LARGE SCALE MODELING OF PRECIPITATION INDUCED LANDSLIDES

A Thesis

Presented to

The Faculty of the Graduate School

At the University of Missouri-Columbia

In Partial Fulfillment

Of the Requirements for the Degree

Master of Science

In Civil and Environmental Engineering

By

JULIO MALDONADO,

Dr. John Bowders, Thesis Supervisor

DECEMBER, 2014

The undersigned, appointed by the dean of the Graduate School, Have examined the Thesis entitled

LARGE SCALE MODELING OF PRECIPITATION INDUCED LANDSLIDES

Presented by Julio Maldonado,

a candidate for the degree of Master of Science in Civil and Environmental Engineering

and hereby certify that, in their opinion, it is worthy of acceptance.

John J. Bowders, P.E.

J. Erik Loehr, P.E.

Timothy Matisziw

ACKNOWLEDGEMENTS

I first would like to thank the people of the United States of America. I would have not accomplished this goal without their help and support. I also extend my thankfulness for the support, knowledge and mentoring for this research project to Dr. John Bowders and Dr. Erik Loehr. I also want to thank Dr. Sung-Chi Hsu from Department of Construction Engineering, Chaoyang University of Technology, in Taiwan for his training in the laboratory of the University of Missouri-Columbia. I also would like to acknowledge the participation of three wonderful undergraduate students who collaborate with enthusiasm, ideas and hard work to develop this research. These three people are: Eric Lindsey, Williams Omatsone and Mitchel Shaneberger. Others contribution are highly appreciated including Rani Jaafar; who helped me to measure the saturated hydraulic conductivity. I also extend my gratitude to Tyler McKee who provided valuable information about the model soil.

To all of them I extend my deepest and sincere gratitude.

TABLE OF CONTENTS

LIST OF FIGURES

LIST OF TABLES

ABSTRACT

Around the world, earth slope failures, often termed landslides, are a major hazard to human activities. Slope failures can damage critical infrastructure such as highways, dams, bridges and airports, and may result in loss of life. These impacts can arise due to direct contact with the compromised slope or via secondary effects, such as tidal surges triggered by undersea landslides.

Landslides are commonly caused by changes in the interaction between water and soil particles on sloping ground. The water can come from natural sources, such as rain and floods, or man-made sources, such as latrines, broken pipes, or poor drainage. The water can reduce the strength of the soil by causing pore water pressures to increase resulting in lower effective stresses and lower shear strength.

The objective of this research is to collect experimental data that can be used to initiate development of a model to predict impending rainfall-induced landslides (slope failures). The scope of the research included in this thesis is the construction, instrumentation and testing of three soil slopes subjected to rainfall-induced failure. Negative and positive pore water pressures, slope angle, precipitation, deformation and drainage are measured for each slope. The stability of each slope is analyzed for various positions of the water (wetting) front as it moves through the soil in the slope.

The experimental results from this study showed different characteristics of slope failures occurring under saturated and unsaturated conditions. In the case of the saturated slope, the failure initiated close to the toe due to infiltration and seepage that

reduced suction in the soil; resulting in higher pore pressures and lower effective stress in this region. The toe failures subsequently lead to a slow retrogressive failure along the slope. The unsaturated slope was stable at higher angles and unlike the saturated slope failed suddenly and moved rapidly. This study demonstrated that monitoring pore pressures in unsaturated slopes can provide insight into the changing stability conditions and may ultimately provide the basis for an early-warning failure system.

CHAPTER 1 INTRODUCTION

1.1 Background

Around the world, countries are struck by earth slope failures, in different scenarios; in man-made structures like embankments for highways, dams, airports or, in nature like mountains and hills. In all cases, failures of slopes constitute a hazard that diminishes the quality of life of people and in many cases, it takes their lives.

In 1998 the Central America region was stricken by Hurricane Mitch; an erratic category five hurricane, which emerged in Cabo Verde, Africa and ended up on the coast of the United States of America, unleashing unexpected amounts of precipitation on Central America. This hurricane caused more than 19,000 casualties in Central America; 14,600 in Honduras. It is considered one of the deadliest hurricanes in the history of the Atlantic, and the deadliest in the past century. Many of these casualties were caused by landslides and floods. Mitch affected 80 percent of the infrastructure and turned Honduras into the most vulnerable country of the world. Hurricane Mitch also caused economic damages on the order of US$ 3.8 billion, more than three times the national budget of Honduras 1998 (US$ 1.2 billion).

One of the cities affected by hurricane Mitch was Tegucigalpa, capital of Honduras, located in the central portion of the country. Most of the soil in Tegucigalpa corresponds to a clay formation in different states of consolidation. On top of this formation lays all types of urban development; from the lowest income to the

wealthiest urban developments. Three major landslides occurred in Tegucigalpa; which caused the loss of thousands of human lives.

1.2 Objective

A landslide is caused by the interaction of water in soil on sloping ground. The water can come from many sources: natural; like rain and floods, or man-made; like latrines, broken pipes, and bad drainage. In all cases, the water reduces the soil strength as the water infiltrates into the soil; it causes an increase in the pore water pressures which reduces the effective stress and thus reducing a soil's resistance to shear. The amount of infiltration combined with other soil characteristics: void ratio, moisture content, geology, land use, soil grain size distribution, hydraulic conductivity and drainage will determine whether the soil slope fails under unsaturated or saturated conditions.

The objective of this research is to collect experimental data that can be used to initiate development of a model to predict impending rainfall-induced landslides (slope failures).

1.3 Scope

The scope of the research included in this thesis is the construction, instrumentation and testing of three soil slopes subjected to rainfall-induced failure.

Negative and positive pore water pressures, slope angle, precipitation, deformation and drainage are measured for each slope. The stability of each slope is analyzed for various positions of the water (wetting) front as it moves through the soil in the slope.

1.4 Organization of Thesis

This thesis consists of six chapters. Chapter 2 is a literature review of slope stability and rainfall-induced slope failures. The physical methods and the instrumentation used to obtain the information from the experimental test are described in Chapter 3. The experimental test results are presented in Chapter 4. Chapter 5 contains the analysis and discussion of the results from the testing. The conclusions from this work are presented in Chapter 6.

CHAPTER 2 LITERATURE REVIEW

This chapter focuses on the theoretical concepts necessary to calculate process and analyze the data collected from the three large-scale precipitation -induced slope stability tests. All experiments were conducted at the University of Missouri in the large-scale geotechnical modeling laboratory.

2.1. Rainfall-Induced Landslides

Lu and Godt, 2012 define a landslide as a down slope mass movement due to soil failure under saturated or unsaturated conditions. The socioeconomic factors that may affect the occurrence of landslides are:

a) Increased Human Developments in Landslide Prone Areas.

b) Continued Deforestation in Landslide Prone Areas.

c) Increased Regional Precipitation Caused by Climate change.

***Increased Human Developments in Landslide Prone Areas**:* Figure 2.1 shows an example of how human development can create landslide prone conditions. In the first stage an undisturbed sloping terrain; in the second stage the urbanization is developed by cutting into the slope; creating the hazardous conditions, and in the last stage, the landslide has occurred.

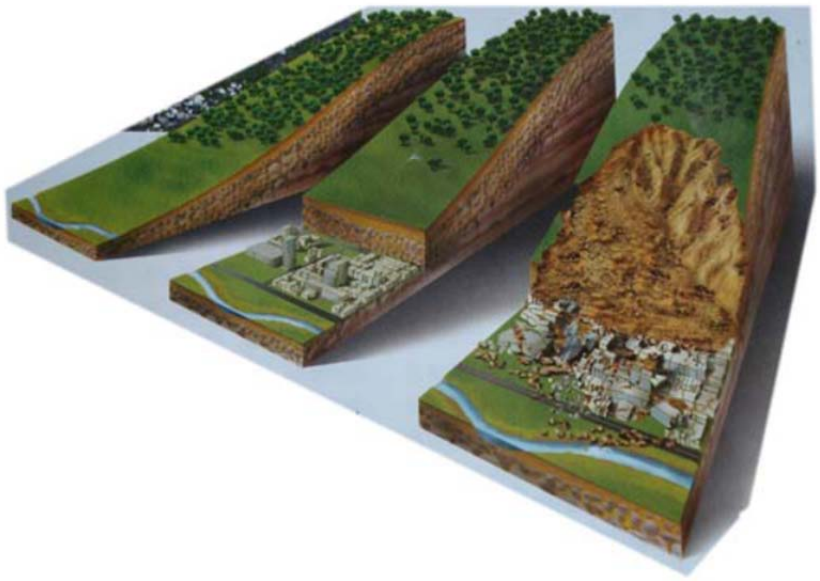

Figure 2.1 Human development creating hazardous conditions. (Lu and Godt, 2012).

***Continued Deforestation in Landslides Prone Areas**:* The deforestation or removal of the land cover causes exposure of the soil to weathering elements including rain, sun and wind which cause stress changes in the soil which influence the occurrence of landslides.

Increased Regional Precipitation Caused by Changing Climate Patterns*:*

Climate change around the world is causing unpredictable climate patterns. One of the most important changes is in the precipitation. The initiation of a landslide is strongly affected by total rainfall, short-term precipitation intensity, antecedent soil moisture and storm duration.

2.2 The cause of landslides

Three major factors are thought to influence the likelihood of occurrence of a landslide (Lu and Godt, 2012):

Geological Factors*:* This factor includes the unique characteristics: Structure and texture of the soil prone to landslides, weak or sensitive materials, weathered materials, sheared, jointed or fissured materials, adversely oriented discontinuities, bedding faults etc. and contrast in permeability and/or stiffness of materials.

Morphological Factors*:* This factor includes changes in the form, shape and pattern of the soil like tectonic or volcanic uplift, glacial rebound, fluvial, wave, or glacial erosion, subterranean erosion-dissolution, deposition loading, vegetation removal by fire or drought, freeze-and-thaw weathering and shrink-swell weathering

Human Factors*:* This factor includes the effect of human activities in the landscape which increase the proneness to landslides like excavation, loading, groundwater drawdown, deforestation, irrigation, mining and artificial vibration.

2.3. Types of Landslides

The following series of figures summarize the most common types of slope failures according to Lu and Godt (2012). These types of slope failure are associated with the way the soil moves down the slope, the shape and size of the mass of soil.

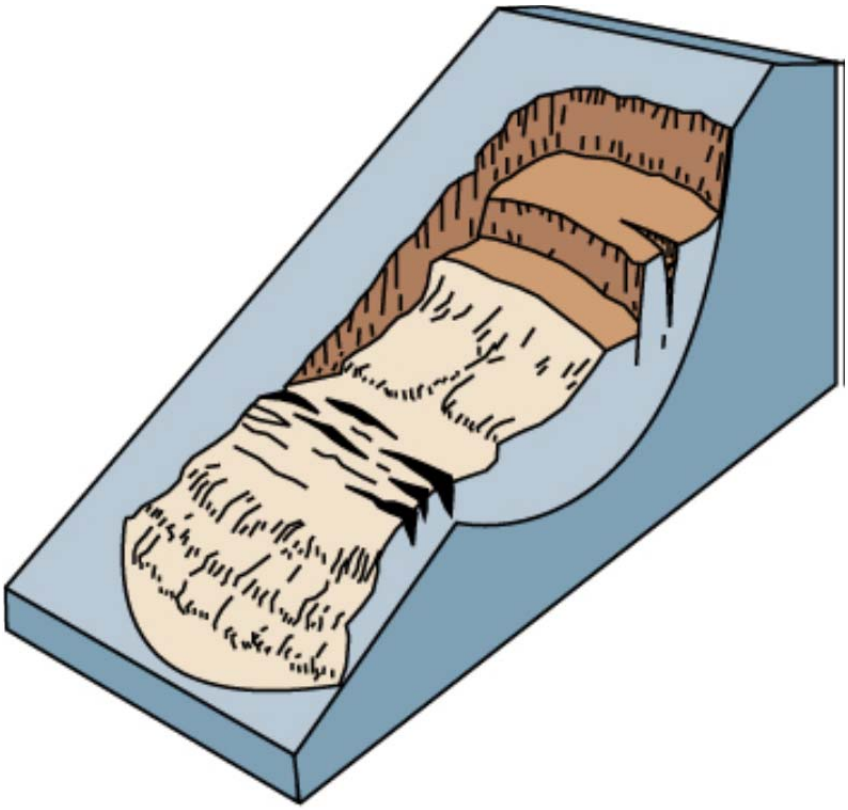

Figure 2.2 Rotational landslides. (Lu and Godt, 2012).

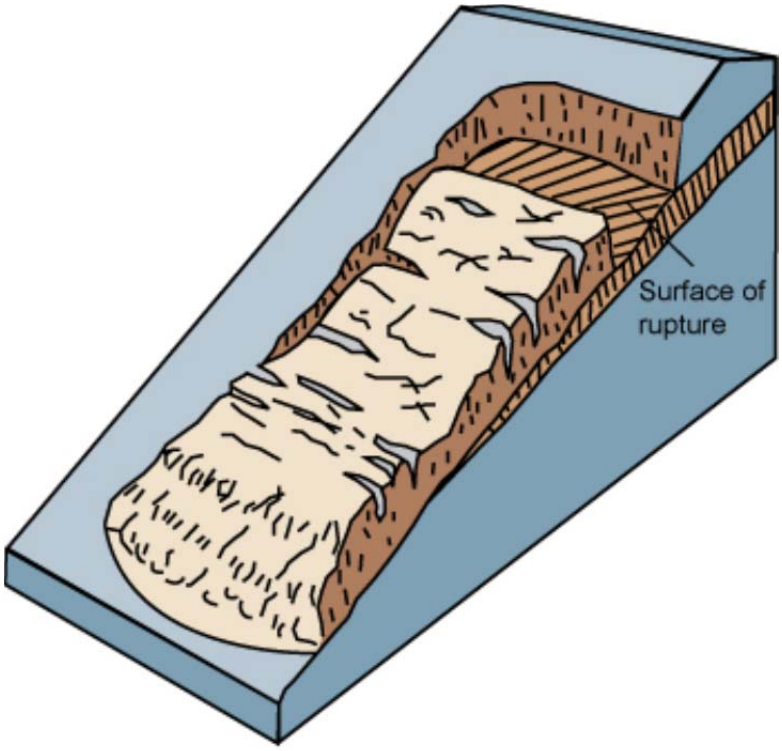

Figure 2.3 Translational landslide. (Lu and Godt, 2012).

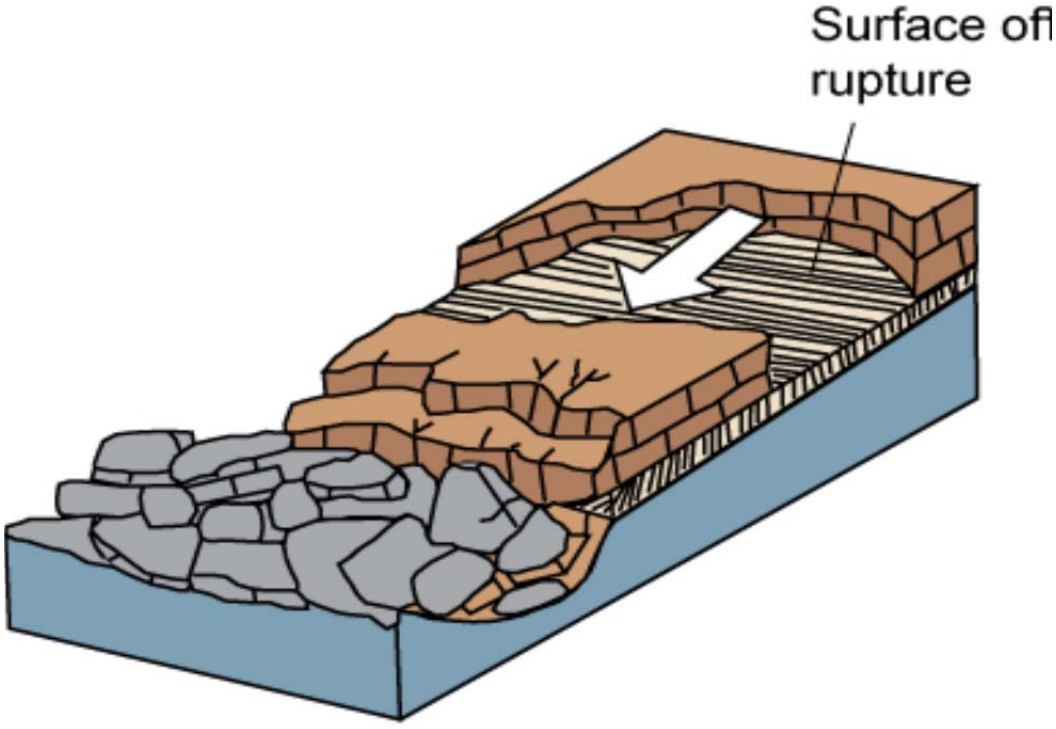

Figure 2.4 Block slide. (Lu and Godt, 2012).

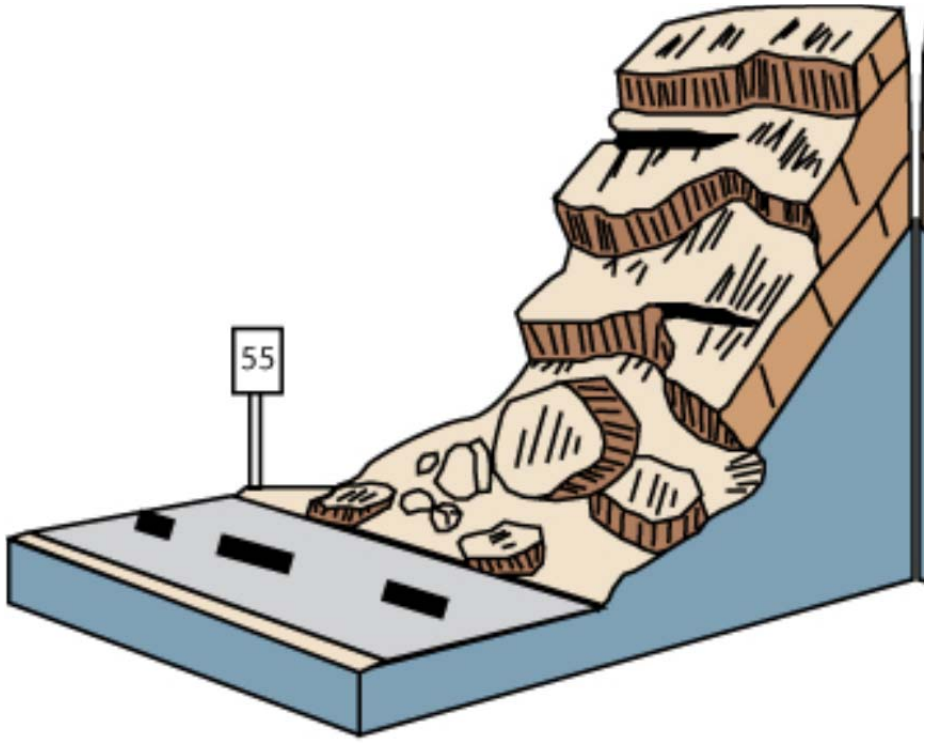

Figure 2.5 Rockfall. (Lu and Godt, 2012).

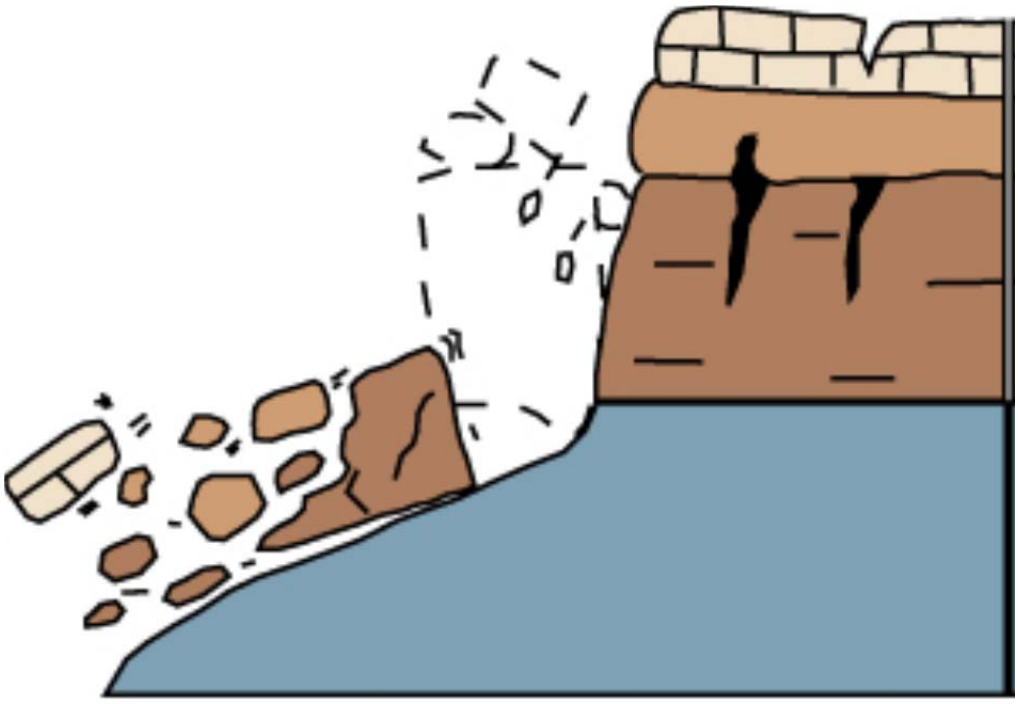

Figure 2.6 Topple. (Lu and Godt, 2012).

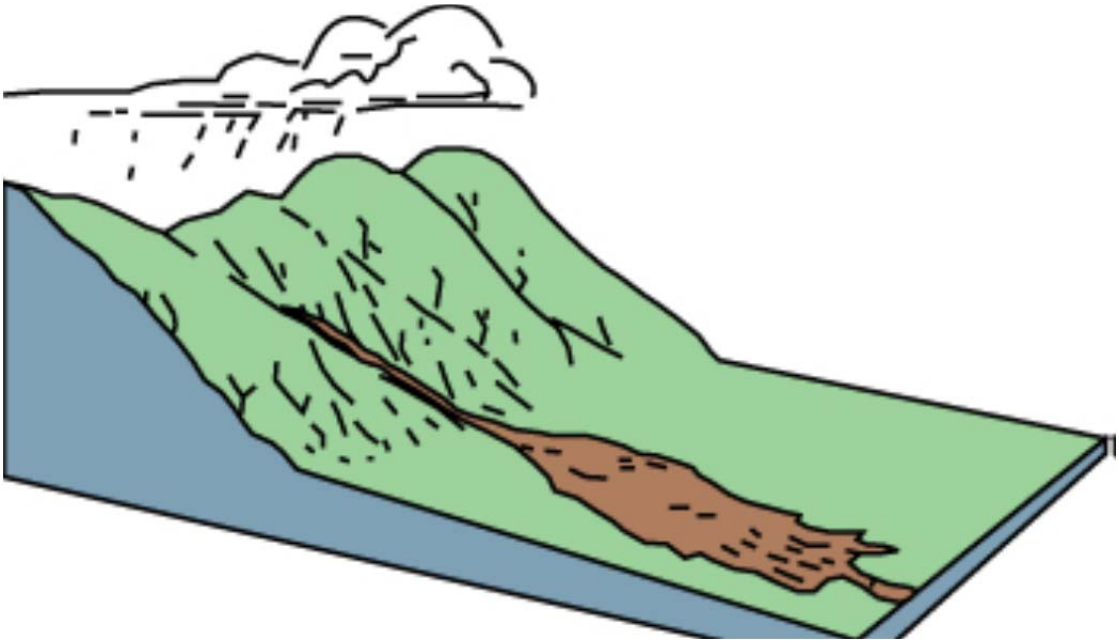

Figure 2.7 Debris flow. (Lu and Godt, 2012).

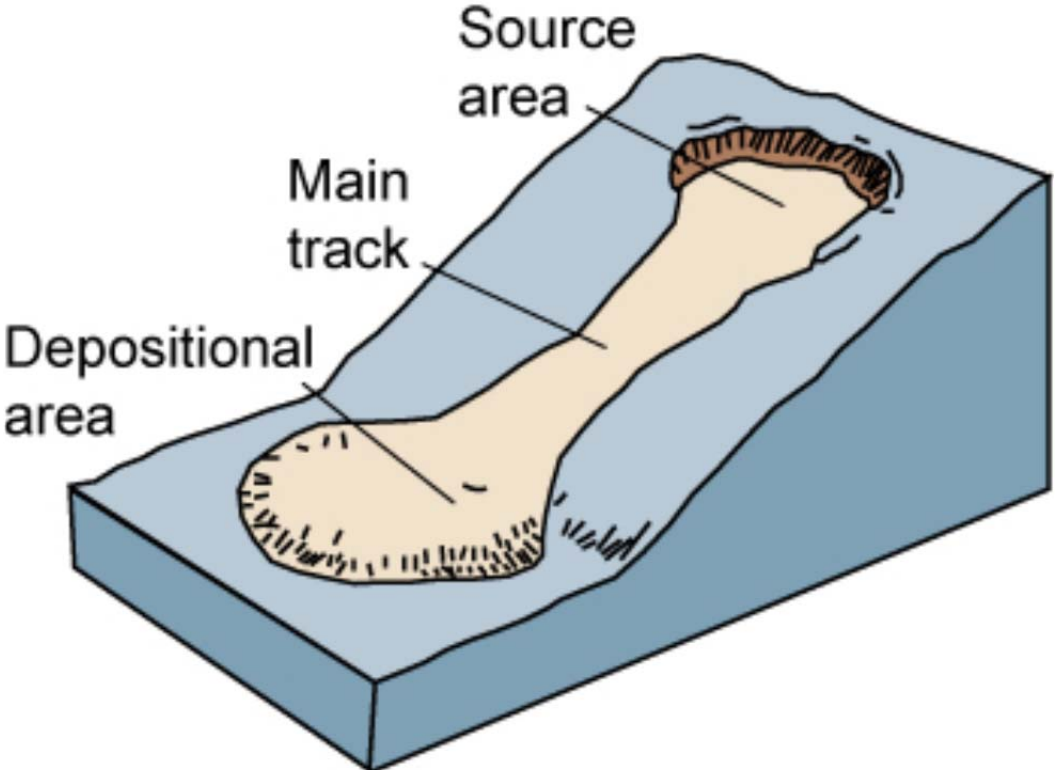

Figure 2.8 Earthflow. (Lu and Godt, 2012).

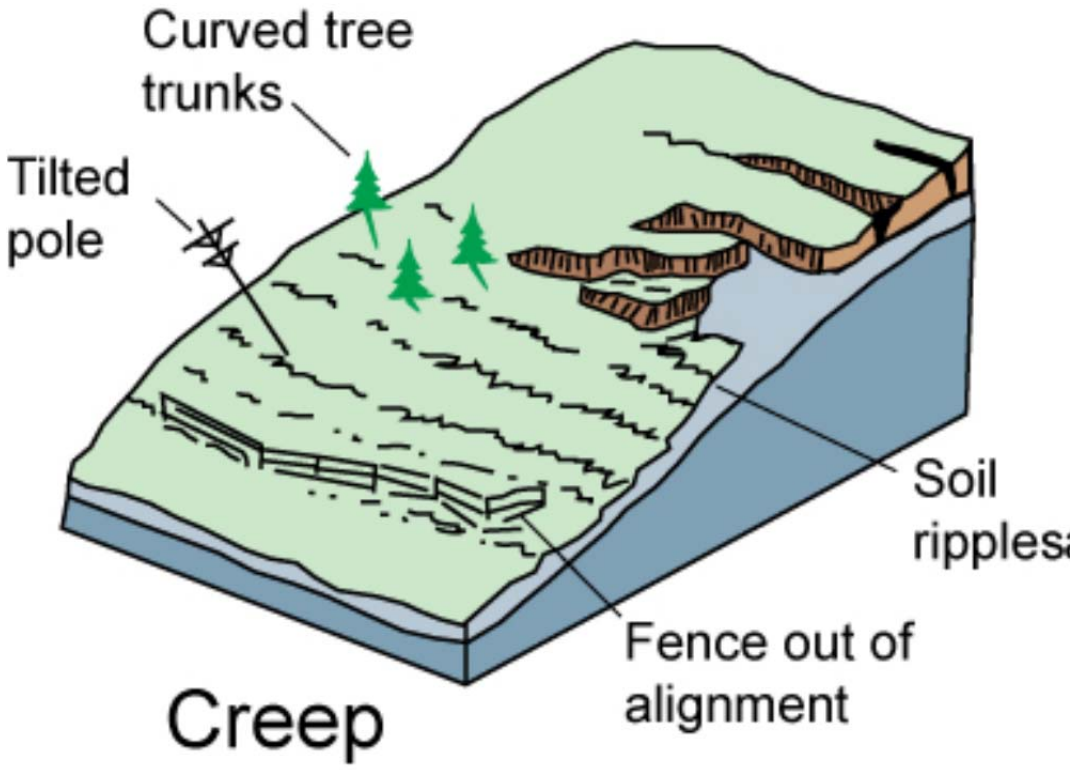

Figure 2.9 Creep. (Lu and Godt, 2012).

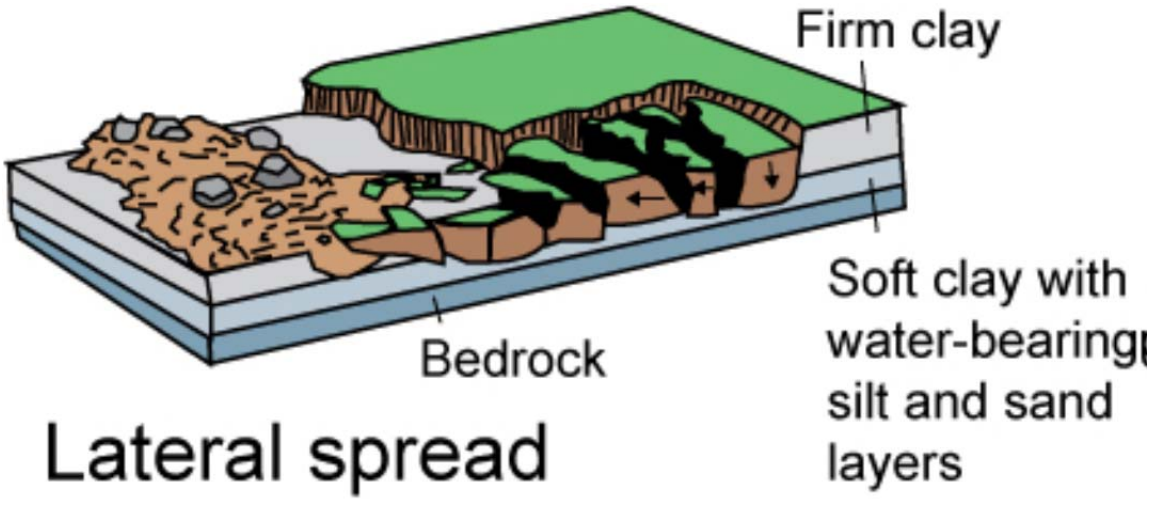

Figure 2.10 Lateral spread. (Lu and Godt, 2012)

2.4. Mechanical Failure due to Water

As water infiltrates into soil, two major mechanical phenomenon occur; Strength Reduction Mechanism and Stress Variation Mechanism (Lu and Godt, 2012).

Strength Reduction Mechanism*:* This aspect accounts for the loss of strength caused by mechanism triggered by the infiltration of water in the soil. Some of these mechanism include:

Weathering*:* The physical, chemical, and biological processes leading to the breackdown of soil or rock into small pieces.

Creeping Permanent displacement of the soil particles that occurs over time. It can result in the sliding of a mass of soil on a continuous plane.

Leaching: Consists of a constant dissolution of soluble minerals in the soil along infiltration pathways. It causes an increase in the porosity and void ratio, thus a reduction in the strength.

Cracking The development of a zone of tension at the top of a clayey soil causing cracks. These cracks promote soil movement and accelerate infiltration.

Slickenside The formation of slip planes in clayey soil caused by previous movement along the plane.

Stress Variation Mechanism: Accounts for the increase in the stress caused by the infiltration of water into the soil. Some of them are listed next:

Pore Water Pressure, A reduction in the effective stress resulting in soil failure. It can be caused by precipitation. Precipitation can also raise the level of groundwater.

Weight of Water, The increase in the weight of the soil near the surface caused by wetting. This increase could reach up to 30 percent and increase the total stress in the soil.

Swelling and Shrinking, Clayey soils like a smectite (montmorillonite) are affected by this mechanism. The availability of water can cause an increase in the void ratio, resulting in a reduction in the strength or development of cracks during times of drying.

Earthquakes, Processes leading to vertical and horizontal movement in the soil, leading to total stress and pore pressure variation.

Soil Suction, A mechanism affecting the unsaturated zone. It varies depending in the type of soil. Soil suction is important in shallow soils. In sandy soils it can cause failure in steep slopes with more than a thirty degree inclination. In silty soils, it can cause failure in moderately steep slopes with more than twenty five degree inclination and in clayey soils in any slope environment (Lu and Godt, 2012).

2.5. Slope Stability Analyses

The mobilized shear stress τ, is equal to the available shear strength, S, divided (factored) by the factor of safety. The factor of safety shown in equation 1 represents the factor by which the shear strength must be reduced so that the reduced strength is just in equilibrium. (Duncan and Wright, 2004)

$$FS = \frac{S}{\tau} \qquad \textbf{Equation 1}$$

The shear strength of a soil, whether saturated or unsaturated, may be defined as the maximum internal resistance per unit area the soil is capable of sustaining along the failure plane under external or internal stress loading. (Duncan and Wright, 2004)

2.6. Limit Equilibrium Analysis and Slope Stability of Unsaturated Soils

2.6.1. Total Soil Suction.

Total suction quantifies the thermodynamic potential of the soil pore water relative to a reference potential of free water. The physical and physicochemical mechanisms responsible for total suction are those that decrease the potential of the pore water relative to this reference state. These mechanisms are the capillary effect, short-range adsorption and the osmotic effect. (Lu and Likos, 2004)

The Capillarity Effect accounts for the relationship among the geometry of the soil and the fluid pressure, relative humidity and vapor pressure at an air-water-soil interface.

Short range adsorption accounts for the effects of electrical and van der Waal's forces occurring in the vicinity of the soil-water interface. Electrical forces emanate from the negative charge on the surfaces of clay minerals and van der Waal's forces emanate from atomic scale interaction among molecules comprising the liquid face.

Osmotic effects are the results of dissolved solutes in the pore water which may come from two sources: externally introduced solutes and naturally occurring solutes adsorbed by the soil mineral surfaces.

The suction derived from the combined effects of capillarity and short range adsorption is usually grouped as *Matric Suction*. Suction derived from the presence of dissolved solutes is referred as *Osmotic Suction.*

The total suction is the addition of both, Matric suction and Osmotic suction.

The importance of the individual physical and physicochemical mechanisms responsible for soil suction depends on the water content of the unsaturated soil-water-air system. At relatively low values of water content and correspondingly high values of suction, the dominant mechanism contributing to suction are the short range adsorption effects governed by the surface properties of the soil solids. At relatively high values of water content and correspondingly low values of suction, the dominant pore water retention mechanism becomes capillarity, governed by the particle and pore

structure and pore size distribution. The osmotic suction is constant over the entire range of water content unless the concentration of dissolved solutes changes.

The Soil Water Characteristic Curve (SWCC) describes the corresponding constitutive relationship between soil suction and soil water content. The shape of the SWCC describes the effects of soil properties including pore size distribution, grain size distribution, density, organic material content, clay content and mineralogy on the pore water retention behavior. Figure 2.11 describes in general the SWCC (Lu and Likos, 2004).

Van Genuchten (1980) proposed a SWCC function expressed in terms of effective water content or degree of saturation as follows:

$$S_e = \frac{\theta - \theta_r}{\theta_s - \theta_r} = \left[\frac{1}{1 + (\alpha\psi)^n}\right]^m \qquad \textbf{Equation 2}$$

Where *m=1-1/n, n and α* are fitting parameters; *n* is related to the pore size distribution of the soil.

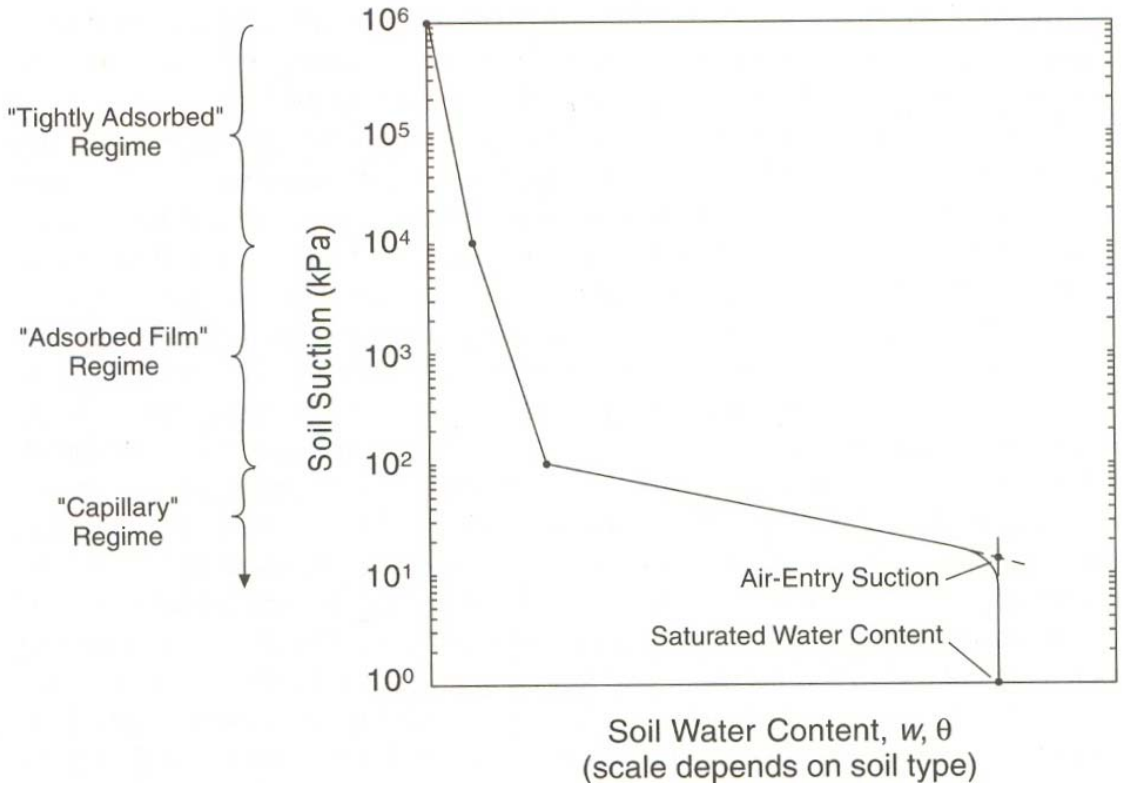

Fig. 2.11 Soil Water Characteristic Curve. (Lu and Likos, 2004).

For an unsaturated soil, the effects of the three phases of the soil; air, water and solids, have to be accounted in the computation of the shear strength. Fredlund et al. (1978) formulated and extended the Mohr–Coulomb criterion to describe the shear strength behavior of an unsaturated soil. The failure surface is a planar surface (Figure 2.12) in the space of the stress state variables $\sigma - u_a$ and $\sigma - u_w$ and shear stress τ and may be written as:

$$\boldsymbol{\tau_f = c' + (\sigma - u_a)_f \tan \emptyset' + (u_a - u_w)_f \tan \emptyset^b} \qquad \textbf{Equation 3}$$

Where c' is the cohesion at zero matric suction and at zero net normal stress, $(\sigma - u_a)_f$ is the net normal stress on the failure plane at failure, ϕ' is the angle of internal friction associated with the net normal stress variable, $(u_a - u_w)_f$ is the matric suction at failure, and ϕ^b is an internal friction angle strength relative to matric suction.

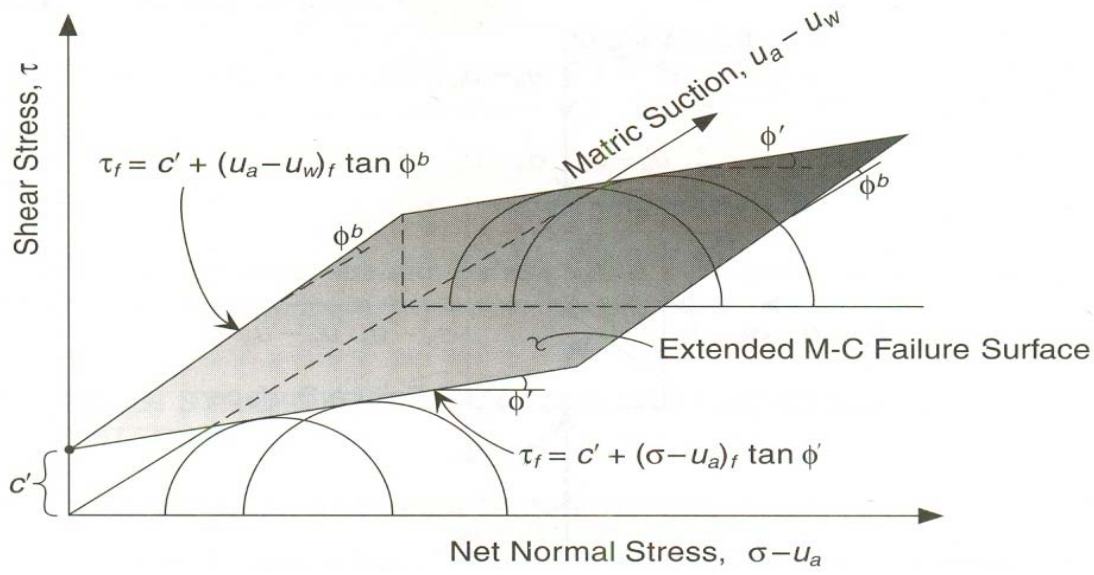

Fig. 2.12 Mohr-Coulomb Diagram for an unsaturated soil. (Lu and Likos, 2004).

For an unsaturated soil; in terms of effective stress approach, as initially proposed by Bishop (1959), the effective stress can be defined by jointly using state stress variables: Net normal stress, $\sigma - u_a$ and matric suction $u_a - u_w$ and one material variable: The *Effective Stress Variable* χ. Bishop's effective stress proposal is:

$$\boldsymbol{\sigma' = (\sigma - u_a) + \chi(u_a - u_w)} \qquad \textbf{Equation 4}$$

The effective stress parameter χ is a function of the degree of saturation of the soil mass and reflects the contribution of matric suction to effective stress.

For a saturated soil, the air pressure is zero, the water pressure is compressive or positive, χ is equal to one and Equation 4 reduces to Terzaghi's classical effective stress Equation 5

$$\boldsymbol{\sigma' = \sigma - u_w} \qquad \textbf{Equation 5}$$

For a completely dry soil, χ is equal to zero and the effective stress is the difference between total stress and air pressure:

$$\boldsymbol{\sigma' = \sigma - u_a} \qquad \textbf{Equation 6}$$

For partially saturated soils, χ is some function of the degree of saturation or matric suction. χ may not be directly measured or controlled through experiments. However Bishop (1954) proposed an indirect way to obtain χ from stresses measured in soil specimens at failure. The traditional Mohr-Coulomb criterion was used to represent the failure conditions:

$$\boldsymbol{\tau_f = S = c' + \sigma' \tan \emptyset'} \qquad \textbf{Equation 7}$$

Which after substitution of the effective stress equation (Equation 4) leads to:

$$\boldsymbol{\tau_f = S = c' + [(\sigma - u_a)_f + \chi_f (u_a - u_w)_f] \tan \emptyset'} \qquad \textbf{Equation 8}$$

Where τ_f is shear strength and c' and ϕ' are the effective cohesion and friction angle, respectively.

Vanapali and Fredlund (2000) proposed several forms of χ as a function of the degree of saturation using a series of shear strength test results for statically compacted mixtures of clays, silts and silty sand from Escario and Juca (1989). For a matric suction ranging between 0 and 1500 kPa, the following two forms showed good fit to the experimental results:

$$\boldsymbol{\chi = S^k = \left(\frac{\theta}{\theta_s}\right)^k} \qquad \textbf{Equation 9}$$

Where S is the degree of saturation, θ is the volumetric water content, θ_s is the saturated volumetric water content, and *k* is a fitting parameter optimized to obtain a best fit between measured and predicted values, and

$$\boldsymbol{\chi = \frac{S - S_r}{1 - S_r} = \frac{\theta - \theta_r}{\theta_s - \theta_r}} \qquad \textbf{Equation 10}$$

Where θ_r is the residual volumetric water content, S_r is residual degree of saturation and S is the degree of saturation.

2.7 Theoretical Equation for Hydraulic Conductivity. (Mitchell and Soga, 2004)

Darcy's law also applies to flow through unsaturated soils. However the hydraulic conductivity is not constant and depends on the amount and connectivity of water in the pores. The hydraulic conductivity of unsaturated soils can be a function of saturation, water content, matric suction or others. A general expression for hydraulic conductivity of unsaturated soils can be written as:

$$\boldsymbol{k = k_r k_s} \qquad \textbf{Equation 11}$$

Where K_s is the saturated conductivity and K_r is called *relative permeability* where the values range from 0; for no interconnected path for the permeating fluid, to 1 for permeating fluid at full saturation.

The use of the soil water characteristic curve (SWCC) to estimate the hydraulic conductivity of unsaturated soil is attractive because it is easier to obtain this curve in the laboratory than it is to measure unsaturated hydraulic conductivity directly. Mualem (1976) suggest equation 12 for hydraulic conductivity as a function of the Soil Water Characteristic Curve:

$$k_r(\theta) = \left(\frac{\theta - \theta_r}{\theta_s - \theta_r}\right)^q \left(\frac{\int_{\theta_r}^{\theta} \frac{d\theta}{\psi(\theta)}}{\int_{\theta_r}^{\theta_s} \frac{d\theta}{\psi(\theta)}}\right)^2 \qquad \textbf{Equation 12}$$

Where *q* describes the degree of connectivity between the water-conducting pores. Mualem (1976) suggested a value of *q=0.5* based on permeability measurements on 45 soils. Van Genuchten et al. (1991) substituted the Soil Water Characteristic equation into Equation 12 and obtained the following closed-form solution for the hydraulic conductivity as a function of water content in the soil:

$$k_r(\theta) = \left(\frac{\theta - \theta_r}{\theta_s - \theta_r}\right)^q \left\{1 - \left[1 - \left(\frac{\theta - \theta_r}{\theta_s - \theta_r}\right)^{1/m}\right]^m\right\}^2 \qquad \textbf{Equation 13}$$

Where *q=0.5* and *m=1-1/n.*

2.8 Transient Vertical Infiltration. (Lu and Likos, 2004)

Green and Ampt (1911) propose a semi-analytical approach to horizontal and vertical infiltration rates. They first apply Darcy's law to unsaturated soil and then apply a *sharp wetting front* that initially propagates at a relatively fast rate through the column of soil and gradually slows with time. Two assumptions were made; the first is that the suction head in the soil, beyond the wetting front (dry portion of soil) is constant in both, space and time; and the second assumption is, that the water content

and corresponding hydraulic conductivity of the soil, behind the wetting front (wet portion of soil) are constant in both space and time.

For the case of transient vertical flow, this wetting front advances under the combined effects of suction and gravity gradients. Green and Ampt, 1911 proposed a function for the infiltration rate as follows:

$$\boldsymbol{q = k_0\left(1 + \frac{h_0 - h_i}{z}\right)} \qquad \textbf{Equation 14}$$

Where q is the infiltration rate, k_o is the hydraulic conductivity corresponding to the water content behind the wetting front θ_o; h_o is the constant head water supply, h_i is the head beyond the wetting front and z is the position of the wetting front.

Green and Ampt,1911 also proposed another formulation, incorporating the time to predict the advance of the water front as a function of the same variables mentioned before:

$$\boldsymbol{\frac{k_0}{\theta_i - \theta_0}t = z - (h_i - h_0)ln\left(1 + \frac{z}{h_i - h_0}\right)} \qquad \textbf{Equation 15}$$

Where t is the arrival time of the water front at a corresponding θ_o, θ_i and k_o to a depth z.

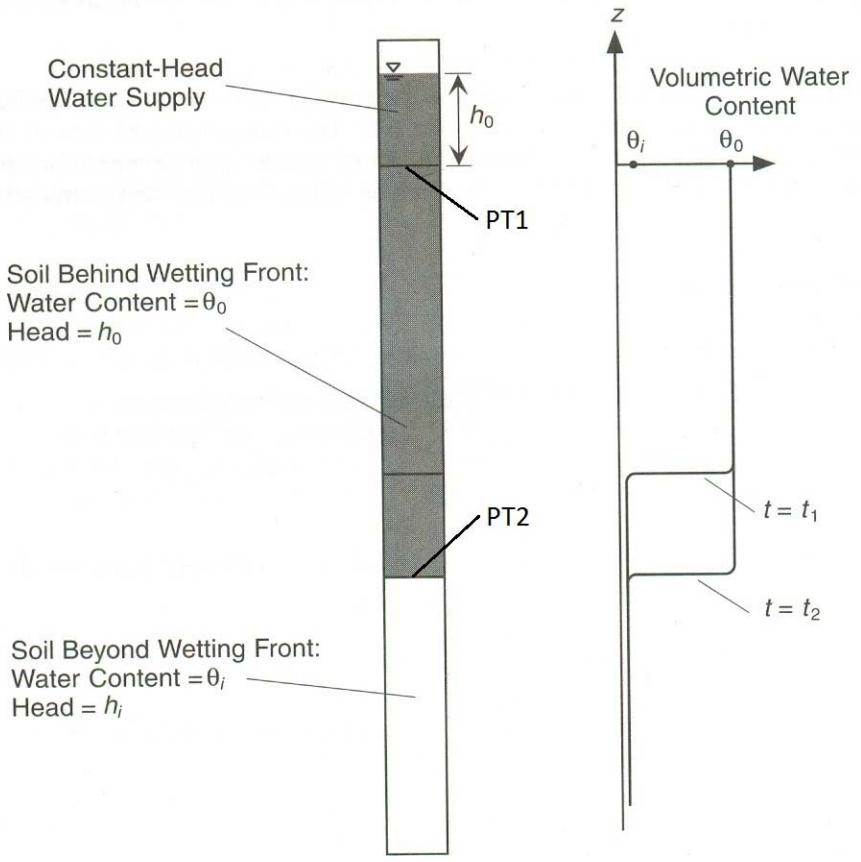

Figure 2.13 Vertical infiltration rate models. (Lu and Likos, 2004)

Figure 2.13 depicts the graphical representation of this model. PT1 is the upper pore pressure transducer which generates h_o, and θ_o; PT2 is the lower pore pressure transducer which generates h_1 and θ_1. Figure 2.14 shows the model, which considers that the rain is a succession of drops of water falling in the same location. In Fig 2.14 a), no rain has occurred. It remains under the original compacted moisture content when the slope was originally built. In b), the first drop of water has fallen and creates the front of water shown, changing the moisture content and the matric suction. In c) the second drop of water has fallen and creates a second front of water, changing again the moisture content and the matric suction. In d), the third drop of water falls and again, it

changes the moisture content and the matric suction. This process repeats continuously. Every drop of water creates a water front that changes the moisture content and the matric suction in the soil, which subsequently will cause a loss in the strength of the soil that will move the slope closer to failure.

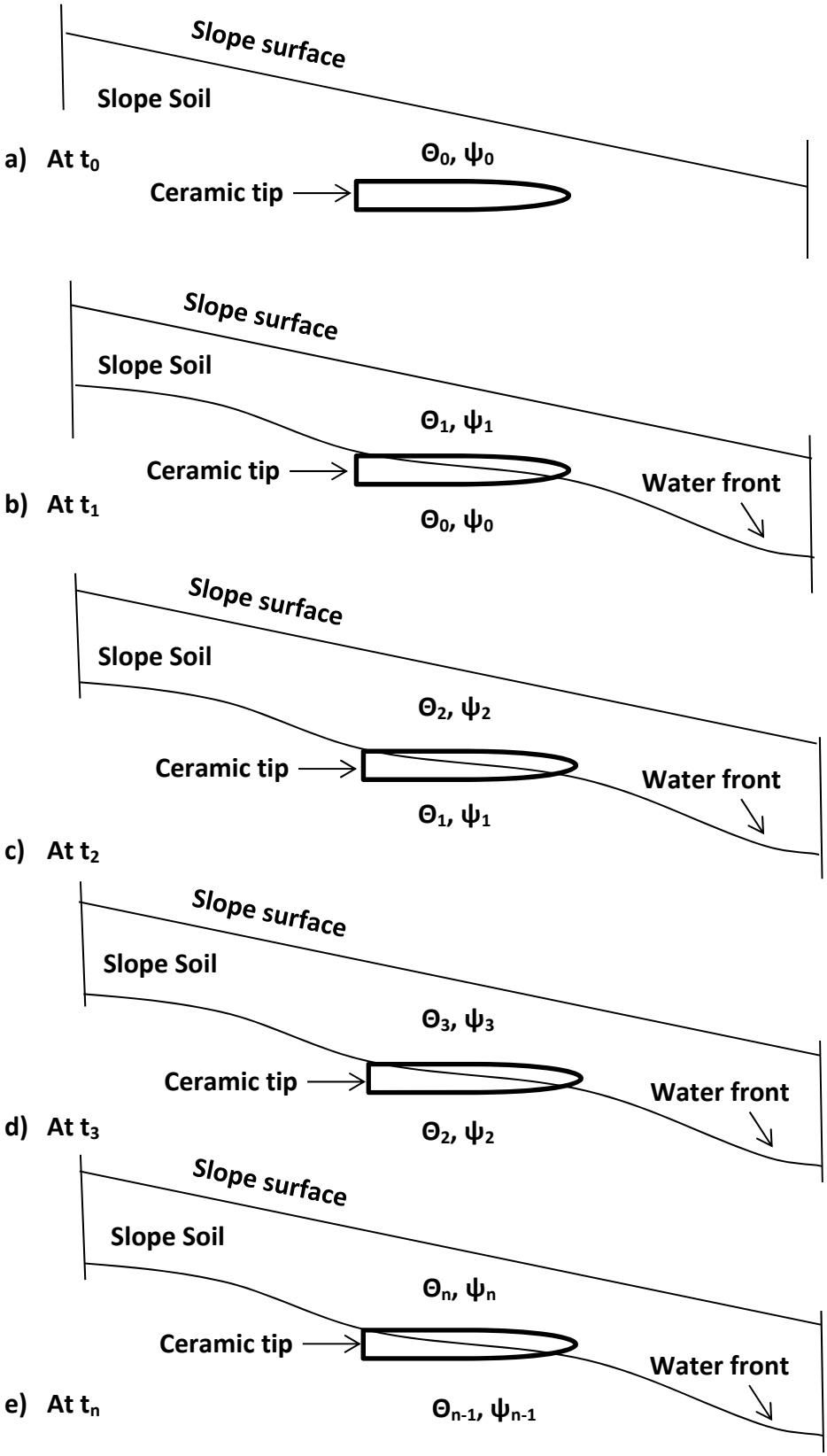

Figure 2.14 Vertical infiltration rate models under precipitation.

2.9 Infinite Slope Procedure.

In 1948 Taylor proposed an infinite slope procedure in which the slope is assumed to extend indefinitely in all directions and sliding is assumed to occur along a plane parallel to the face of the slope. Equilibrium equations, shown in Equations 16 and 17, are derived by considering a rectangular block sliding down a slope (Duncan and Wright, 2004).

$$\tau = \gamma_d(1 + w)z \cos\beta \sin\beta \qquad \textbf{Equation 16}$$

$$\sigma = \gamma_d(1 + w)z \cos\beta^2 \qquad \textbf{Equation 17}$$

Where γ_d is the dry unit weight of the soil, w is the water content; which varies as the wetting front advances and it is obtained from the readings in the tensiometers and the SWCC; z is the vertical depth from the surface to the shear plane.

2.10 Hydraulic Conductivity of Soils and Seepage.

Hydraulic conductivity (permeability) is one of the most important properties of soils. It has decisive effects on the cost and the difficulty of many construction operations. Permeability has important practical implications because water exerts a pressure on the porous material through which it percolates. This pressure is called *seepage pressure.*

As water percolates through a permeable material, the individual water particles move along paths which deviate erratically but only slightly from smooth curves known as *flowlines.* In order for this movement to occur a driving force is necessary. This driving force is the change in the total head and is called *hydraulic head, h.* The pressure that drives the water through the soil is called *hydrostatic pressure* and it can be represented by:

$$\boldsymbol{u = \gamma_w h} \qquad \textbf{Equation 18}$$

Where γ_w is the unit weight of water.

The hydraulic gradient varies as the water moves throughout the soil; tapering from high to low hydrostatic pressures in a determined length, this is called *hydraulic gradient, i. The critical hydraulic gradient* is represented by Equation 19.

$$\boldsymbol{i = (\Upsilon - \Upsilon_w)/\Upsilon_w} \qquad \textbf{Equation 19}$$

Where Y is the saturated unit weight.

When the water percolates in a downward direction, it produces friction between the percolating water and the walls of the voids. This can be described as *drag.* The flow "drags" the soil particles down and thereby increases the effective stress in the soil, increasing the overall stability of the slope (Terzaghi, 1967).

As an example; if a highway embankment, subjected to periodic inundations, consists of well compacted, relatively incompressible soil; the reduction in stability of the slopes can be avoided by the introduction of a layer of gravel underneath the whole embankment. Since the water drains downward into the filter, the seepage pressure acts in a downward vertically direction instead of along the direction of a potential slide plane.

2.11 Summary

This chapter summarizes the theoretical knowledge necessary to process the information obtained experimentally. Caused by the effects of suction and gravity; a water front advances into the soil of a slope, and the soil's properties like; weight, water content, density, suction, etc. change. The suction then is recorded in the tensiometers; and by using the already known SWCC, the suction is used to find the corresponding water content, which later is used to calculate the soil's density, and ultimately to calculate the factor of safety of the slope against sliding. The overall idea in this thesis is to analyze the factor of safety, by using Infinite Slope method.

CHAPTER 3 MATERIALS AND METHODS

This chapter details the experimental setup and instrumentation used in the physical model of rainfall induced slope failures. Description of the slope container, construction process, instrumentation correction and calibration and finally testing are also included.

3.1 Experimental Apparatus

The experimental apparatus consisted of four basic components: The model slope container which is the bed of a dump truck; a lifting mechanism which is a hydraulic cylinder connected to a hydraulic pump; a rainfall application and control system, which is a matrix of nozzles that creates the conditions of rain on the slope and instrumentation which includes devices prepared in order to measure the in-slope seepage and surface runoff, tensiometers to measure pore water pressures and potensiometers to measure displacement. Each device is described below

3.1.1 Model Slope Container

The bed of a dump truck was used to contain and construct the model slope. The container measures 14ft by 8ft by 5ft and it is placed on top of steel frame consisting of W10x30 steel beams. Lexan® sheets were installed along the sidewalls of the container.

Additionally, plastic sheets were installed and cooking oil was sprayed on it; all of this in order to minimize the effects of the friction between the soil and the sides of the container (Figure 3.1).

Provisions were made in order to provide more stability to the device. The container is reinforced with two telescoping stability braces connected to a sliding pivot, which slides along a threaded rod as the container moves up or down. (Figure 3.2)

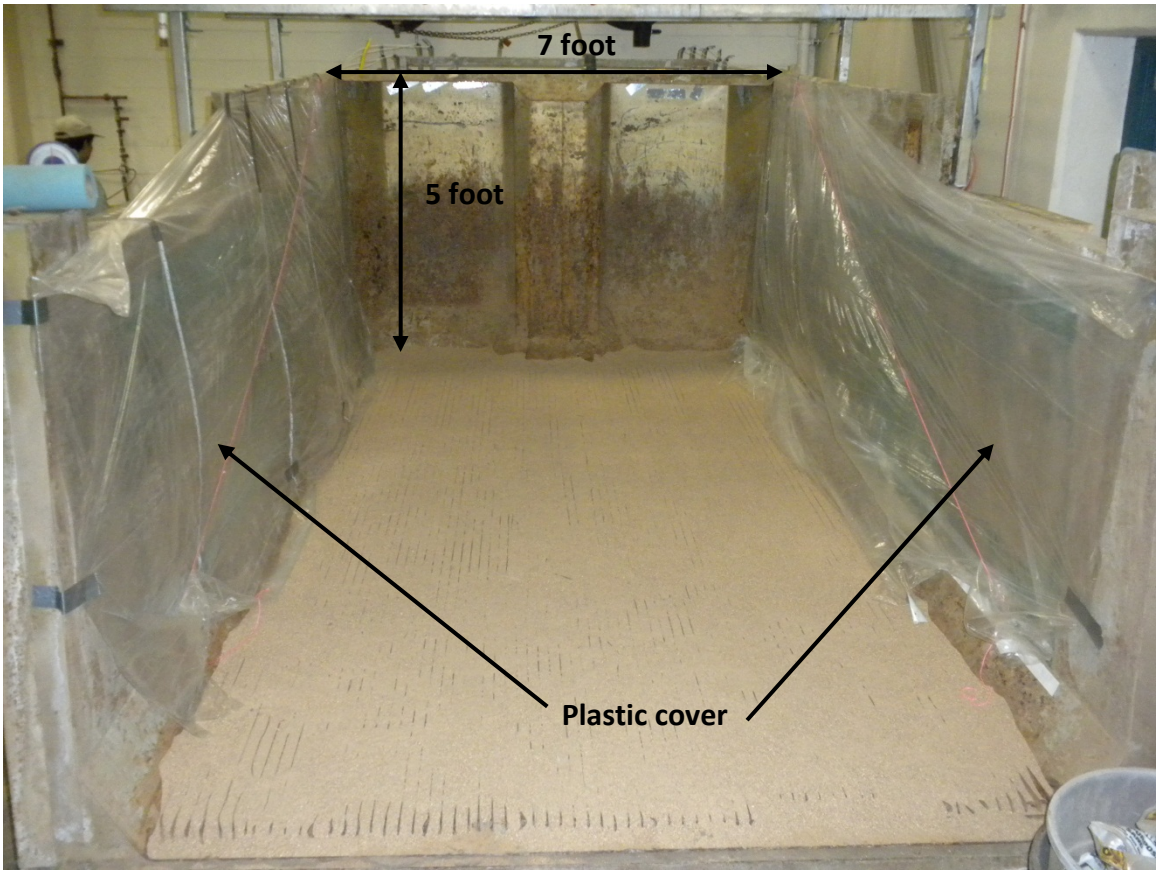

Figure 3.1 Model Container before filling

3.1.2 Lifting Mechanism

The lifting mechanism provides the inclination necessary to the model slope. It is composed of a hydraulic cylinder located beneath of the container and an external hydraulic pump. The hydraulic pump, pumps the oil to the hydraulic cylinder which expands to raise the angle of the slope until the desired inclination. Figure 3.2 and 3.3 show these components.

Figure 3.2 Hydraulic piston of the lifting mechanism.

Figure 3.3 Hydraulic pump used to lift the model container.

3.1.3 Precipitation system

The rainfall control system consists of an array of 30 water sprinkler heads distributed in six rows and five columns mounted on an aluminum frame parallel to the container and controlled using a computer. Figure 3.4 shows the array and Figure 3.5 shows a close-up of the sprinklers heads. Figure 3.6 shows a close up of one of the nozzles used to deliver the precipitation on the slope. The duration of precipitation (Minutes); is regulated by an electronic valve connected to the public water system and a computer. Figure 3.7 and 3.8 show images of the valve.

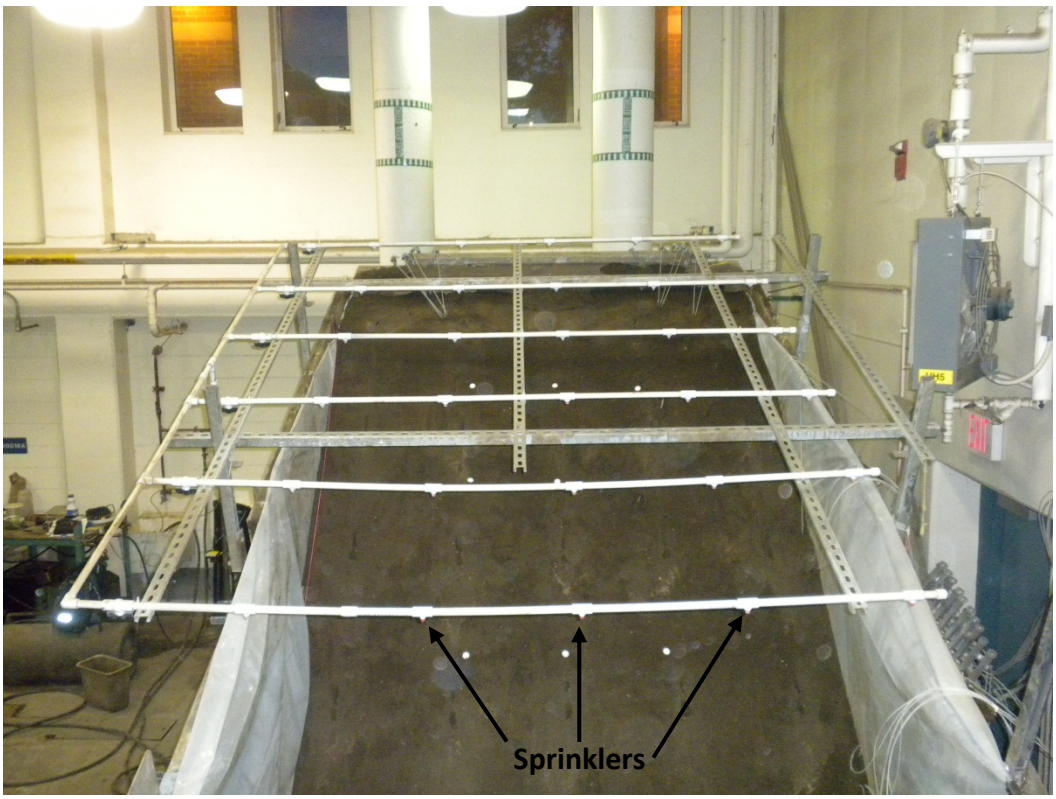

Figure 3.4 Array of sprinklers on top of the slope model.

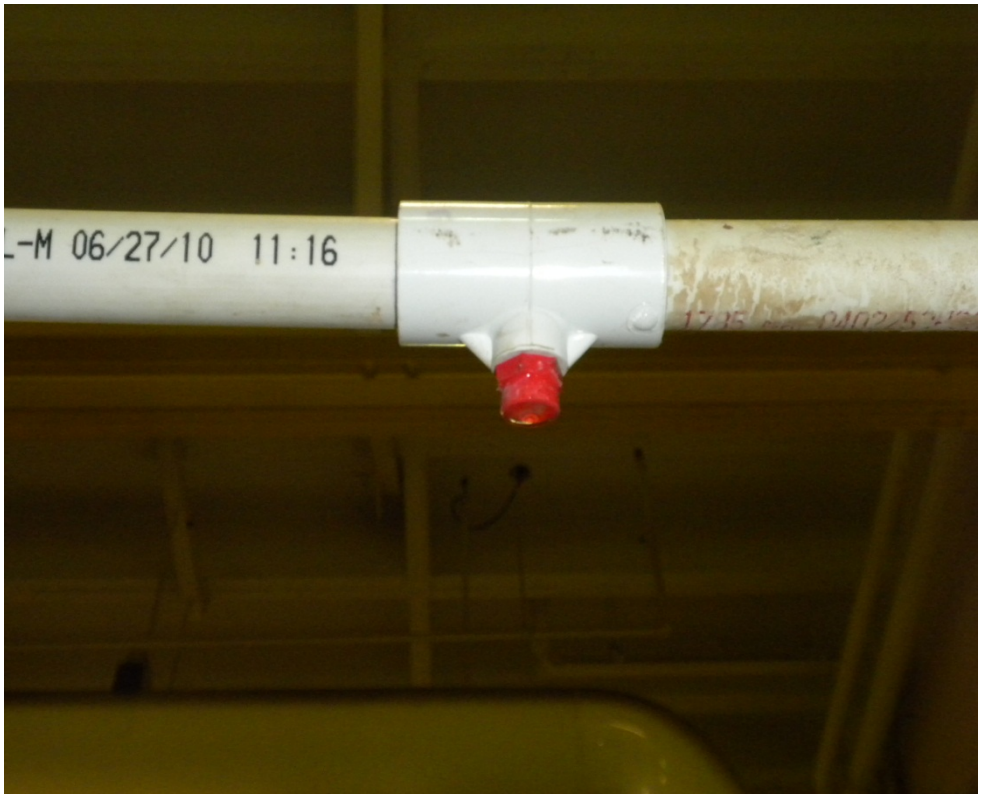

Figure 3.5 Close up to sprinkler head in the array.

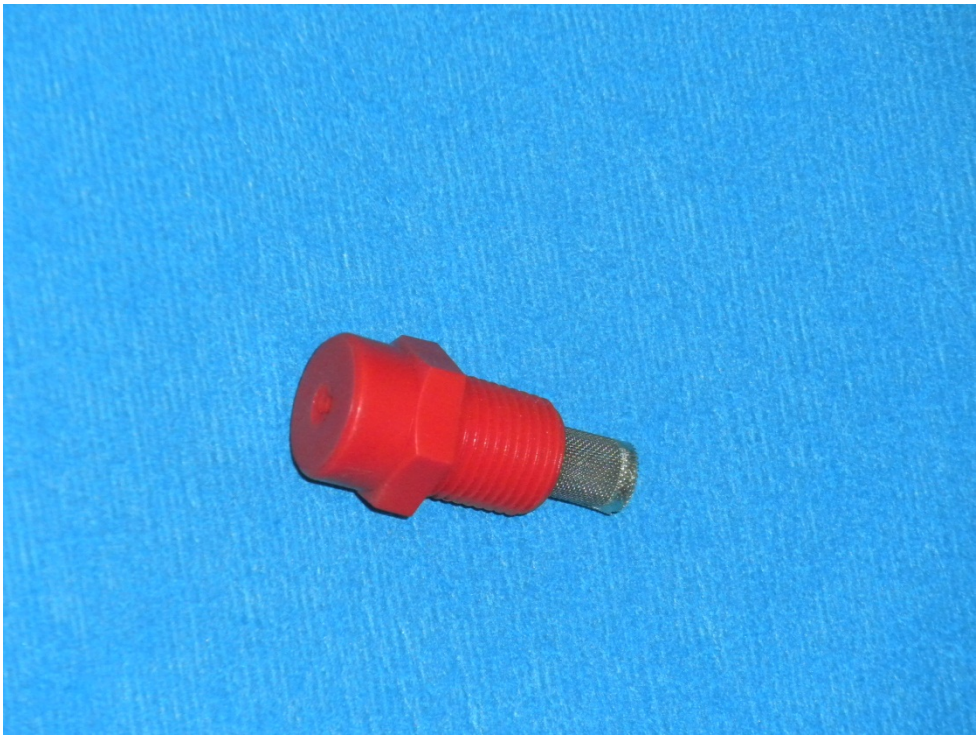

Figure 3.6 Picture of a nozzle used in precipitation system.

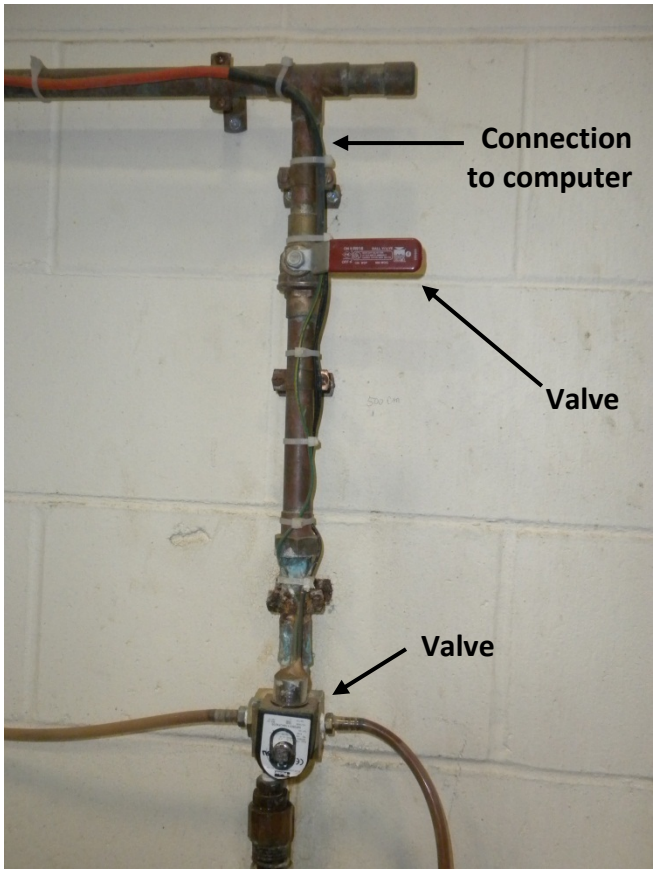

Figure 3.7 Connection to public water system.

Figure 3.8 Water valve.

3.2 Instrumentation

A variety of instrumentation was used to collect data as the water infiltrated into the soil in the slope. The following section describes the instrumentation used to collect this information from the experimental slope. The data collected consisted of pore water pressures, slope deformation, slope inclination angle, quantity of internal seepage and quantity of surface runoff.

3.2.1 Deformation monitoring

Slope displacements were measured using wire-line extensometers consisting of small anchors attached to monofilament lines placed in the model slopes and attached to rotary potentiometers to record movement. An example anchor, consisting of a 1.0-in. diameter washer secured to an I-hook, is shown in Figure 3.9. Monofilament line was attached to each anchor and threaded through flexible tubing (to minimize friction between the monofilament and the surrounding soil) placed in the slope, exiting behind the crest of the slope to the back of the model container. There, the line was connected to a rotary potentiometer that records movements of the anchors. Nine displacement gages were installed in the slope during model slope construction. Each rotary potentiometer, as shown in Figure 3.10, is a Micro-Epsilon® Draw-Wire Displacement Sensor Series WPS Model MK30. The resistance of the potentiometer varies linearly with the length of line pulled from it, so by placing the potentiometer in a voltage

divider circuit, the voltage across the potentiometer varies linearly with movement of the anchor.

The maximum line displacement for the sensors is 30 inches. To protect the sensors from damage, each potentiometer was placed in a protective housing, also shown in Figure 3.10. The housing is mounted to the back of the model slope container as described previously (Boeckman 2006). Figure 3.12 shows the entire set of extensometer, potentiometer and anchor together. Detailed information about the configuration is given in Appendix A.

White dots consisting of door knobs were pushed into the surface of the slope. Dots were monitored using a video recorder to document the movement of the soil mass.

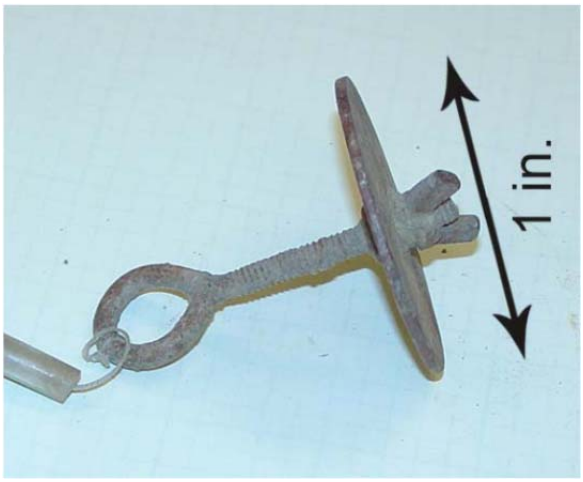

Figure 3.9 Deformation gage anchor with thin conduit (Boeckman 2006).

Figure 3.10 Rotary potentiometer.

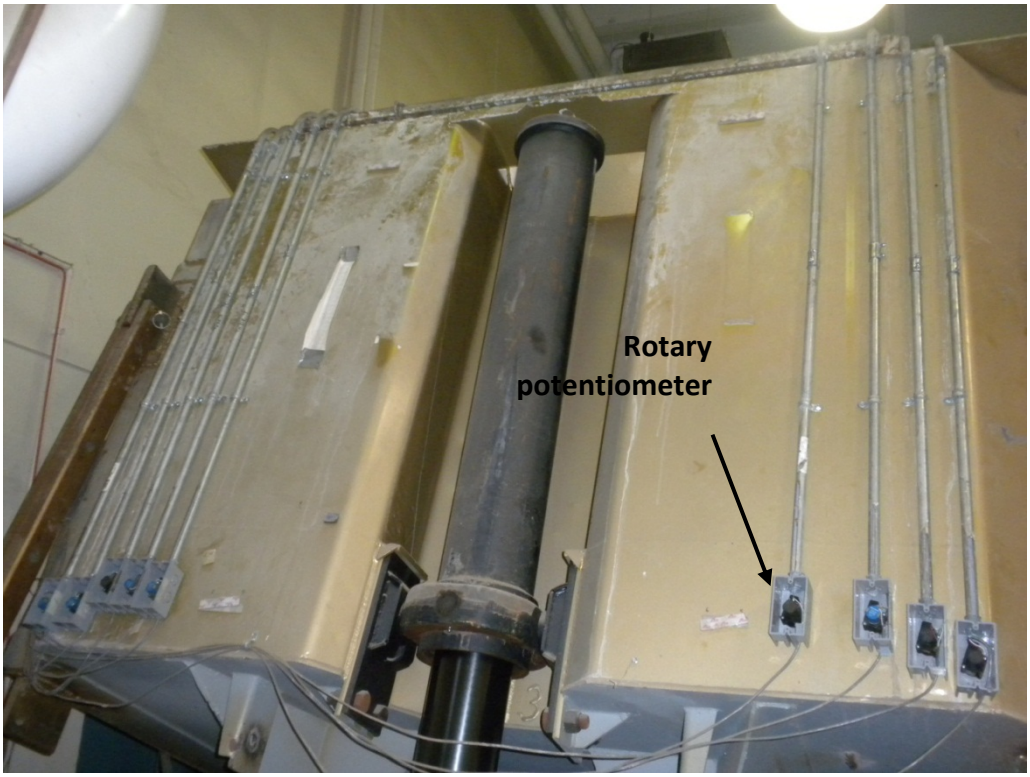

Figure 3.11 Location of potentiometers.

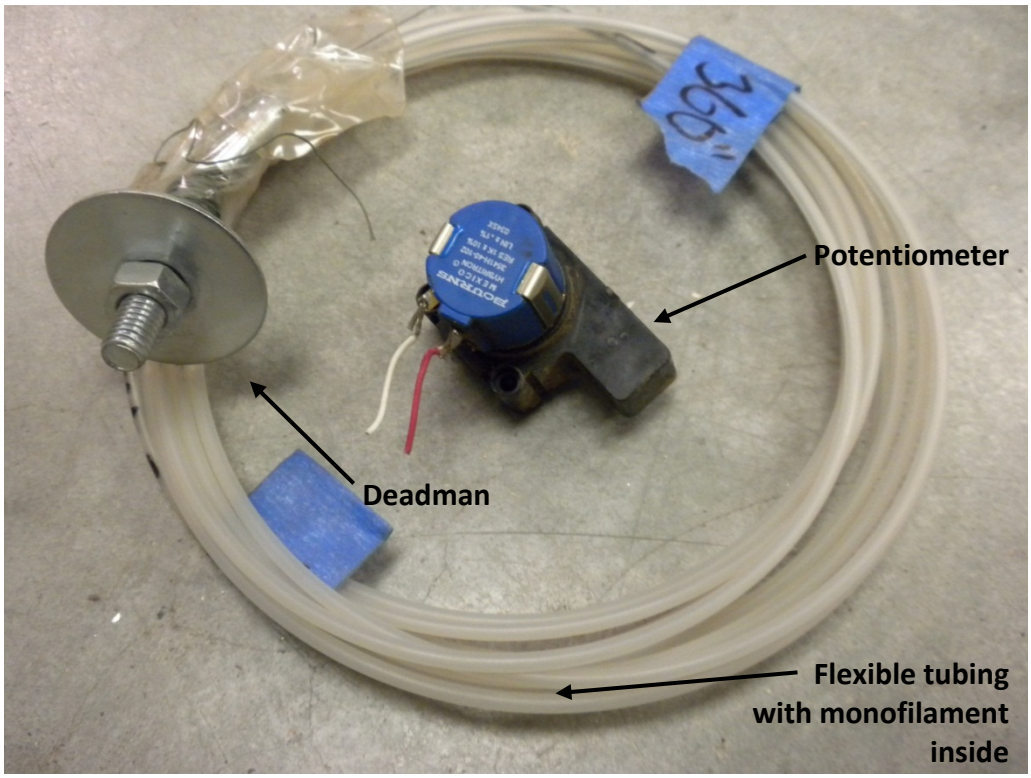

Figure 3.12 Extensometer and potentiometer.

3.2.2 Pore water pressure monitoring

Pore water pressures are crucial in the stability analysis of soil slopes. (Terzaghi, 1967). In this research project, it was imperative to obtain high quality pore water pressure data from the model soil. Precipitation and subsequent infiltration of water into the slope results in increased pore water pressure. Soilmoisture® tensiometers were used to measure the pore water pressures in the slopes. Detailed instructions for assembly, operation and configuration of the tensiometers are provided in Appendix A.

3.3 History of pore pressure for this research

Once the tensiometers and transducers were properly assembled and their accuracy and response was evaluated and corrected as described in Appendix A, the ceramic tips were kept under water until they were installed in the soil. Thus, depending on the position of the ceramic tip relative to the transducers, this caused a constant reading in tension or suction that had to be corrected. Figure 3.13 represents a typical behavior of the pore pressure as recorded with a tensiometer and transducer. The initial flat line in (a) represents the potential between the ceramic tip, submerged in water, and the transducer before placing it in the soil. It represents the hydrostatic pressure.

Once the ceramic tip is placed in the soil, the *matric suction* of the soil causes water to flow out of the tensiometer, creating a negative pressure in the tensiometer that the transducer registers and transforms into units of voltage. The suction is shown in (b) and increases until reaching an equilibrium point (c). This point of equilibrium is a coordinate corresponding to the water content of the soil were the ceramic tip is placed and the corresponding soil suction in the SWCC. It remains constant until the soil undergoes a change in the moisture content. After precipitation and infiltration begins, the water (wetting) front moves downward, reaching the location of the ceramic tip. At this location, the soil moisture content changes and the suction decreases (d). If it is considered that the SWCC is unique for each soil, it should be discussed whether the

suction and the wetting processes are also unique for the interaction between this particular soil and the tensiometer.

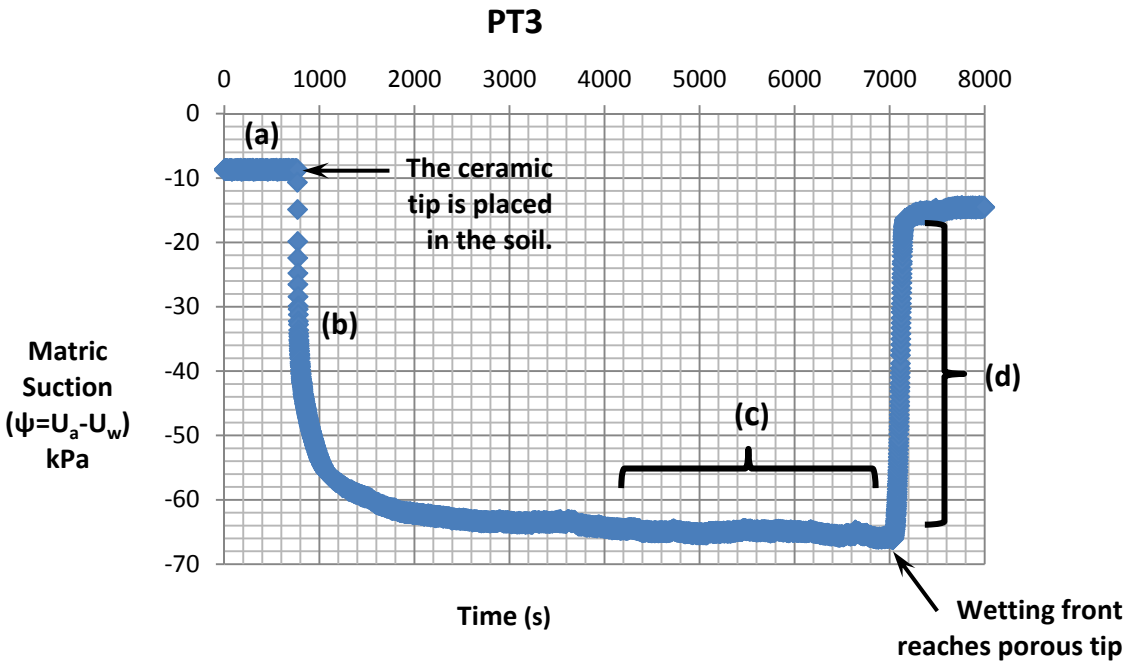

Figure 3.13 History of pore pressure described by a tensiometer and transducer during the test at a specific location.

3.4 Computation of corrections for Tensiometer-Transducer set

Once the ceramic tips are installed in the soil, the transducers are set to rest aside the dump bed container. Since the ceramic tips are located below the position of the transducer, this creates a potential reading that needs to be corrected for each transducer. Figure 3.14 shows the slope profile when built in polygon OABC and the same slope profile, when tilted in polygon OA'B'C'. This slope model pivots about point O. The ceramic tips are located at position 1, 2, 3 and 4, when built (Red) and after tilting it (Blue). The distance *d* is the correction to be calculated, when the slope is tilted, from the position of the transducers located at a position E and E' to any ceramic tip location. X1 is the distance measured from the edge of the dump bed container to the resting position of the transducer, when built and tilted, respectively. X2 is the horizontal distance from the pivot point O to the original position of the ceramic tips, H2 is the perpendicular distance from the bottom of the model slope to the ceramic tip, and H1 is the complement of the total height of the model slope at the distance X2. The slope is tilted to an angle of α. The angle λ is known and it is 25°. The angles θ and ɣ are unknown and β is the angle of slope failure or α plus 25°.

From the geometric arrangement shown in Figure 3.14 we have:

$$\boldsymbol{L = \sqrt{1.23^2 + X1^2}} \qquad \textbf{Equation 20}$$

$$L = Y1 + d \qquad \textbf{Equation 21}$$

$$From\ triangle\ \Delta IOF, \qquad tan\,\alpha = \frac{X3}{X2} \longrightarrow X3 = X2\tan\alpha \qquad \textbf{Equation 22}$$

$$From\ triangle\ \Delta FGH,\ \cos\alpha = \frac{Y1}{X3+h2} \longrightarrow Y1 = (X3 + h2)\cos\alpha \qquad \textbf{Equation 23}$$

Substituting Equation 22 in X3 of Equation 23

$$Y1 = (X2\tan\alpha + h2)\cos\alpha \qquad \textbf{Equation 24}$$

Clearing for *d* and substituting Equation 24 in Equation 21

$$d = \sqrt{1.23^2 + X1^2} - (X2\tan\alpha + h2)\cos\alpha \qquad \textbf{Equation 25}$$

Equation 25 represents the correction for potential *d* of any transducers located at a distance X1 and a ceramic tip located at a distance of X2 and H2, when the slope is

tilted an angle α from the pivot point O of the model slope. Note that the values of X1, X2, α and *h2* are known for each individual set of ceramic tips and transducers.

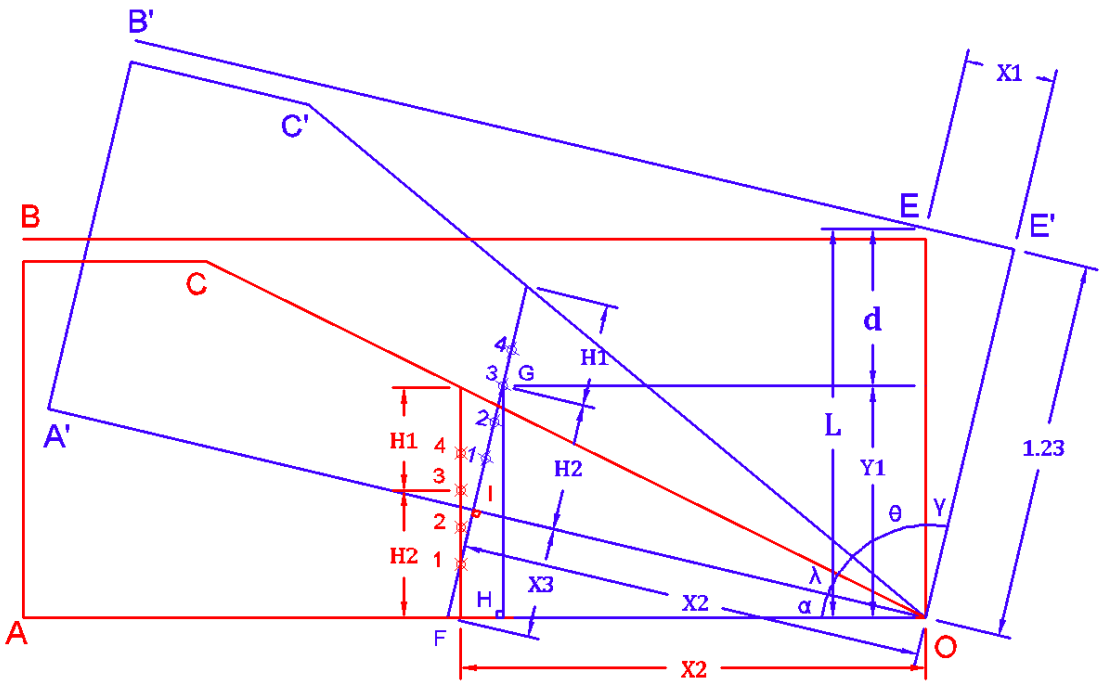

Figure3.14 Slope model as built and as tilted.

3.5 Soil Properties

Soil used for the model slopes is a silty sand dredged from the Missouri River near Jefferson City, Missouri. To characterize the soil, a series of index tests was performed in the University of Missouri geotechnical engineering laboratories (Boeckman, 2006). Results of all tests are summarized in Table 3.1. A plot of the grain size distribution is shown in Figure 3.15. Standard and reduced Proctor compaction curves are shown in Figure 3.16.

Figure 3.17 shows the graph of the Soil Water Characteristic Curve of the soil used in the lab and with the regression using the van Genuchten, 1980 model.

Table 3.1 Table with Soil Properties. (Boeckman, 2006).

Parameter	Value
ASTM Classification	SM
Plastic Limit	14
Liquid Limit	23
Plasticity Index	9
Organic Content	1%
Fines Content (percent passing #200 sieve)	19%
Maximum Dry Unit Weight, Standard Proctor	120pcf
Optimum Water Content, Standard Proctor	11%
Maximum Dry Unit Weight, Reduced Proctor	115pcf
Optimum Water Content. Reduced Proctor	12%
Drained Angle of Internal Friction, 18% water content	36°
Drained Angle of Internal Friction, 10% water content	33°
Effective Stress Cohesion Intercept, 18% water content	70psf
Effective Stress Cohesion Intercept, 10% water content	70psf

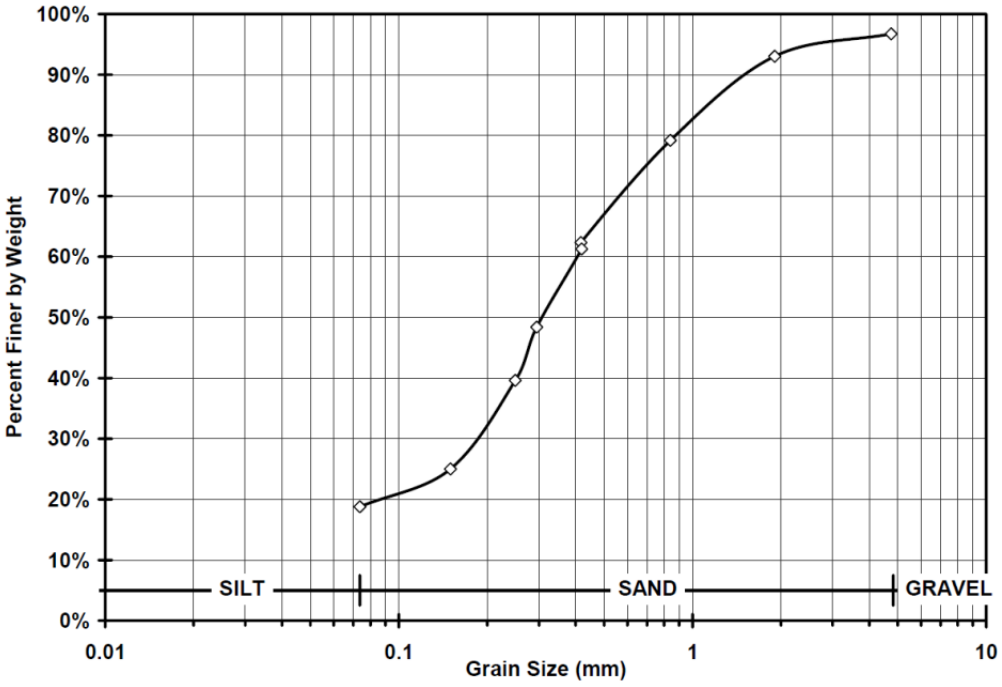

Figure 3.15 Graph of grain size distribution of soil used in models. (Boeckman, 2006).

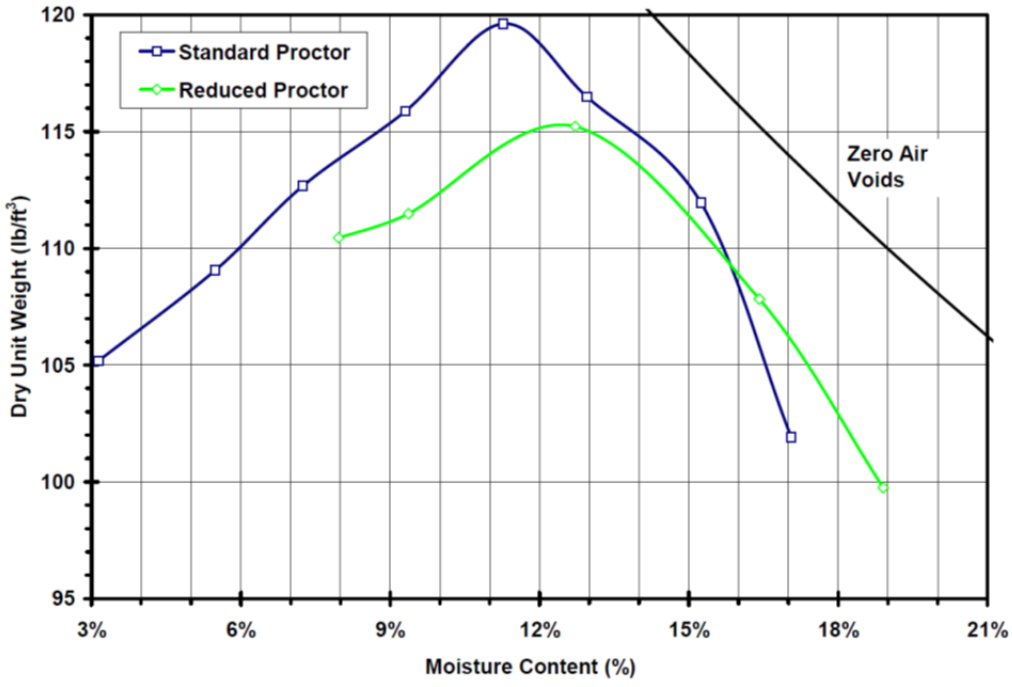

Figure 3.16 Proctor graph of soil used in model soils. (Boeckman, 2006)

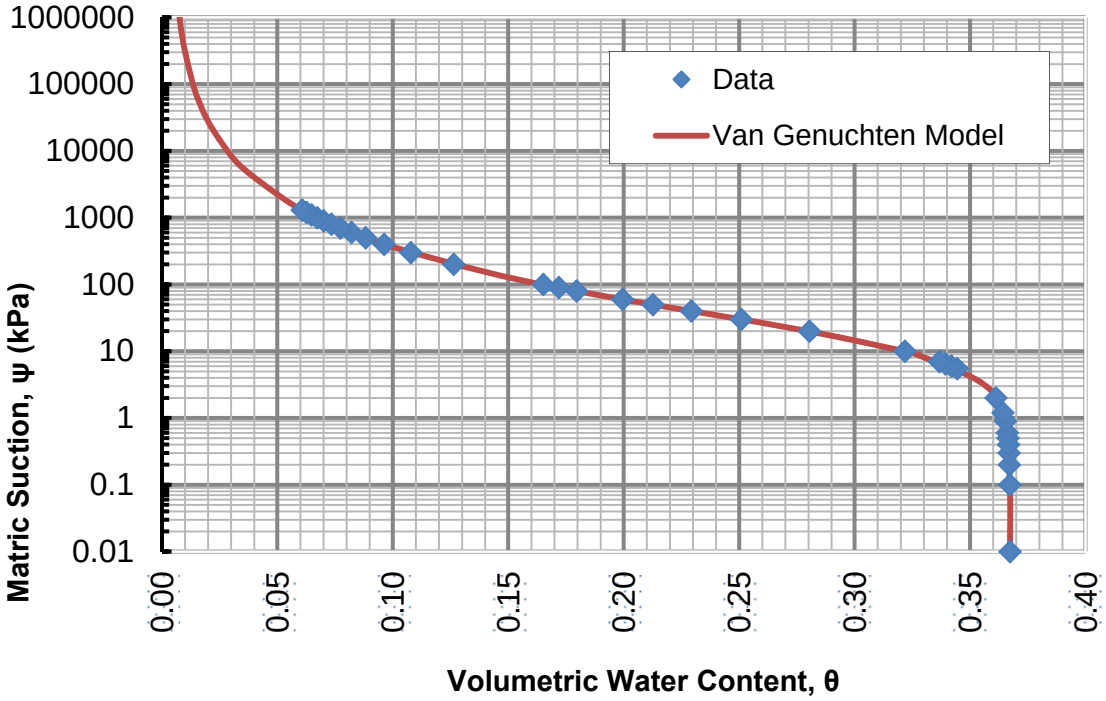

Figure 3.17 Regression model of soil Using Van Genuchten Model. (McKee, 2012)

3.6 Saturated Hydraulic Conductivity

The saturated hydraulic conductivity was measured in the geotechnical lab. The saturated hydraulic conductivity is a function of the SWCC. (Mitchell and Soga, 2005). Figure 3.18 shows the setup of the instruments when conducting the test and Figure 3.19 show a soil sample in the permeameter. As explained in Section 2.7, the saturated hydraulic conducivity complements Equation 11 for the calculation of the unsaturated hydraulic conductivity.

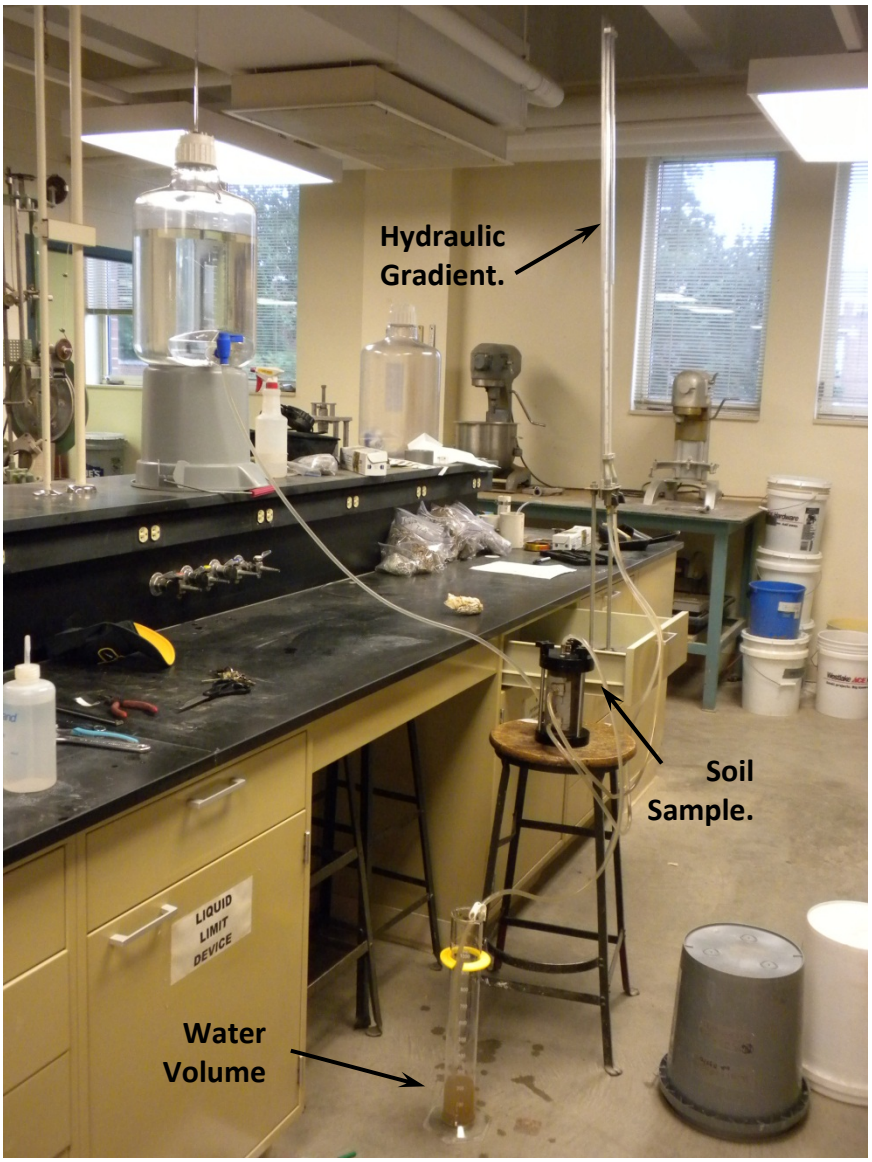

Figure 3.18 Set up of instruments to measure saturated hydraulic conductivity.

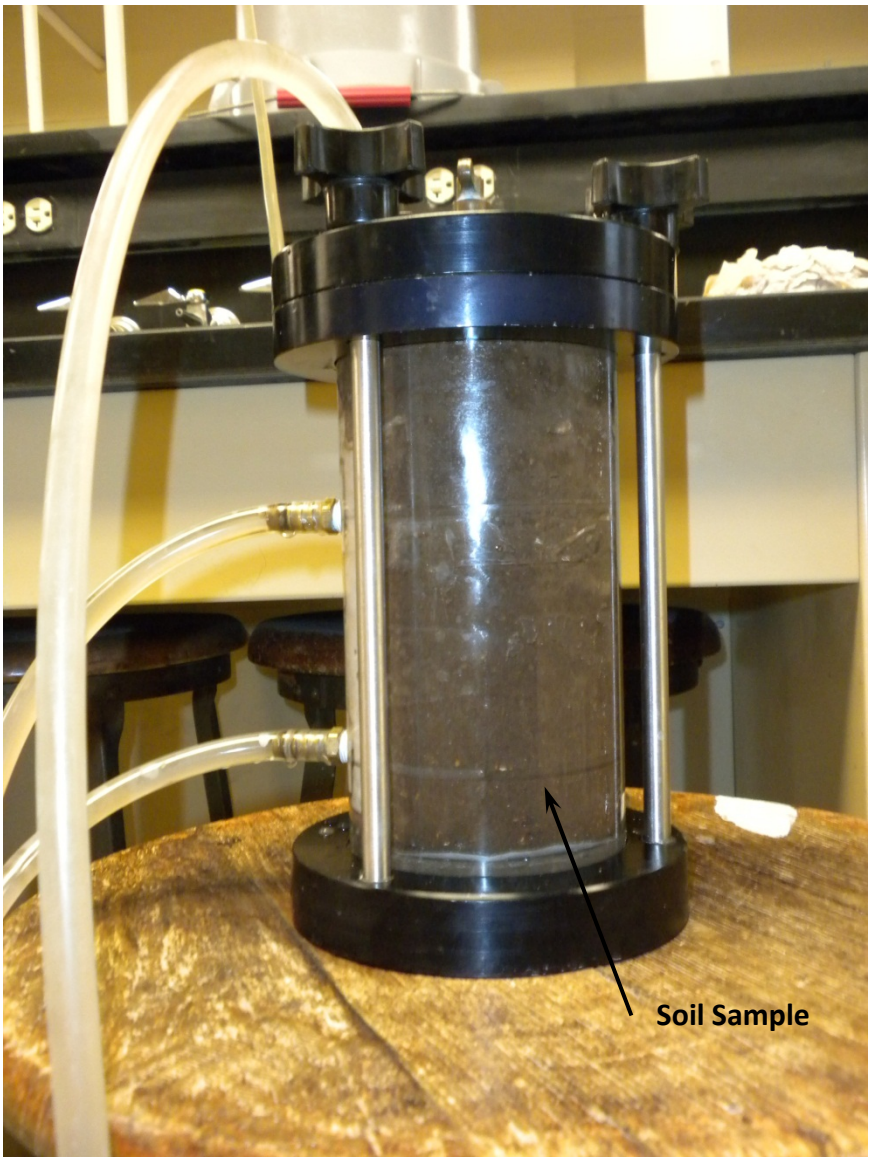

Figure 3.19 Sample of soil in permeameter.

3.7 Slope Testing Procedure

This section contains the three major steps followed in each slope test: model construction, model testing procedure and forensic analysis.

3.7.1 Model construction

Three model slope tests were conducted during this experimental program; the first test was under the direction of visiting scholar Professor Sun-Chi Hsu from the Department of Construction Engineering, Chaoyang University of Technology, in Taiwan and the other two slopes, under the author's supervision. The first test was built following the same procedure performed by Boeckman (2006) and Deeken (2005). The procedure consisted of tilling the soil to eliminate large clods of soil and to provide uniform moisture to the soil (Figure 3.20).

Figure 3.20 Preparation of soil for uniform moisture content prior to placement and compaction.

It was desired to work on the dry side of the optimum moisture content (OMC) thus; frequent verification of the moisture content was performed. Once the appropriate moisture content was reached, the soil was placed in lifts of approximately 20 cm. Figure 3.21 shows the process of placing the soil in the dump bed and Figure 3.22 shows the lifts being placed. Each lift was compacted with three passes of a 400-lb smooth drum roller until reaching a slope angle of 25° (Figure 3.22). The drum is pulled; up and down, through a pulley operated with a motor mounted in a reaction frame (Figure 3.22). The edges of each lift were compacted with a 25-lb hand compactor being careful not to hit the tubing from the sensors (Figure 3.23). As the lifts were built, the instrumentation was installed in the pre-established locations (Figure 3.24). For the third slope SL3, the soil was directly discharged from the Bobcat loader into the dump bed container. Next, the soil was spread out with rakes and compacted. This procedure was followed for the first 50 cm of fill; the rest of the slope was constructed following the same procedure of the previous two tests (SL1 and SL2). The instrumentation was installed after the soil slope was completed for the second and third slopes.

Figure 3.21 Placement of soil in model container.

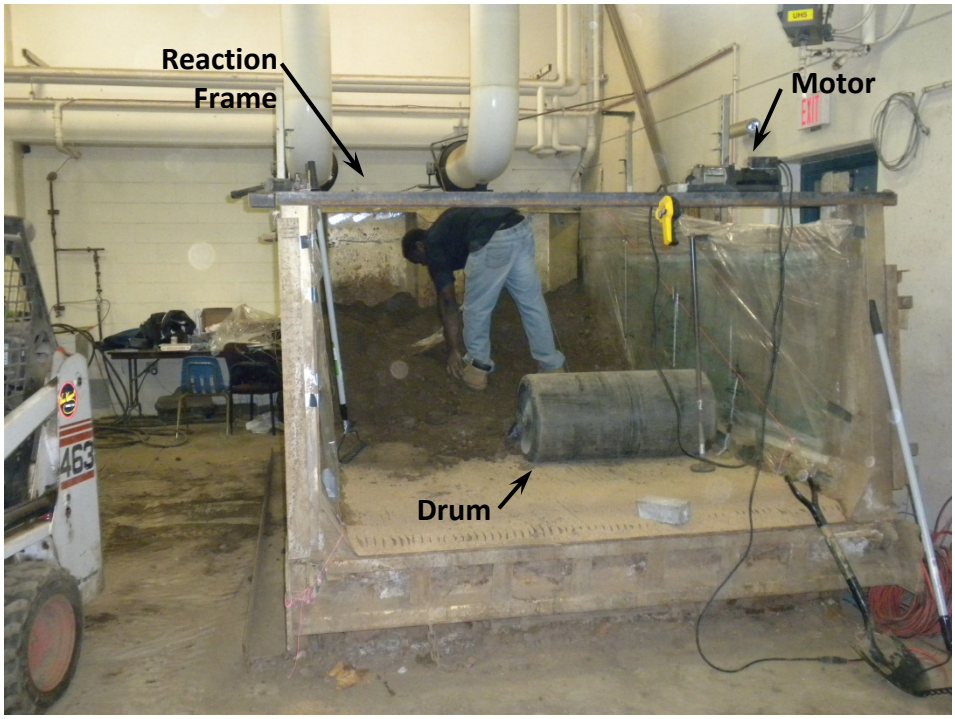

Figure 3.22 Lifts of soil being placed and compacted.

Figure 3.23 Hand compacting of soil along the edges of the container.

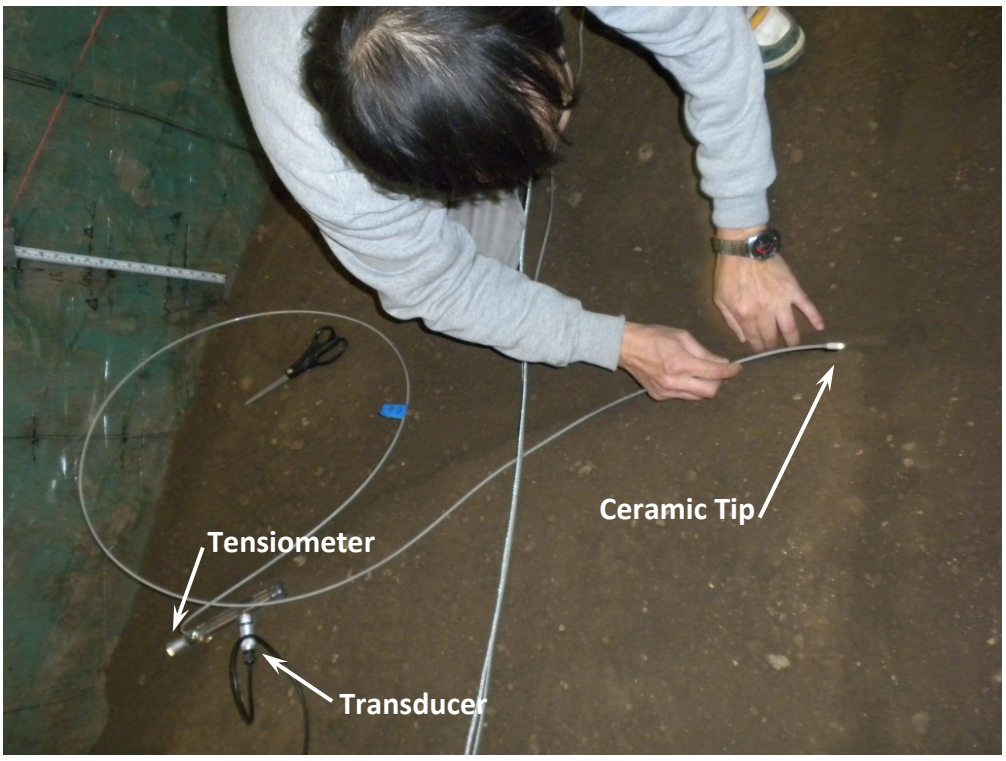

Figure 3.24 Installation of ceramic tip for a tensiometer.

3.7.2 Model testing procedure

The slopes were built to a surface slope of 25°, and then tilted to steeper angles, while receiving the precipitation, until failure. Time was allowed for the pore water pressures to reach equilibrium (Figure 3.13 part (c)). Once equilibrium was reached, the rain process was started. The first slope was rained on continuously while at a constant slope angle of 40° until failure. The second test was rained on cyclically (10 minutes on followed by 10 minutes off). The slope angle was then increased one degree per day while receiving precipitation until failure. The third test was subjected to a rain cycle of 13 minutes on followed by 10 minutes off, and then the slope was tilted until 45°. The rain was continued for another five days and then the rain was shut off until failure.

During each slope test, the slope was monitored using a video recorder. Figures 3.25 to 3.28 show 3D views of the soil slope model test with the distribution of the instruments in the soil slope before and during testing and the precipitation system and connections to the computer.

3. 7.3 Demolition and Forensic Analysis

The shape of the slope failure was studied after each slope failed. Coordinates of the failed surface were measured in order to compare the observed versus the predicted surfaces.

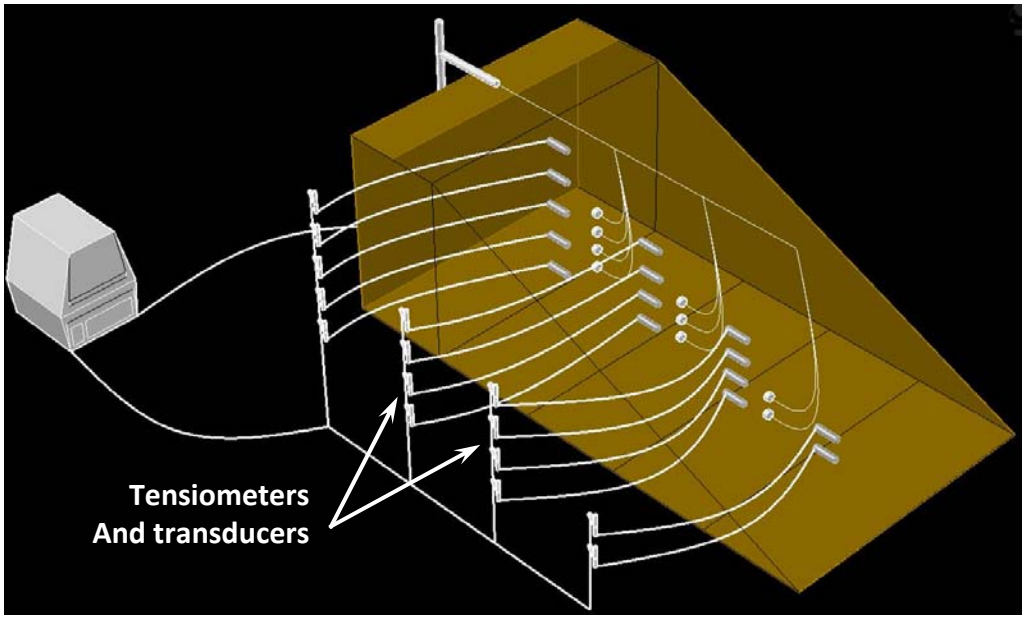

Figure 3.25 3D View of layout of instruments installed in model slope.

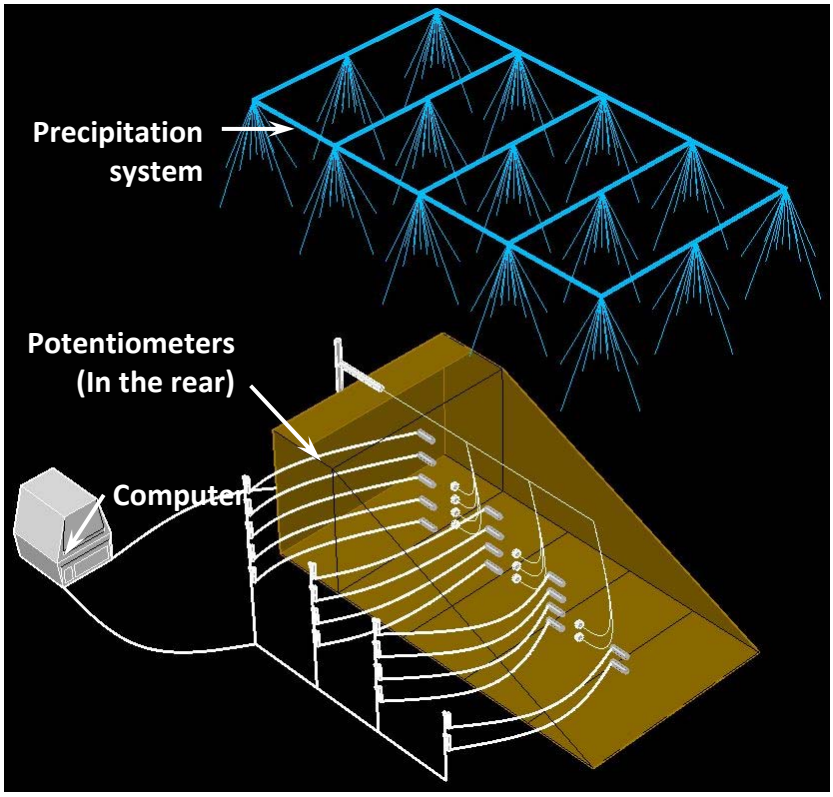

Figure 3.26 3D View of the precipitation system.

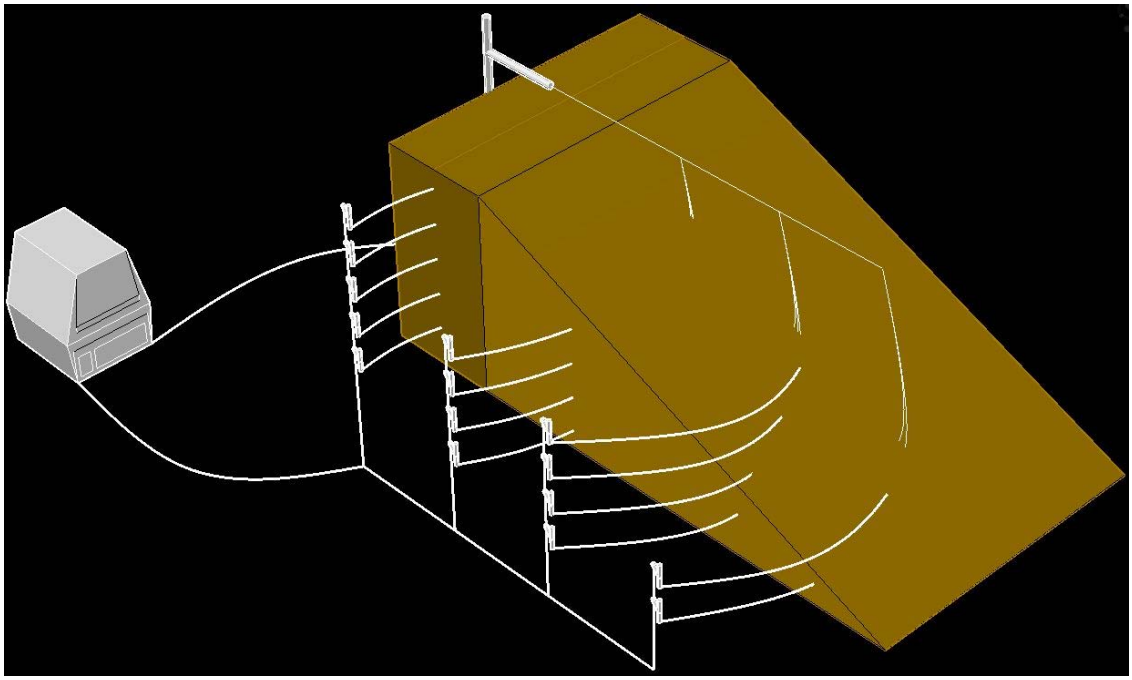

Figure 3.27 3D view of slope before testing.

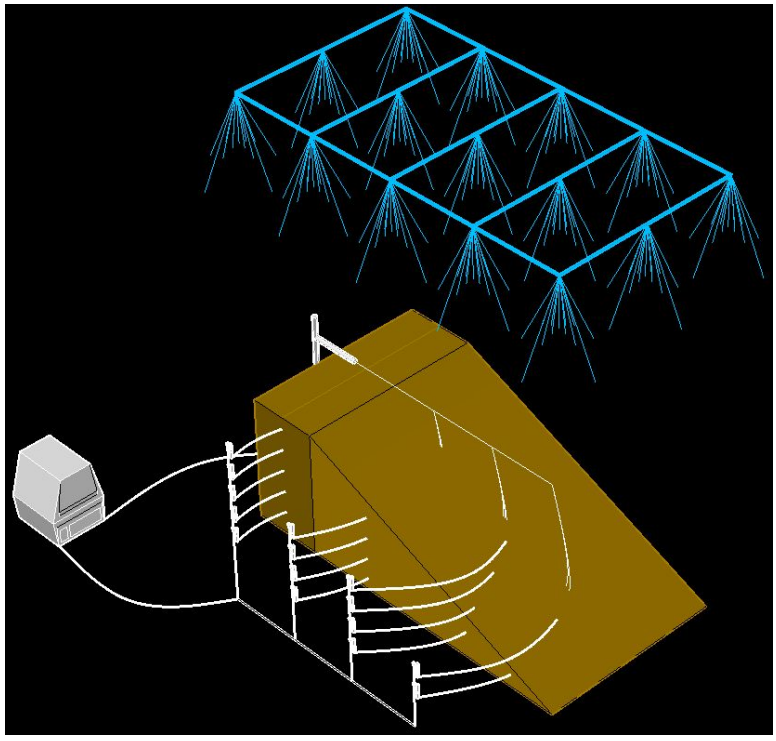

Figure 3.28 3D View of slope during testing.

CHAPTER 4 MODEL TESTS AND RESULTS

4.1 Testing program

Three model slopes were constructed, tested and analyzed in order to develop this thesis. The first model was subjected to continuous rain, in order to cause saturated conditions in the soil. The next two models were subjected to cyclical periods of rain in order to allow drainage and to cause failure of the slope in unsaturated conditions of the soil.

4.2 Results for Hydraulic Computations and Measurements

The hydraulic conductivity explains how water moves through a soil. As the soil becomes wetter, the hydraulic conductivity increases, thus the speed at which the water infiltrates in the soil; hence the need to model the hydraulic conductivity from the Soil Water Characteristics Curve (SWCC).

4.2.1 Regression model for Soil Water Characteristic Curve (SWCC)

In order to develop the computations explained in Chapter 3, a mathematical model for the SWCC is needed. To do so, a regression model was developed for the data

obtained in the lab and provided by previous research by Dr. William Likos, (University of Wisconsin-Madison formerly University of Missouri faculty).

Figure 3.17 shows SWCC with the fit line using the van Genuchten model. The data for the fit line corresponding to the original curve was obtained from McKee, 2012. Table 4.1 shows the values corresponding to the fit line for Equation 26. These values are used to establish the unsaturated hydraulic conductivity.

Table 4.1. Table of values for fit line for SWCC.

Parameters	θ-ψ n=0.40 Original curve	ω-ψ n=0.40 Primitive curve	ω-ψ n=0.272 Test 2	ω-ψ n=0.272 Test 3
θ_r =	0.0040	0.0043	0.0043	0.0043
θ_s =	0.3673	0.3673	0.3673	0.3673
α =	0.0679	0.0678	0.0679	0.0679
n =	1.4143	1.4151	1.4151	1.4151
m =	0.2929	0.2933	0.2933	0.2933

$$\boldsymbol{S_e = \frac{\theta - \theta_r}{\theta_s - \theta_r} = \left[\frac{1}{1 + (\alpha\psi)^n}\right]^m} \qquad \textbf{Equation 26}$$

Substituting values from Table 4.1 for n=0.272

$$\boldsymbol{S_e = \frac{\theta - 0.0040}{0.3633} = \left[\frac{1}{1 + (0.0679\psi)^{1.4143}}\right]^{0.2929}} \qquad \textbf{Equation 27}$$

Or

$$S_e = \theta = 0.3633 * \left[\frac{1}{1 + (0.0679\psi)^{1.4143}}\right]^{0.2929} + 0.0040 \qquad \textbf{Equation 28}$$

Were ψ is the Matric Suction.

4.2.2 Unsaturated Hydraulic Conductivity

The configuration for the unsaturated hydraulic conductivity (Mitchel and Soga, 2005) of the soil used in the model test is:

$$k_r(\theta) = \left(\frac{\theta - \theta_r}{\theta_s - \theta_r}\right)^q \left\{1 - \left[1 - \left(\frac{\theta - \theta_r}{\theta_s - \theta_r}\right)^{\frac{1}{m}}\right]^m\right\}^2 \qquad \textbf{Equation 29}$$

Substituting values from Table 4.1

$$k_r(\theta) = \left(\frac{\theta - 0.0040}{0.3633}\right)^{0.50} \left\{1 - \left[1 - \left(\frac{\theta - 0.0040}{0.3633}\right)^{\frac{1}{0.2929}}\right]^{0.2929}\right\}^2 \qquad \textbf{Equation 30}$$

Where Θ is the volumetric water content.

Figure 4.1 is a graph of the unsaturated hydraulic conductivity versus volumetric water content of the soil model.

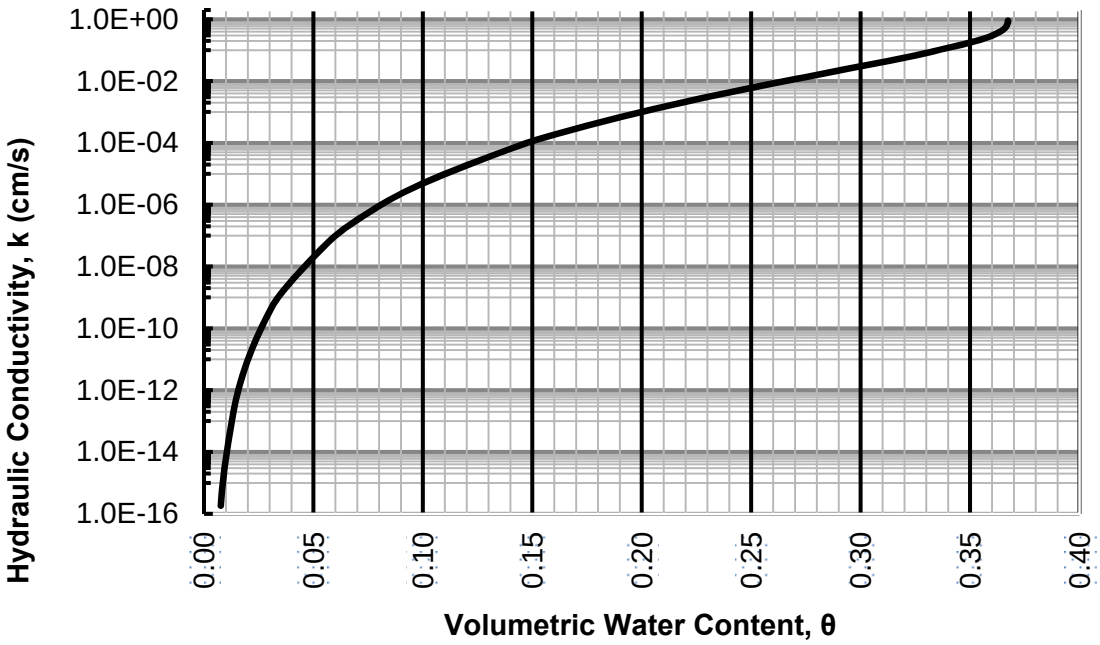

Figure 4.1 Unsaturated hydraulic conductivity for the soil used in the model slope.

4.2.3 Saturated Hydraulic Conductivity Function

The saturated hydraulic conductivity was calculated after performing five permeability tests. The results are summarized in Table 4.2. Figure 4.2 shows the graph of these values. The saturated hydraulic conductivity for the soil is the slope of the line from Figure 4.2 and the corresponding value is *K=0.015 cm/s or* $1.5x10^{-2}$ *m/s.*

Table 4.2. Saturated hydraulic conductivity test data from constant head test on the silty sand used to construct the slopes.

Test	Δh (cm)	i	Q (cm^3)	Time (s)	V (cm/s)
1.0	-	-	-	-	-
2.0	4.00	0.52	100.00	283	0.0077
3.0	3.50	0.46	50.00	290	0.0038
4.0	2.20	0.29	50.00	342	0.0032
5.0	2.20	0.29	50.00	349	0.0031

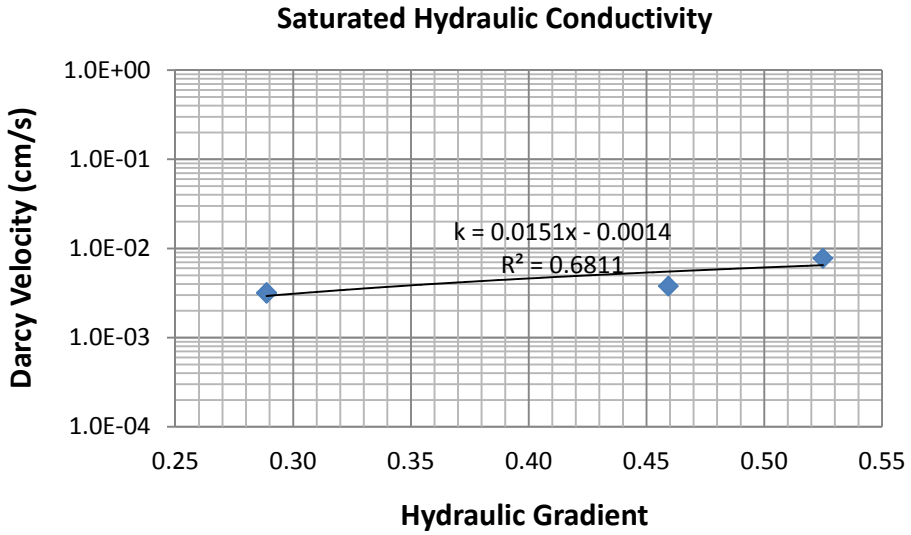

Figure 4.2 Measured saturated hydraulic conductivity of the silty sand used to construct the slopes.

4.3 Relationship between θ and ω in the Soil Water Characteristic Curve (SWCC)

The SWCC was presented by McKee, (2012) in a form of volumetric water content to matric suction or **Θ-ψ** relationship. In order to compute the factor of safety shown in Equation 31, this relationship must be converted to gravimetric water content to matric suction or **ω-ψ** relationship. Therefore, it is necessary to find the relationship between the volumetric water content and the gravimetric water content. More detail of how this relationship was derived is included in Appendix A.

4.4 Calculations of factor of safety

Equation 31 was used to calculate the factor of safety against failure of the model slopes. The equation is composed of Equation 1, which is transformed, by using Equation 8 and Equation 17, from Sections 2.6 and 2.9 respectively. The calculations were repeated for every one of the fifteen transducers. More details of these calculations are provided in Appendix A. The method was used for SL2 and SL3 only. Test SL1 was analyzed by Hsu et al, 2013.

$$F = \frac{S}{\tau} = \frac{c' + [(\sigma - U_a)_f + \chi_f (U_a - U_w)_f] \tan \phi'}{\gamma_d (1 + \omega) Z \cos \beta \sin \beta} \qquad \textbf{Equation 31}$$

4.5 Results for Soil Model Slopes

In this section, results from each test are analyzed. The first test analysis is a summary of Hsu et al. 2013 publication; the next two tests (SL2 and SL3) are the author's analysis using the concepts presented in the literature review (Chapter 2).

4.5.1 Model Slope SL1.

The first slope (SL1) was built with a slope angle of 25° and later tilted until a constant slope angle of 40°; then it was rained on until collapse. The results of first test (SL1) showed that a soil slope can easily fail under rainfall conditions. The failure started from the toe and retrogressed upslope as was caused by increase in pore water pressure due to the precipitation as it infiltrated into the soil. Initially, there was a consolidation of the whole mass of soil caused by the seepage forces. When the water percolates through soil in a downward direction, it produces a drag force between the percolating water and the surface of the soil particles, dragging the soil particles downwards, compacting and increasing the density of the soil.

Figure 4.3 shows a vertical profile with the location of the tensiometers in the soil model, and Figure 4.4 shows the graphs of the change in the suction with depth and time as measured with the pore pressure tensiometers located in the slope. Tensiometers 1 to 5 were installed near the crest of the slope. After 310 minutes of rain, the pore pressure increases from negative values to zero in tensiometer 5 located at 20 cm below the surface. After 1000 minutes of rain, the pore pressure in tensiometer 1

located 65 cm below the surface, increased to zero. Tensiometers 11 to 15 were installed close to the toe of the slope (Figure 4.5). Tensiometers, 11 to 15 were installed 9 cm below the surface and increased to zero pore pressure after 200 minutes of rain. The bottom tensiometer located 27 cm below the surface increased to zero pore pressure after about 400 minutes.

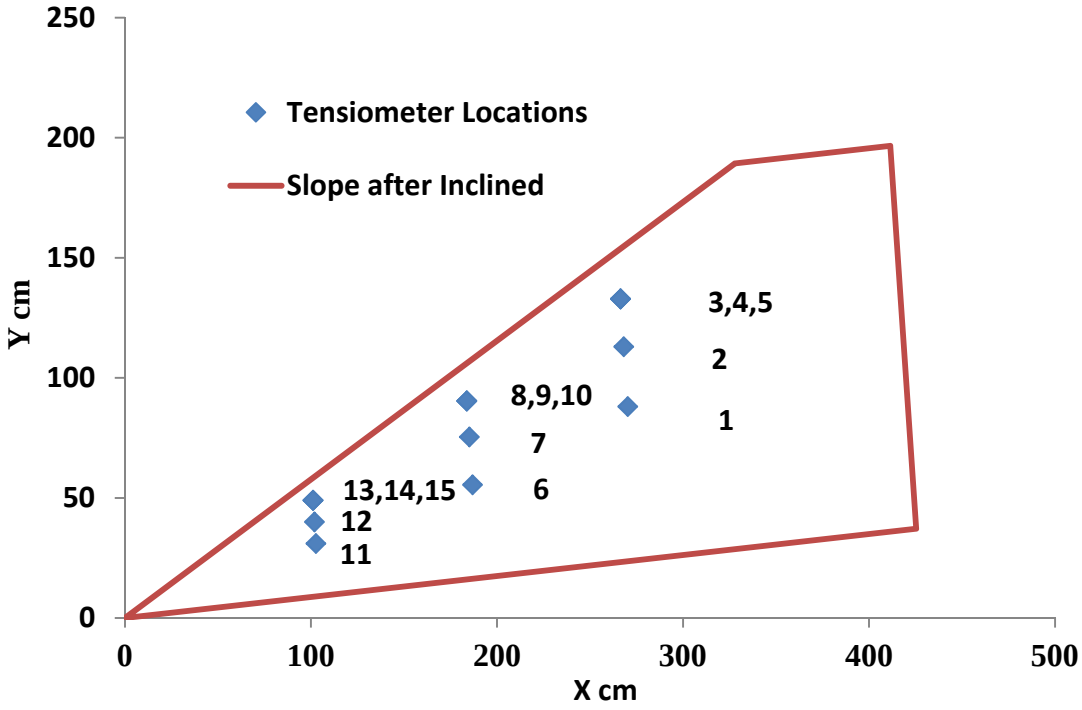

Figure 4.3 Locations of the Tensiometers for SL1. (Hsu et all, 2013)

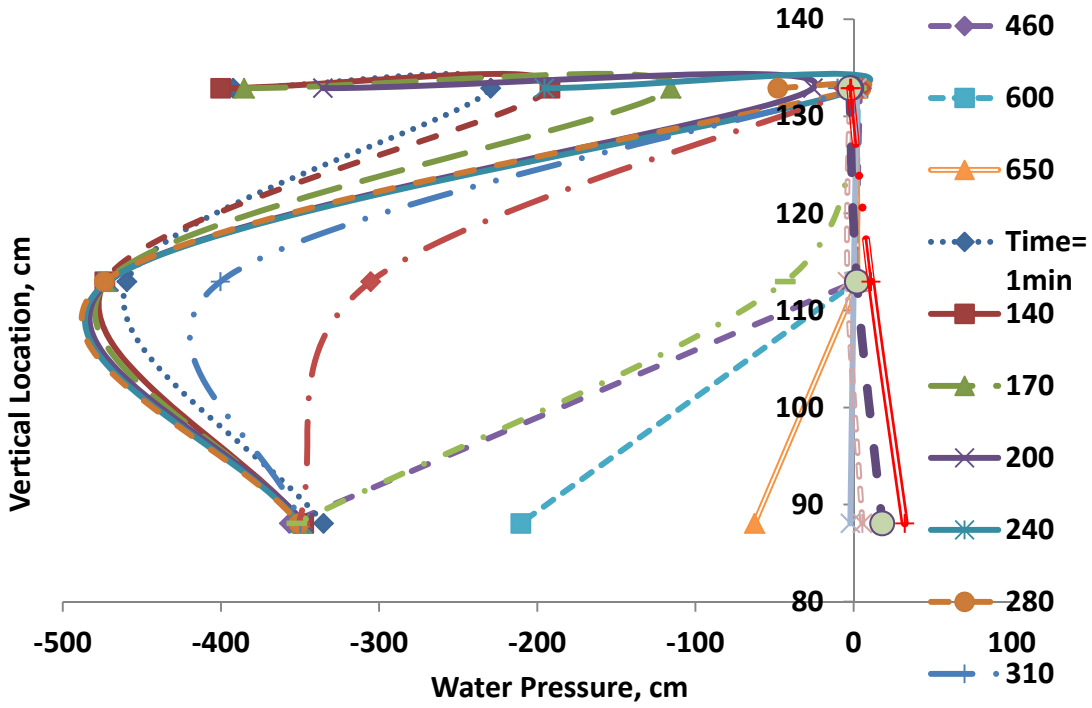

Figure 4.4 Change of pore pressures in tensiometers SL1. (Hsu et all, 2013)

After 20 hours of precipitation, a densification occurred and cracks started to appear at the crest of the slope. Picture 4.5 and 4.6 show this densification and the initial crack.

Four stages of failure could be observed from this test. The first stage of failure occurred after 67 hours of continuous precipitation and consisted of small toe failure; this landslide is shown in the pictures of Figure 4.7 and 4.8.

The second stage of failure occurred after 109 hours of precipitation. It is shown in Figure 4.9. The third stage of failure occurred after 111 hours of precipitation and it is shown in the picture from Figure 4.10 with only two hours of difference from the second stage of failure.

The fourth and last stage of failure occurred after 115 hours of precipitation. It is shown in the pictures of Figures 4.11 and 4.12 with only four hours after the previous third stage of failure.

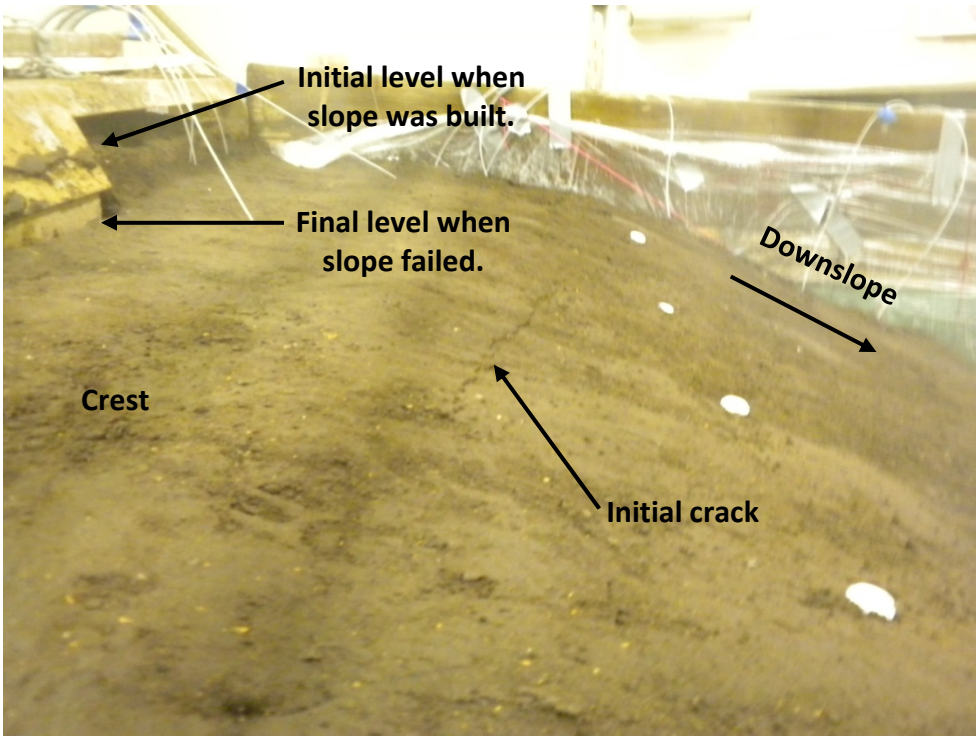

Figure 4.5 Marks of consolidation and initial crack.

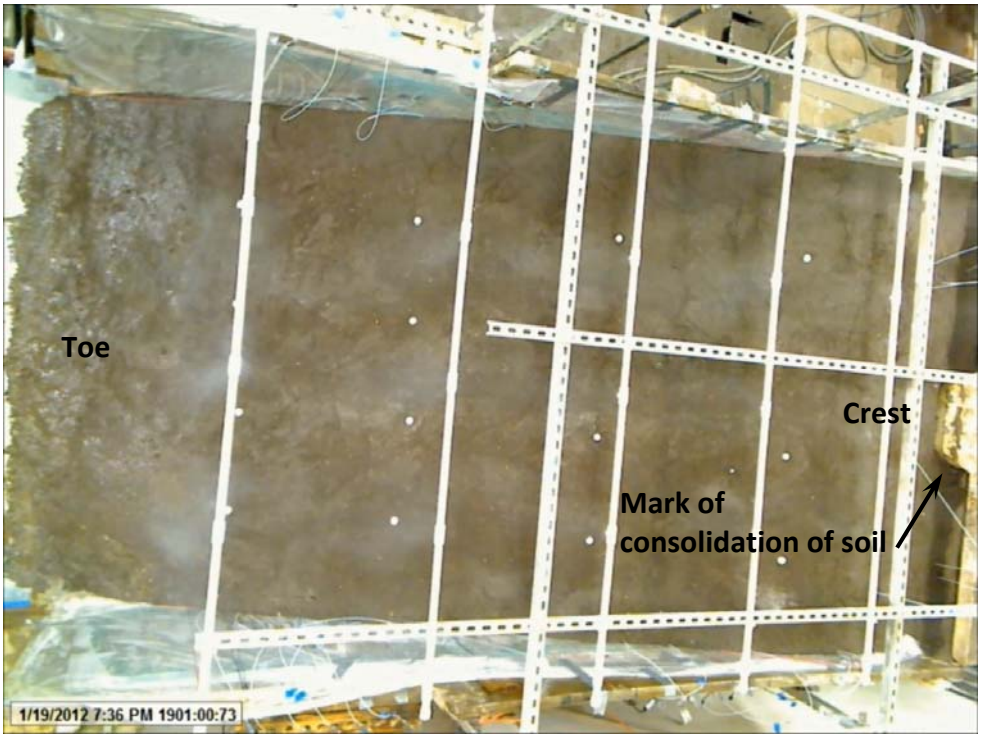

Figure 4.6 Top view of marks of consolidation.

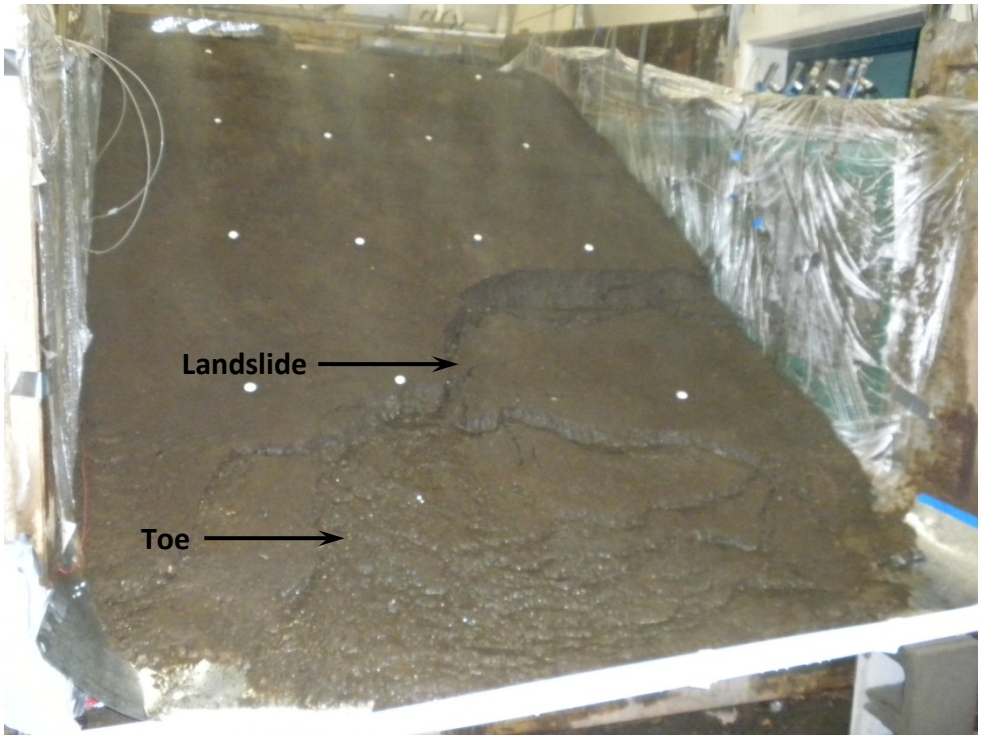

Figure 4.7 Initial stage of failure after 67 hours of precipitation SL1.

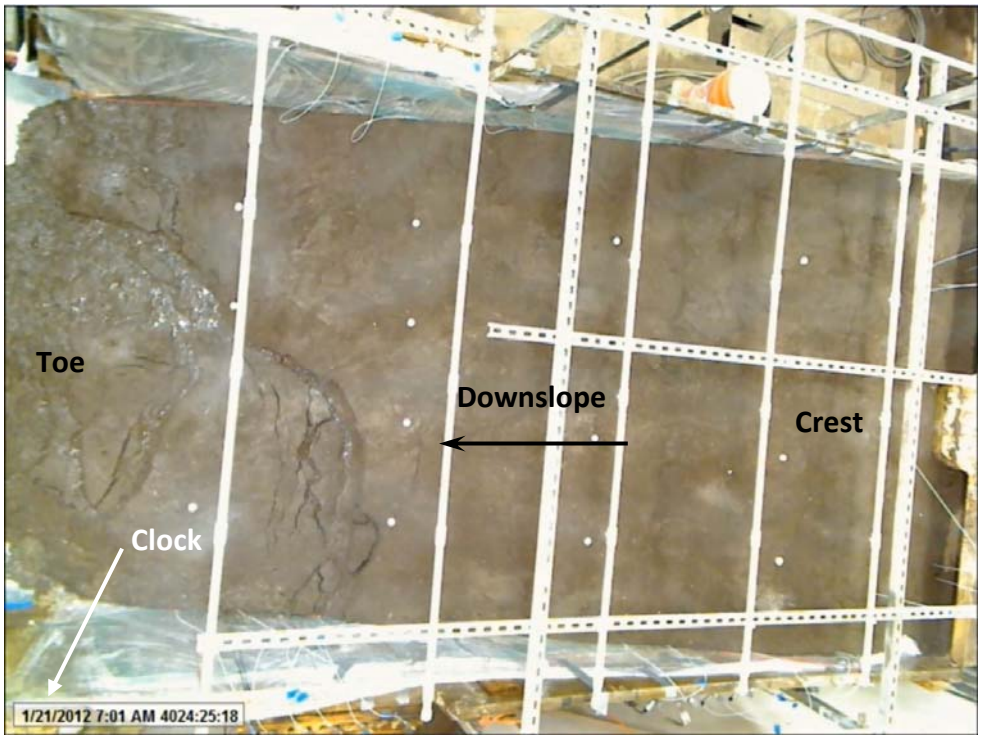

Figure 4.8 Top view of the initial stage of failure SL1.

Figure 4.9 Top view of second stage of failure SL1.

Figure 4.10 Top view of third stage of failure SL1.

Figure 4.11 Top view of last stage of slope failure SL1.

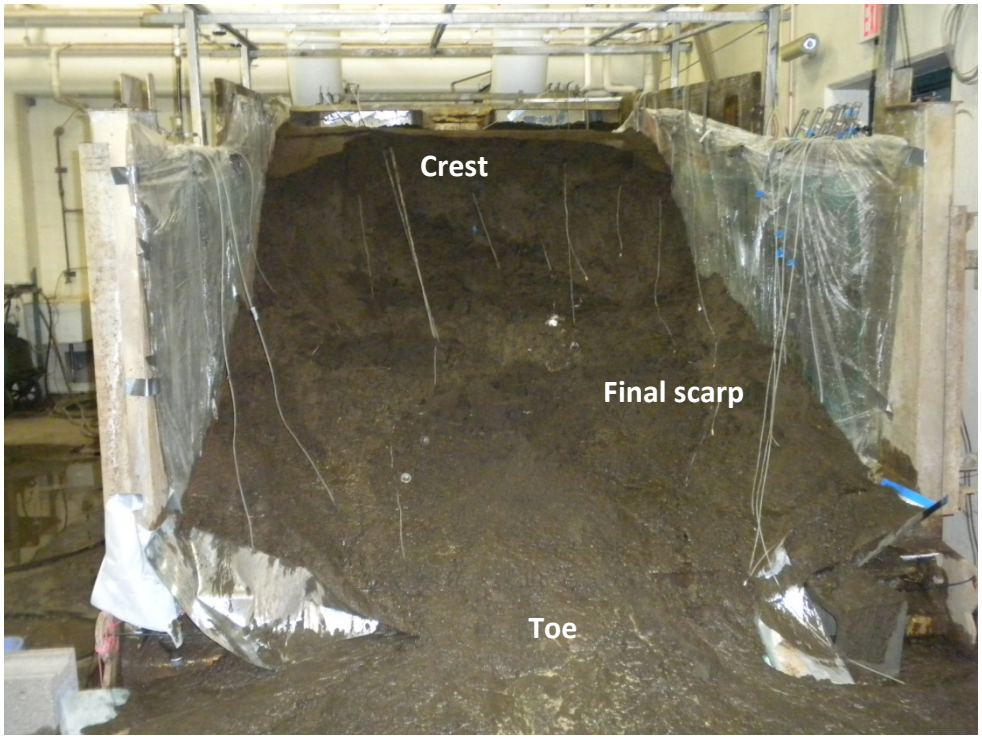

Figure 4.12 Front view of the last stage of failure SL1.

4.5.2 Model Slope SL2

The second model slope was also built at a slope angle of 25° which was later increased to 40°. Figure 4.13 shows the distribution of the instruments throughout the slope. The slope was rained on using a cycle of 10 minutes on constant rain and followed by 10 minutes off. After a month of rain, no failure occurred, and the angle of the slope was increased at a rate of one degree every day and the rain cycle was continuous. Failure occurred after seven days of rain at a slope angle of 47°. Figure 4.14 shows a comparison of a circle of radius of 521 cm with points measured on the soil slope after failure (Figure 4.16 to Figure 4.23). Although some different geotechnical characteristics were observed among the first (SL1) and the second test (SL2), the cracks and the pre-failure consolidation were still observed in the same magnitude and appearance. Figure 4.24 shows the lowest calculated factor of safety across the slope. The lowest calculated factor of safety of 1.0 was located near the slope surface (Fig, 4,24) which is consistent with the observed zone of failure.

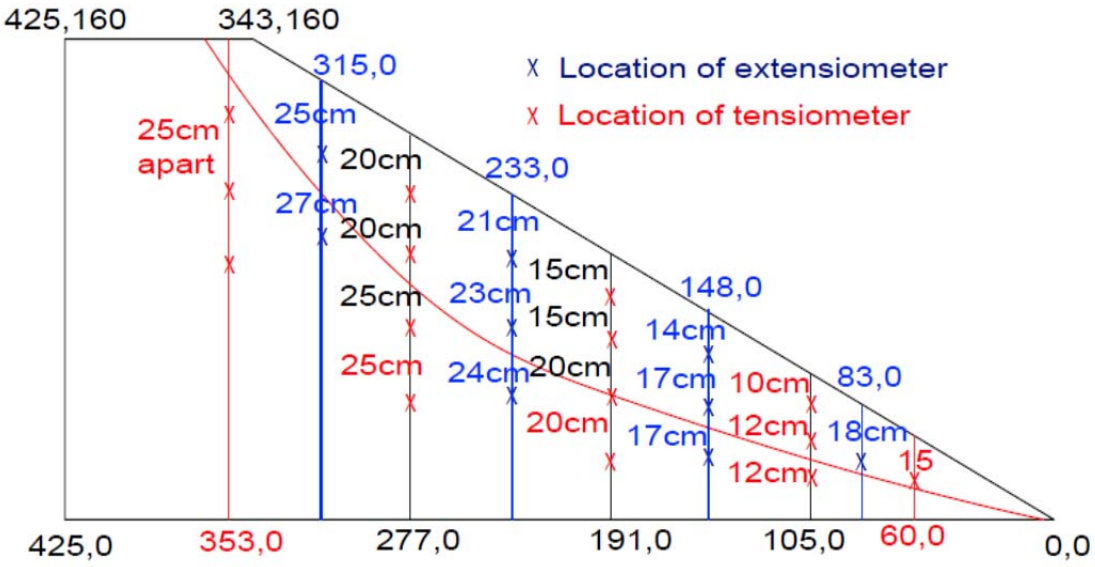

Figure 4.13 Location of instruments SL2. (Provided by Dr. Hsu)

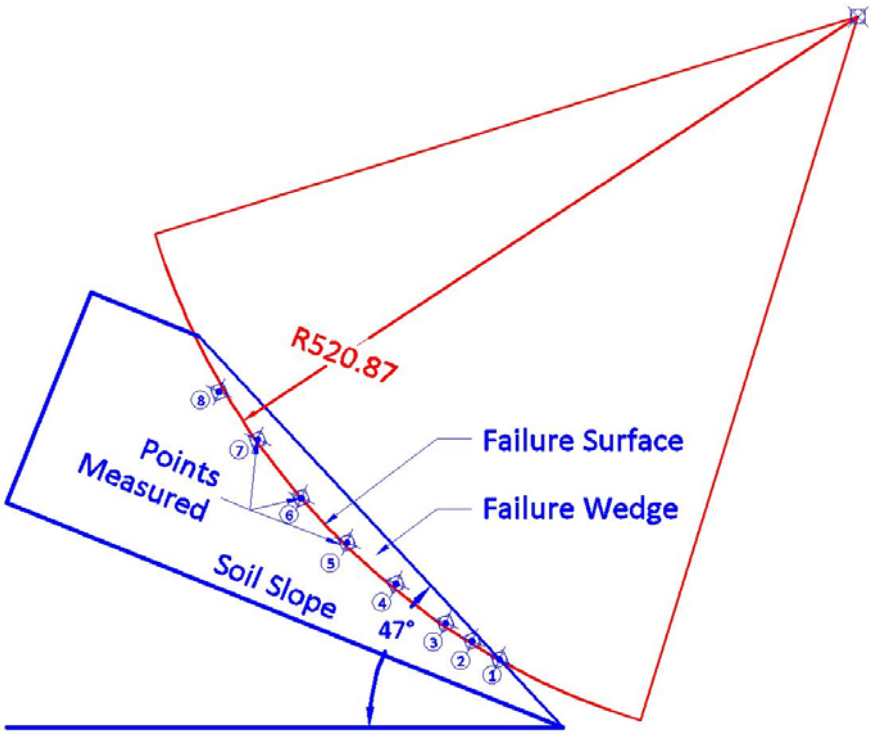

Fig 4.14 Comparison of circular shape with points measured at the slope test SL2. Points 1 to 8 were measured as seen in Figures 4.14 to 4.21.

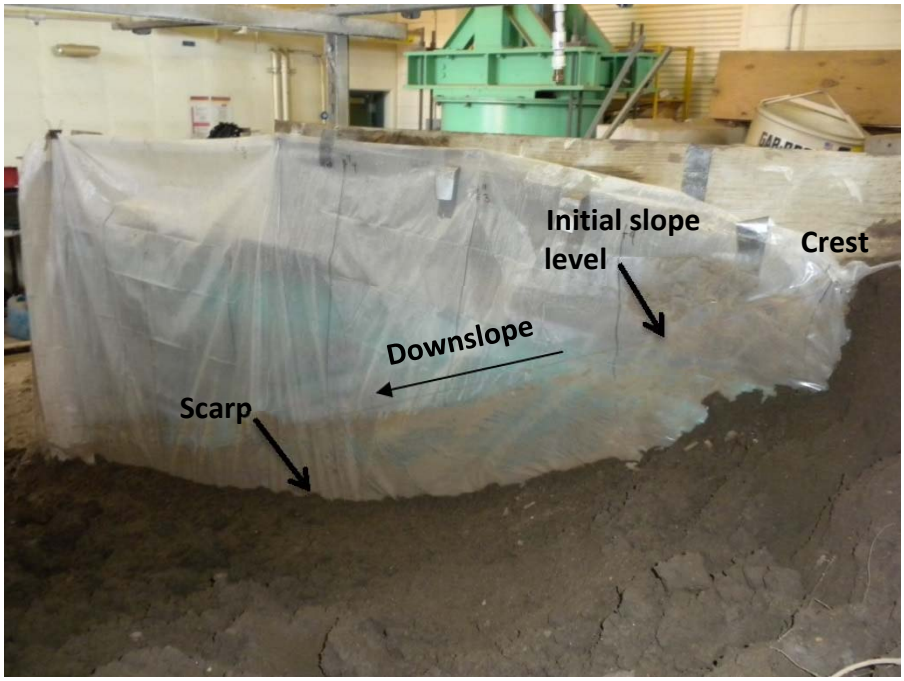

Figure 4.15 General view of failure shape SL2.

Figure 4.16 Point 1 in Figure 4.14. SL2

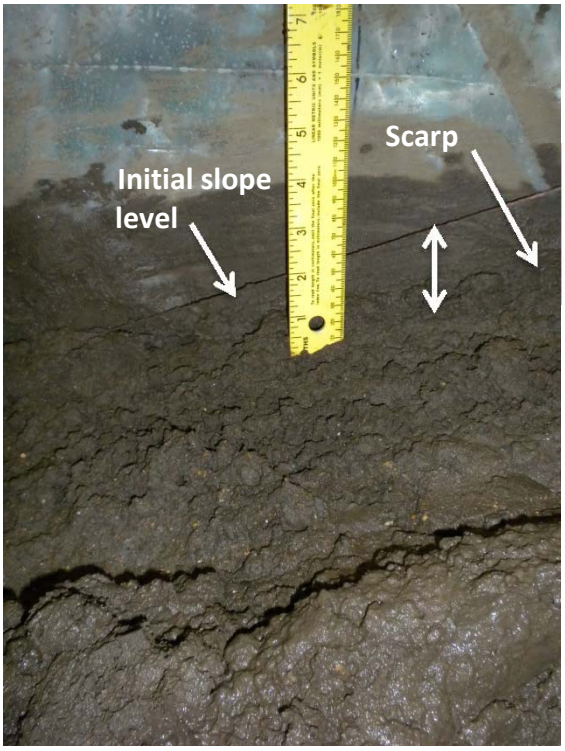

Figure 4.17 Point 2 in Figure 4.14. SL2

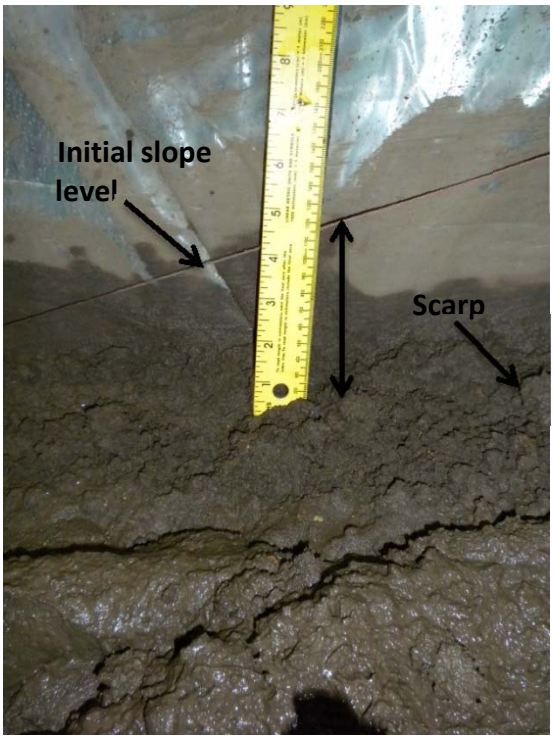

Figure 4.18 Point 3 in Figure 4.14. SL2

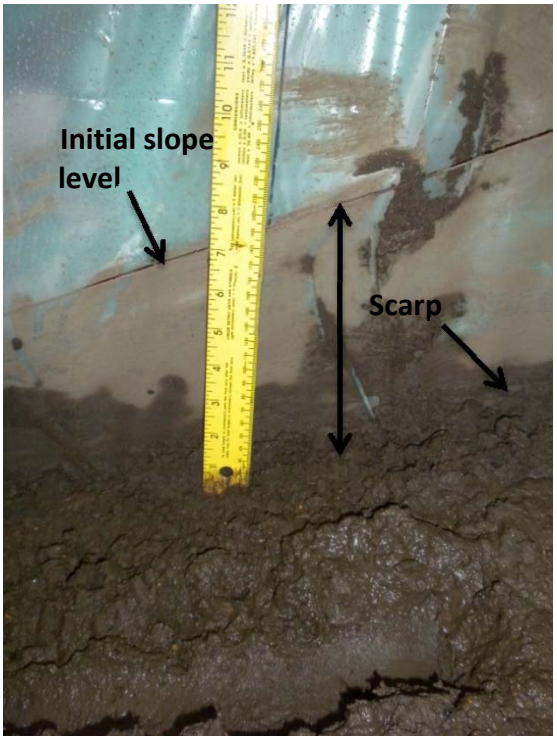

Figure 4.19 Point 4 in Figure 4.14.

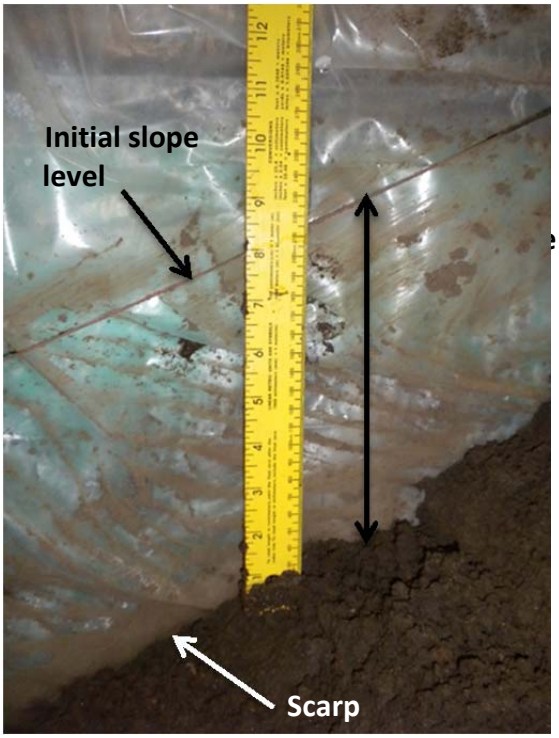

Figure 4.20 Point 5 in Figure 4.14. SL2

Figure 4.21 Point 6 in Figure 4.14. SL2

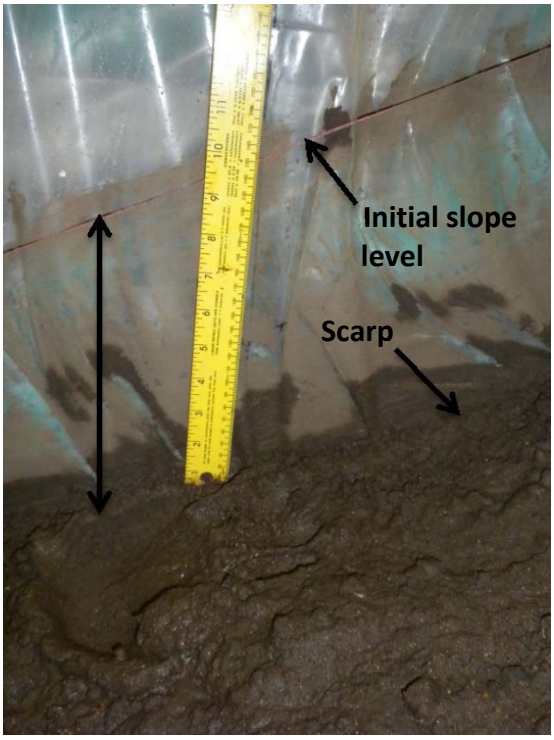

Figure 4.22 Point 7 in Figure 4.14. SL2

Figure 4.23 Point 8 in Figure 4.14. SL2

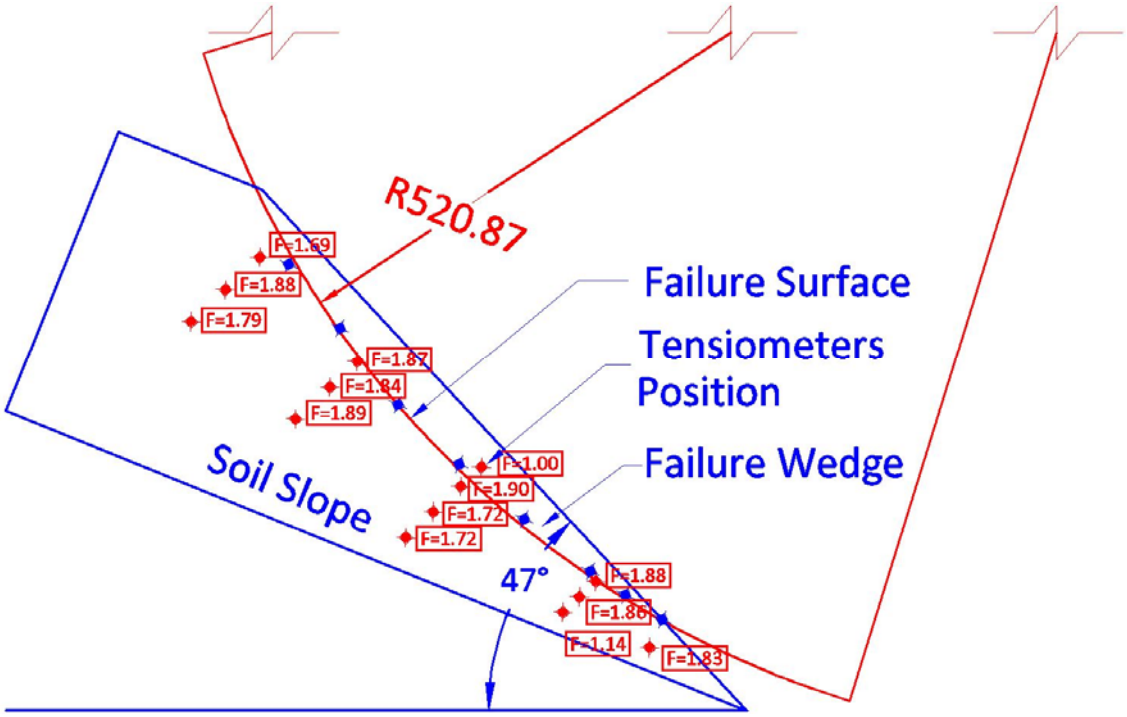

Figure 4.24 Calculation of factor of safety. See Appendix A for more detail on the calculation of factors of safety SL2.

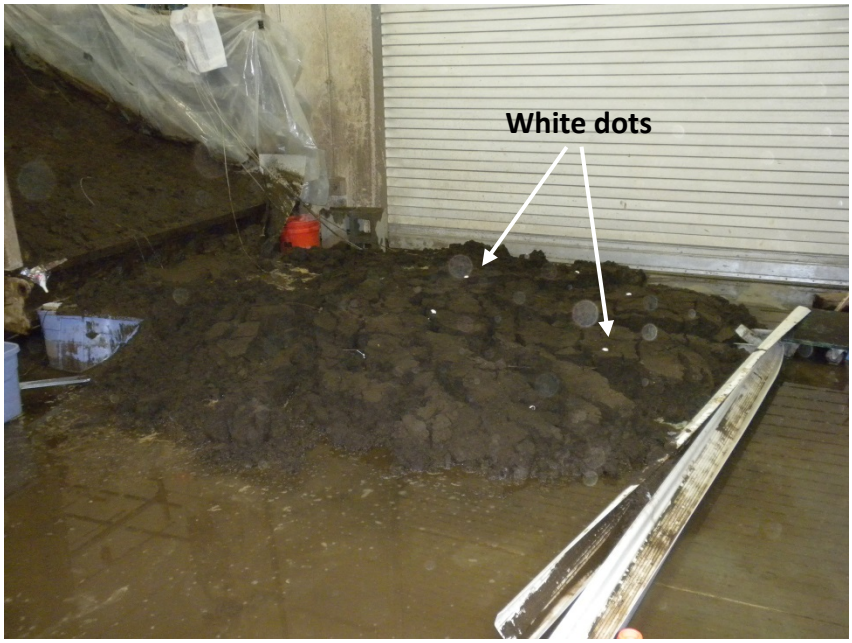

Figure 4.25 Second test slide. The white dots indicate the characteristics of the slide movement SL2.

Figure 4.14 shows the points measured after failure and a circular segment with a radius of 521 cm, which closely resembles the final failure shape of the slope. Only one tensiometer was located inside the failure wedge as expected; it was the only tensiometer which registered the failure. (F=1). The rest of the tensiometers, were out of the failure wedge and showed factors of safety greater than one. After this test, it was planned that; for the third and last test (SL3), all the tensiometers should be located shallower than deployed in the second test (SL2).

Figure 4.15 shows the image of the shape of the failure wedge of SL2 and Figure 4.25 shows the image of the same wedge of soil from SL2 that slid out of the dump bed container. After the wedge of soil slid out, the six white markers on the surface of the slope still remained aligned, indicating a fast and massive block of soil movement.

4.5.3 Model Slope SL3

After evaluating the results from SL2; which indicated a shallow failure surface, it was decided to study the pore water pressures in the failure wedge and proximities; therefore, all the tensiometer probes were placed 10 cm below the surface of the slope and 10cm apart from each other, in the arrangement shown in Figure 4.26.

The slope was built at a slope angle of 25°, the same slope angle of the previous tests, but the way the dump bed container was fed with the soil was changed. The soil was carried into the container by a Bobcat front end loader and compacted in layers of 20cms. After the slope was built; the instrumentation was installed. The slope angle was increased until 45°; close to the angle of failure of SL2 (47°), and then rained on for cycles of 13 minutes on followed by 10 minutes off. Cracks and pre-consolidation were observed to be similar to slopes SL1 and SL2. No failure occurred for the next month of cyclic precipitation; therefore, the slope angle was increased at the same rate of one degree per day until reaching an angle of 51°; the maximum angle of the dump bed container, and the rain schedule (13 min on and 10 minutes off) was continued, yet no failure was observed.

Two phenomenon could have contributed to this outcome; the first is the possible overcompaction of the bottom of the slope; caused by the change in the compaction procedure. The heavy weight of the bucket full of soil and the motor of the Bobcat loader caused the front wheels to apply a higher stress on the soil at the toe of the slope. This overcompacted zone likely included the tip of the failure wedge. The

second phenomenon is the seepage forces. As explained previously, seepage forces play an important role in the stability of slopes. Seepage forces cause consolidation, which reduces the void ratio and increases the density of the soil providing additional shear strength. Figure 4.27 shows the distribution of the lowest calculated factors of safety across the slope. These factors of safety were calculated with the procedure explained in Appendix A. It can be noted that no location shows a factor of safety equal to or less than one (FS>1). All the factors of safety were greater than one and the slope never failed, which is in agreement with the calculated FS>1.

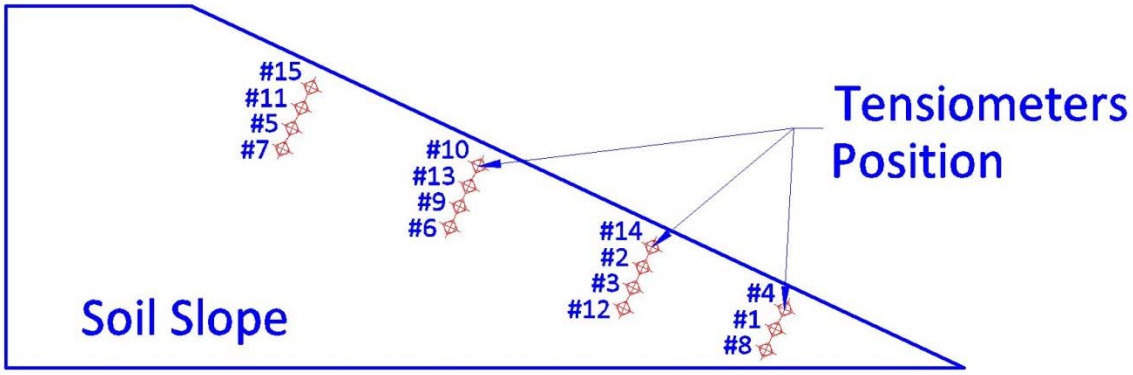

Figure 4.26 Arrangements of tensiometers into the slope for SL3.

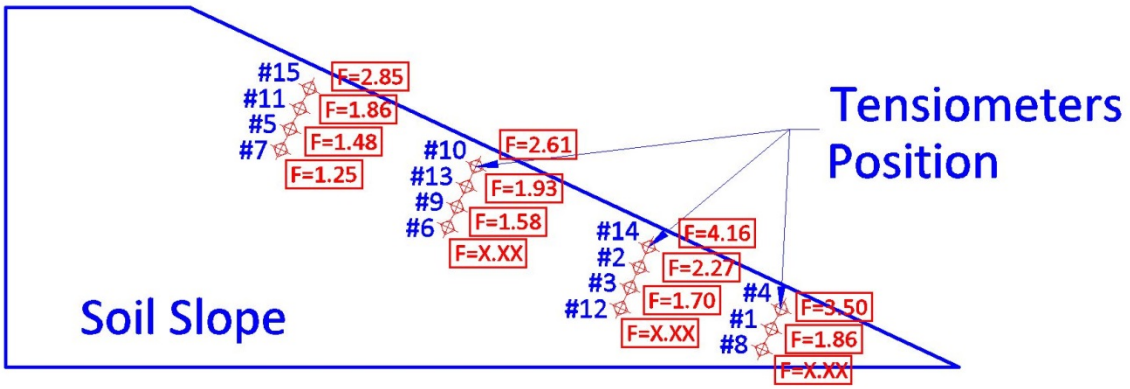

Figure 4.27 Distribution of Factor of Safety across the slope for SL3.

4.6 Summary

Three slope failure tests were performed. The tests consisted of filling the bed of a dump truck with a silty sand soil; in a sloping shape. The slopes were subjected to different amounts of precipitation and inclined at different angles until failure. In each test, pore pressures, deformations, slope angle, precipitaion were collected using different types of dedicated instruments. The data collected were analyzed using theories of soil mechanics, slope stability, soil hydraulics and unsaturated soil mechanics. The analysis is presented in the following chapter.

CHAPTER 5 ANALYSIS OF RESULTS

5.1 Introduction

In this chapter, a comparison of the results of the three tested slope models is presented. Comparisons include depth of the failure surface, the energy released by the mass of soil at failure, the shape, speed and volume of the failure mass and the time of failure. Some of these characteristics were analyzed by looking at videos recordings of the slope failures.

5.2 Failure Behaviors

The first slope model failed under saturated conditions and the second model failed under unsaturated conditions. However the third slope model tested did not fail.

The first two tests, SL1 and SL2, failed at inclination angles of 30 and 47 degrees respectively. The third test SL3 did not fail, even when the slope angle reached a maximum of 51 degrees of inclination and being subjected to the same amount of precipitation as SL2. The non-failure of SL3 is attributed to the change in the method of feeding and compacting the soil for SL3. In this method, the Bobcat loader was driven into the dump bed container while loaded with soil. As the placement process continued, the front tires of the Bobcat; rolled on top of the soil previously placed, providing additional compaction to the soil. The soil placement process repeated itself

in every layer until 50 cm and could have reached the toe of the potential failure wedge. It is observed that the highest factors of safety are located in the usual location where the slope failure starts. When additional compaction is provided, the size of the pores are reduced and the capillary forces increase, augmenting the matric suction; therefore, increasing the strength of the slope. (Lu and Likos, 2004).

Figures 5.2 to 5.7 give an idea of the speed and energy released during the slope tests. Figure 5.2 and Figure 5.3 correspond to the initial and final stage of SL1, the saturated test. Figures 5.4 to 5.7 correspond to the initial and final stages of failure of SL2, the unsaturated test. In test SL2, a small crack on top of the slope can be observed. Later, the crack expands until a total and sudden failure. It took only 10 seconds for complete failure.

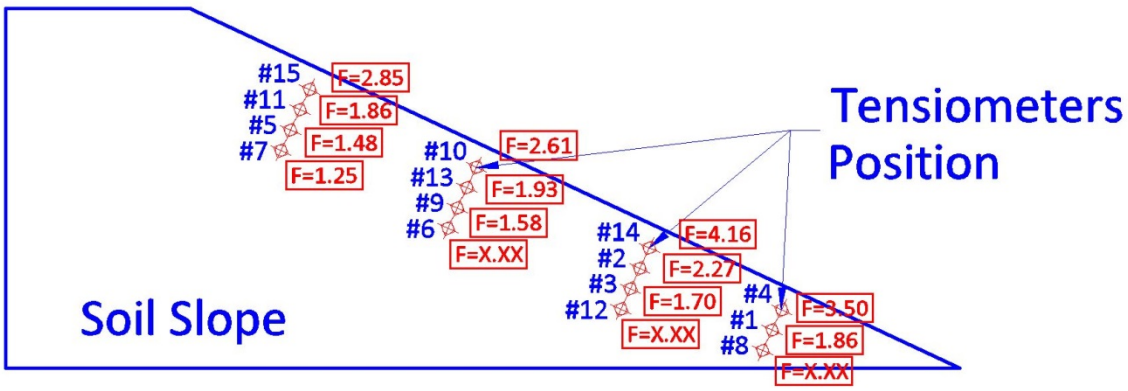

Figure 5.1 Calculation of factors of safety for SL3.

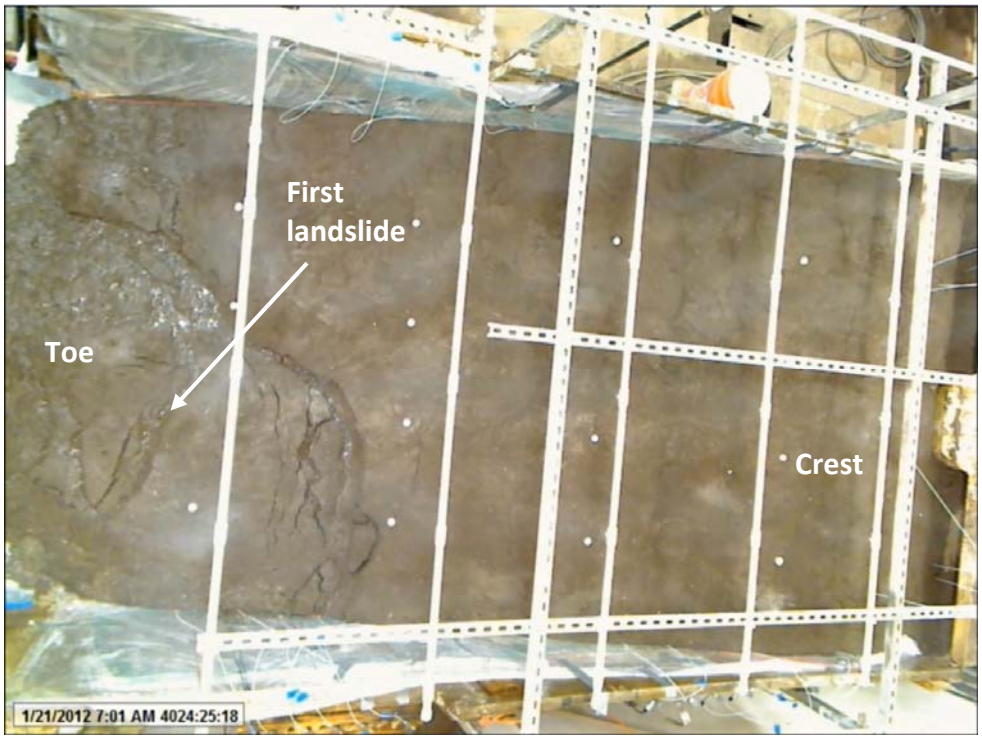

Figure 5.2 Initial stage of slope failure, SL1 on January 20th after 1 day 14 hours and 24 minutes of precipitation.

Figure 5.3 Final stage of failure, SL1 on January 23rd after 4 days 19 hours and 16 minutes of continuous precipitation

Figure 5.4 First stage of unsaturated failure, SL2.

Figure 5.5 Second stage of unsaturated failure, SL2.

Figure 5.6 Third stage of unsaturated failure, SL2.

Figure 5.7 Fourth and last stage of unsaturated failure, SL2.

5.3 Comparison of Failure Characteristics

The slope failures were characterized using the following factors: depth of failure surface, shape of failure wedge, volume of mobilized soil, time until total failure, velocity of moving soil and the energy of the sliding soil. Each characteristic is discussed below and summarized in Table 5.1.

***Depth of the failure wedge*:** Figures 5.8 and 5.9 allow comparison of the depth of the failure surface for the saturated and unsaturated tests. It can be observed that the depth of the saturated slope failure (SL1) was a considerably larger than the unsaturated one (SL2).

***Shape of the Failure Wedge*:** The unsaturated failure SL2 (Figure 5.9) shows an almost circular failure (See also Figure 4.24) unlike the saturated failure SL1 which shows a shapeless and disordered failure surface (Figure 5.8).

***Volume*:** It can be noted that the volume of the failure wedge is considerably larger in the saturated test (SL1, Figure 5.8) than the unsaturated test (SL2, Figure 5.9). It should also be noted from SL1 that the size of the scarp for SL1 is considerably larger than that of the scarp of SL2.

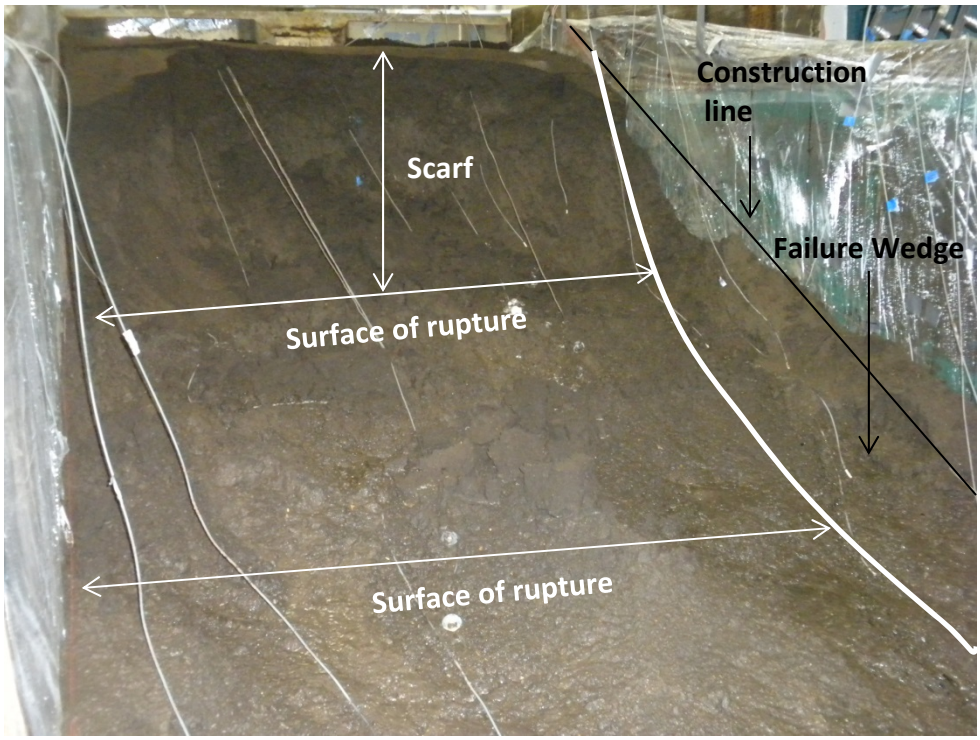

Figure 5.8 Saturated failure wedge SL1.

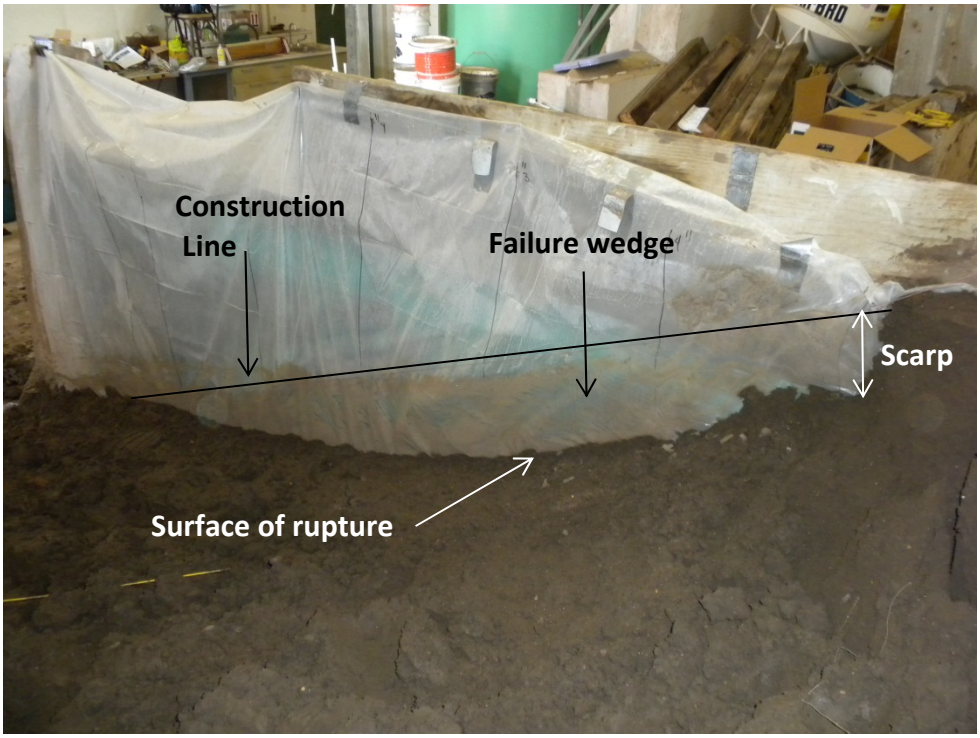

Figure 5.9 Unsaturated failure wedge SL2.

***Time until Total Failure*:** Time until total failure is defined as the time that takes for the total collapse of the slope. The time is measured from the video recordings of the slopes while they were being inclined and wetted with precipitation. It was found that the saturated test, SL1, took an estimated time of 4 days 19 hours and 16 minutes to reach complete failure. The unsaturated test, SL2, took only 10 seconds to reach total failure. Slope SL3 did not fail.

Speed: The speed of the slope failure was also measured from the video recordings. In order to do this, the distance among the "door knobs" installed on the surface was measured. It can be easily inferred, from the time to total failure, that the unsaturated slope (SL2) speed will be considerably larger than the speed for the saturated slope (SL1). If the distance and the time are known, then the speed can be calculated. The speed of the failure wedge for the saturated slope (SL1) was 0.85 m/d. While the speed of the failure wedge for the unsaturated slope (SL2) was 2.33×10^6 m/d or 60 mph.

***Energy*:** The energy corresponds to the total amount of energy. It includes kinetic energy and potential energy and is described by

$$\boldsymbol{E = \frac{1}{2}mv^2 + mgh} \qquad \textbf{Equation 32}$$

No energy calculations were made since the mass of the wedge for the saturated failure (SL1) is difficult to estimate; however, it can be easily inferred that; the energy of the unsaturated failure (SL2), is considerable larger than the energy of the saturated

slope, which had a speed of about 1 m/day, while the speed of the unsaturated slope failure was about 10^6 times faster. As shown in Equation 32, the potential energy (mgh) was similar for both slopes; however, the kinetic energy ($\frac{1}{2}mv^2$) would be $(10^6)^2$ or 10^{12} times higher for the unsaturated slope (SL2).

Table 5.1 Comparison of the saturated (SL1) and unsaturated slopes (SL2 and SL3) behaviors.

Characteristic Evaluated	Saturated (SL1)	Unsaturated (SL2)	Unsaturated (SL3)
Depth of failure surface	Deep	Shallow	No fail
Shape of failure surface	Shapeless	Circular	No fail
Volume of failed soil	Larger	Smaller	No fail
Time for complete fail	4 days, 19 hours, 16 min	10 seconds	No fail
Speed of slide mass (m/d)	0.85	$2.33x10^6$	No fail
Energy of slide mass	Small	Large 10^{12}	No fail
Angle of slope failure (°)	40	47	52 No fail
Precipitation Schedule	On	On 10min/Off 10min	On 13min/Off 10min
Precipitation rate	227.61lts/hr	113.80lts/hr	117.22lts/hr

CHAPTER 6 CONCLUSIONS AND RECOMMENDATIONS

6.1 Summary

Precipitation-induced landslides (slope failures) are common and can have severe economic and loss of life consequences. The objective of this research was to collect experimental data on soil model slopes under precipitation induced-slope failures. The data can provide a background for development of guidance for stability thresholds conditions for precipitation-induced slope failures

Three slopes were constructed using silty sand. Each slope was instrumented with deformation, pore water pressure, surface runoff and subsurface flow quantification equipment. A precipitation simulator system was used to rain on each slope as the slope angle was increased from an initial 25 degrees. Slope SL1 underwent a saturated failure. Slope SL2 underwent an unsaturated failure. Slope SL3 did not fail. Pore pressures measured at the time of failure were used to calculate factors of safety at points along the failure surface. The results for all the three slopes were analyzed.

6.2 Conclusions

The saturated slope (SL1) failed at a lower slope angle (β_f=40°) than either of the unsaturated slopes SL2, β_f=47° and SL3, β=52° no failure. The higher stable slope angles of the unsaturated slopes are attributed to the lower (and in some case) negative pore water pressures and associated higher effective stresses.

The failure of the saturated slope (SL1) began at the toe, where the soil liquefied as subsurface seepage saturated the toe of the slope. Subsequently, the failure slowly retrogressed up slope. The failure of the unsaturated slope (SL2) was rapid (within seconds). Slope SL2 was at a higher slope angle, β_f=47°, and it is likely that the low pore water pressures allowed the steeper angle, until the pore pressures increased sufficiently to permit the shear stress to become greater than the shear resistance of the soil.

It is concluded that unsaturated slopes can be stable at higher slope angles than saturated slopes; however, slope failure in the unsaturated case may be sudden and rapid. Rapid failures leave little time for warning anyone on or at the toe of a slope.

Monitoring changes in the pore water pressures; especially in unsaturated slopes can provide key insight into changing stability levels. A well-developed monitoring program may provide the basis for an early warning system for precipitation-induced landslides.

Measurements of the deformation were not possible due to the malfunctioning of the potentiometers caused by the high speeds of the slope failures.

6.3 Recommendations

Two model slope tests to failure do not provide sufficient information to make quantitative conclusions regarding precipitation induced slope failures. However, the findings do indicate that monitoring the pore-water pressures; especially in unsaturated slopes, may be the basis for an early warning system for precipitation-induced landslides. It is recommended that additional model tests be performed with all slopes at the same angle but with varied precipitation schedules and that the pore water pressures; especially nearer the surface be carefully monitored.

One of the most time demanding activities of these test is the placement and compaction of the soil into the container (dump truck bed). The third slope SL3 did not perform as expected. The author was looking for an expedited way to fill the dump bed container by filling the container directly with the Bobcat loader; however this likely led to an overcompaction of the toe of the slope in the dump bed. Using the overhead crane to place the soil in the dump bed, and adapting the Bobcat to pull the roller to compact the soil without driving the Bobcat itself into the dump bed container may still allow for accelerated construction of the slopes.

Every time a soil slope was built, technicians walked directly on the soil. The weight of a person divided by the area of one's foot can create a considerable amount of stress on the soil (300 to 400 psf) which might result in significant compaction. It is recommended to use boards to distribute the loads thereby reducing the compaction by foot traffic on the slopes.

Another time demanding activity was the placement of the instrumentation. The author suggests installing the instruments from the sides of the dump bed container, after the soil slope has been built; which means that it will be necessary to drill holes through the sides of the dump bed container in order to insert the tubes and ceramic tips of the tensiometers. This will result in permanent location of the ceramic tips in the soil slope, but it will reduce the time to build the soil slope, install the instruments and will improve the quality of the data, as it will not be necessary to dig and/or to walk on top of the slope to install the tensiometer tips. The proposed procedure will also allow more room for the installation of the extensometers anchors.

REFERENCES

Boeckman A. (2006) *"Load Transfer in Micropiles for Slope Stabilization From Tests of Large-Scale Physical Models"* M.S. Thesis University of Missouri-Columbia. 274 pgs

Deeken J.J. (2005*) "Large Scale Laboratory Testing of Model Slopes with Slender Reinforcement"* M.S. Thesis University of Missouri-Columbia. 106 Pages

Duncan, M. and Wright S. (2004). "Mechanics of limit Equilibrium Procedures" *Soil Strength and Slope Stability John Wiley and Sons New York, NY.* 577 Pages.

Fredlung and Rajardo (1996) *" Soil Mechanic for Unsaturated Soils"* John Wiley and Sons. New York NY. 544 Pages

Guiney, J.L. and Lawrence M.B. 1999 *"Preliminary Report: Hurricane Mitch"* NOAA http://www.nhc.noaa.gov/1998mitch.html (January 28th, 1999).

Lott. N and McCown S. "*Mitch: The Deadliest Hurricane Since 1780" NCDC, NOAA http://www.ncdc.noaa.gov/oa/reports/mitch/mitch.html* (January 23rd, 1999)

Lu and Godt (2010) *"Hillslope Hydrology and Stability "* USGS-Colorado School of Mines. http://pubs.usgs.gov/of/2001/ofr-01-0276/ (January, 2010)

Lu and Likos W. (2004). *"Unsaturated Soils Mechanics"* John Wiley and Sons. New York NY. 584 Pages

Mitchell M. and Soga K. (2005) *"Conduction Phenomena" Fundamentals of Soil Behavior."* John Wiley and Sons. New York NY. 577 Pages

Soilmoisture (2009) *"Operating Instructions for Soil Moisture Probe 2100F."* Soil Moisture Equipment Corp. 2009

Terzaghi K. and Peck R. (1967) "Soil Mechanics in Engineering Practice" John Wiley and Sons. New York NY. 566 Pages

University of Cornell 2011. "Vertical Infiltration Model" http://www.hydrology.bee.cornell.edu/BEE3710Handouts/GreenAmpt.pdf

USGS 2010 Landslide Team *"Hurricane Mitch, Central America"* USGS, NOAA http://landslides.usgs.gov/research/other/hurricanemitch/

World Food Program 2012 "*Honduras"* WFP
http://www.wfp.org/countries/honduras/overview

APPENDIX A

Potentiometer calibration

The deadman anchor moves as the soil in the model slope moves, resulting in the rotary potentiometer sending a signal, in the form of voltage, to a computer where it is recorded. A calibration is required to transform the voltages into units of displacement. A calibration curve was developed for each potentiometer by moving the deadman anchor known distances; i.e., every centimeter. The voltages were plotted versus the known movements (Figure A-1). The resulting calibration curves were then used to transform voltages into displacements. Each potentiometer was calibrated generating a total of nine graphs.

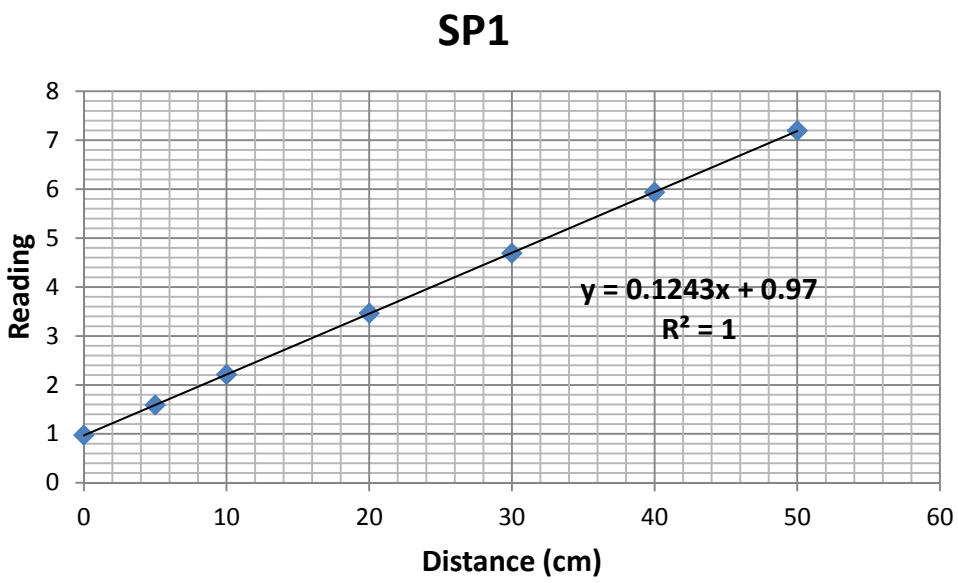

A-1. Calibration graph of potentiometer SP1.

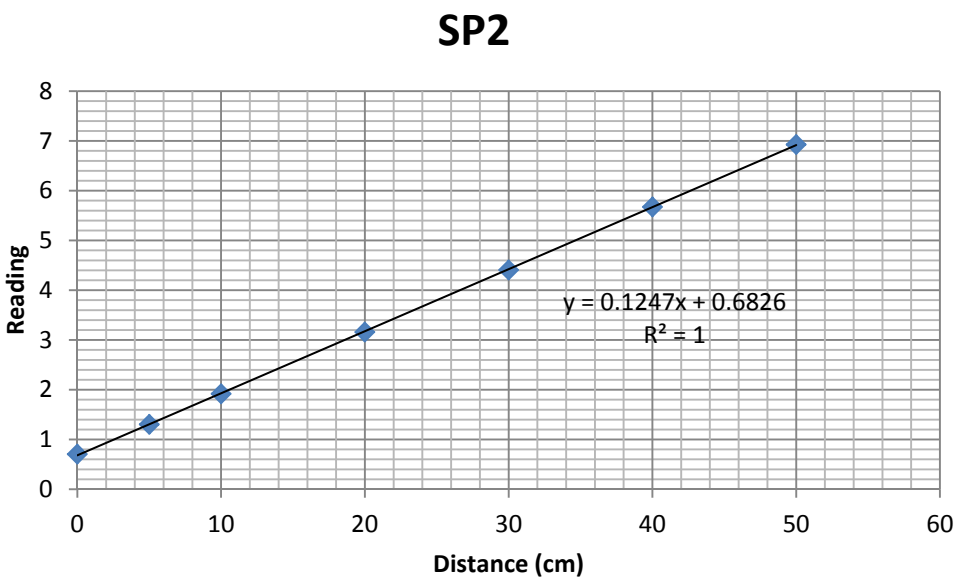

A-2. Calibration graph of potentiometer SP2.

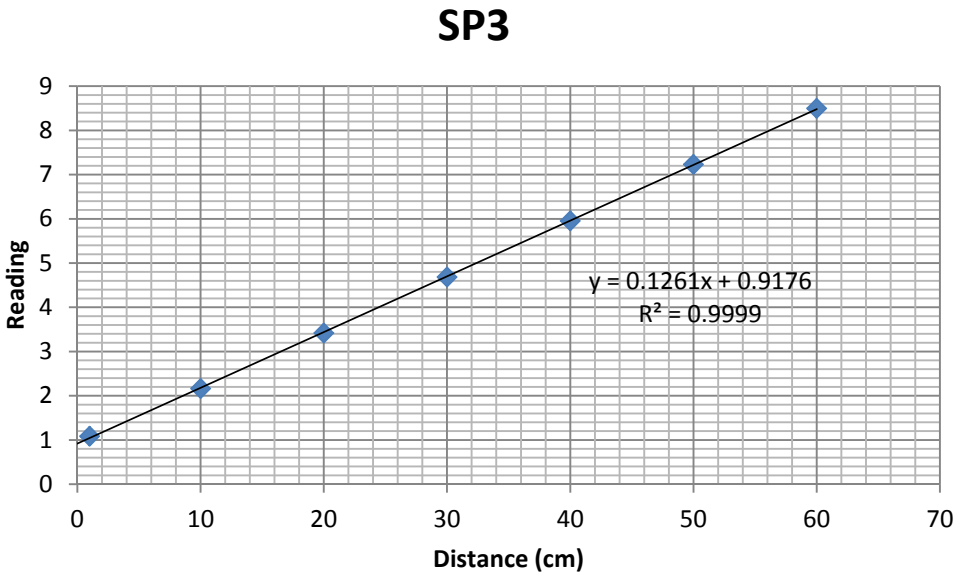

A-3. Calibration graph of potentiometer SP3.

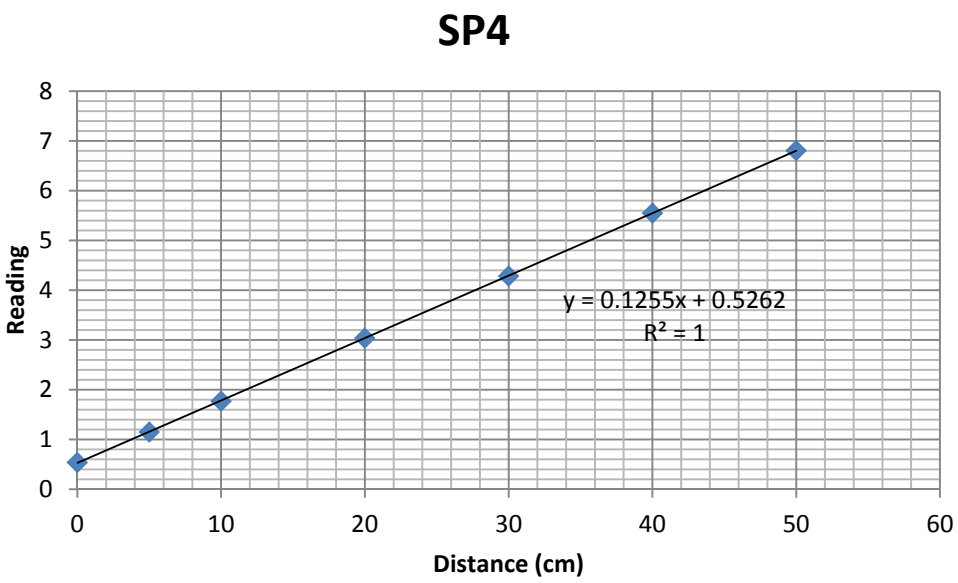

A-4. Calibration graph of potentiometer SP4.

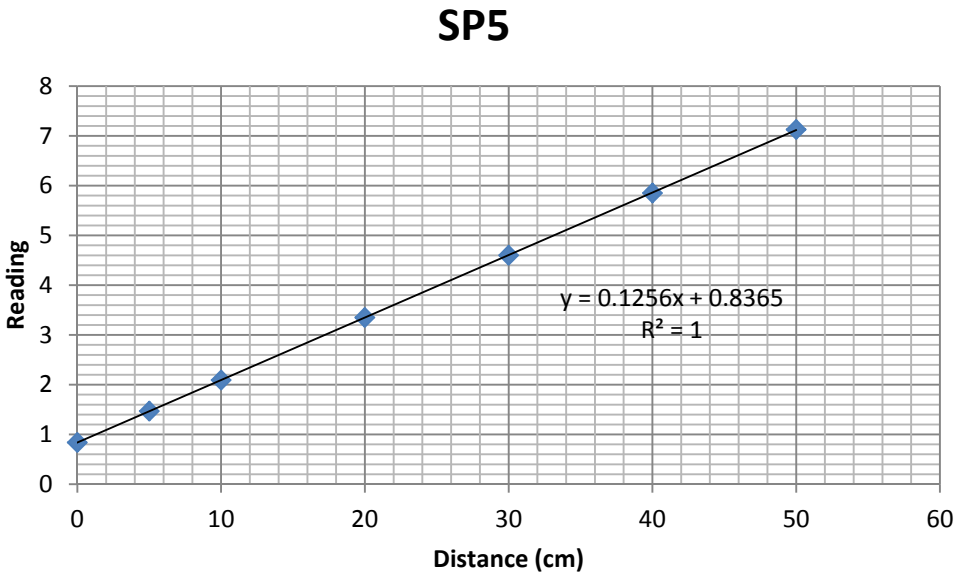

A-5. Calibration graph of potentiometer SP5.

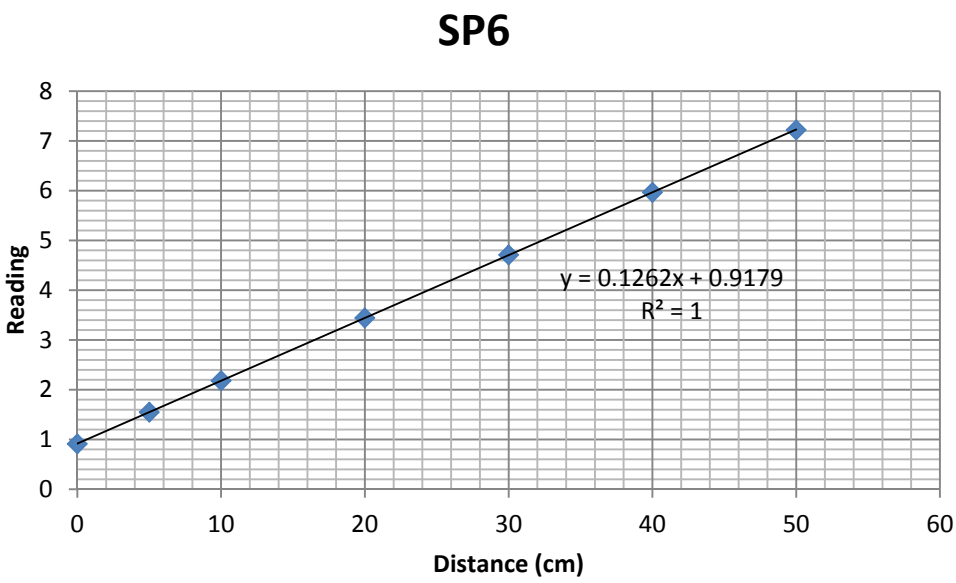

A-6. Calibration graph of potentiometer SP6.

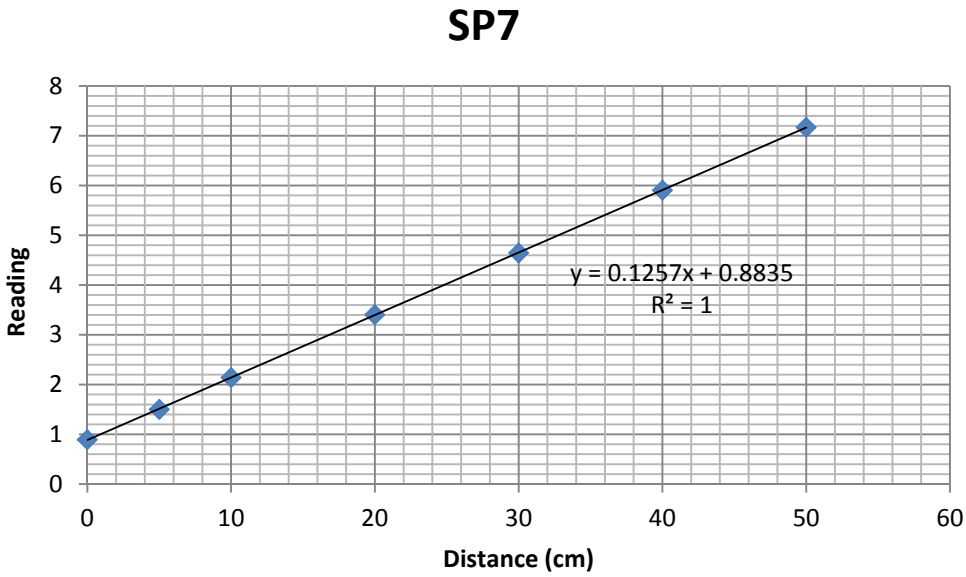

A-7. Calibration graph of potentiometer SP7.

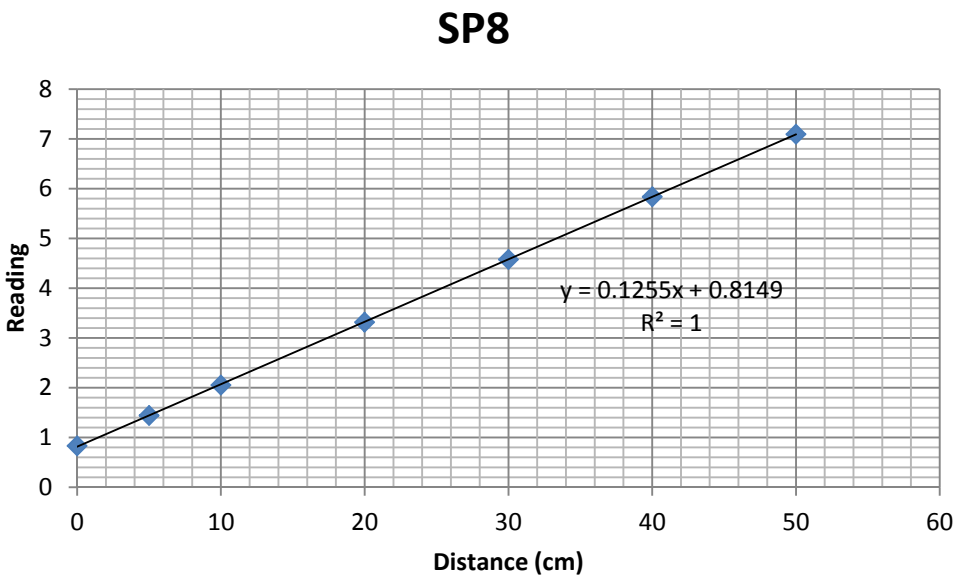

A-8. Calibration graph of potentiometer SP8.

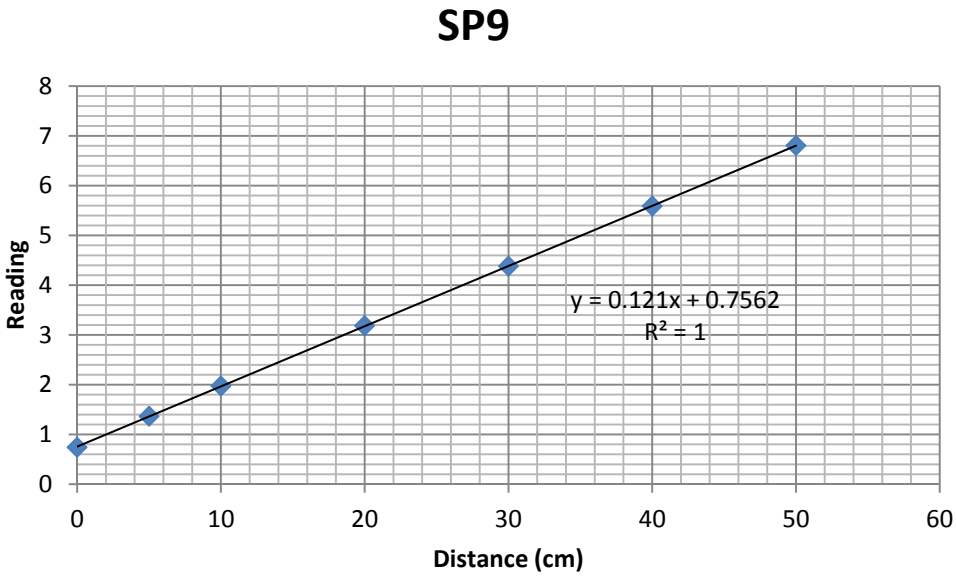

A-9. Calibration graph of potentiometer SP9.

APPENDIX B

Measuring the negative pore pressure in the soil pore water

Tensiometers were used to measure the soil suction (negative pore water pressures) in the soil. A tensiometer measures the negative pore-water pressure in a soil. The tensiometer consists of a high air entry, porous ceramic cup connected to a pressure measuring device through a small bore tube. The tube was plastic due to its low heat conduction and noncorrosive nature. The tube and the cup were filled with de-aired, and deionized water. The cup was inserted into a pre-cored hole and then refilled with soil. Once pressure equilibrium is achieved between the soil and the measuring system, the water in the tensiometer will have the same pressure as the pore water in the soil. The measured negative pore-water pressure is numerically equal to the matric suction when the pore-air pressure is atmospheric. The measured matric suction must not exceed the air entry value of the ceramic cup. (1 Bar), otherwise the probe will be de-watered and no more valid pressure (suction) readings can be recorded. The osmotic component of soil suction is not measured with tensiometers since soluble salts are free to move through the porous cup. (Fredlung and Rajardo, 1993)

Soilmoisture® Tensiometer probe

Fifteen tensiometers from Soilmoisture® were installed in each model slope. The tensiometers were equipped with pressure transducers, which transmitted the suction readings; from the ceramic tip, installed into the soil, through the tubing, to the acrylic cup, to the pressure transducer and finally to the computer, where they were recorded at a rate of three readings per minute. Figure B-1 shows a picture of the set up used to obtain the pore water pressure reading and Figure B-2 shows the tensiometer parts and the tools used to calibrate it. Note that the vacuum dial gage was replaced with the pore pressure transducer and instead of the screw top bottle, a 20oz syringe was used to flush the air bubbles from the tubing system.

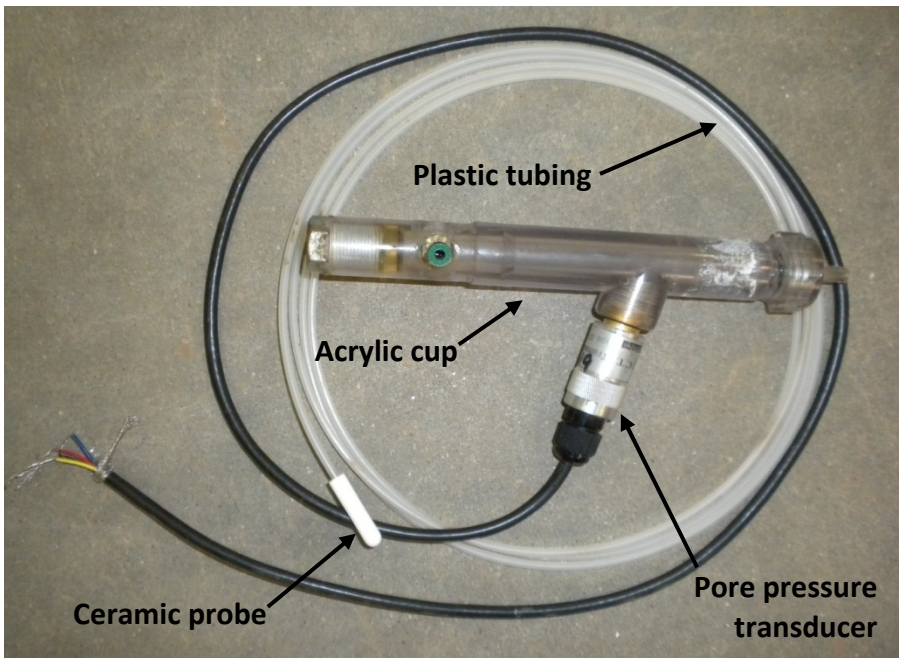

B-1 Tensiometer showing porous ceramic tip, plastic tubing, acrylic cup (water reservoir) and pore pressure transducer.

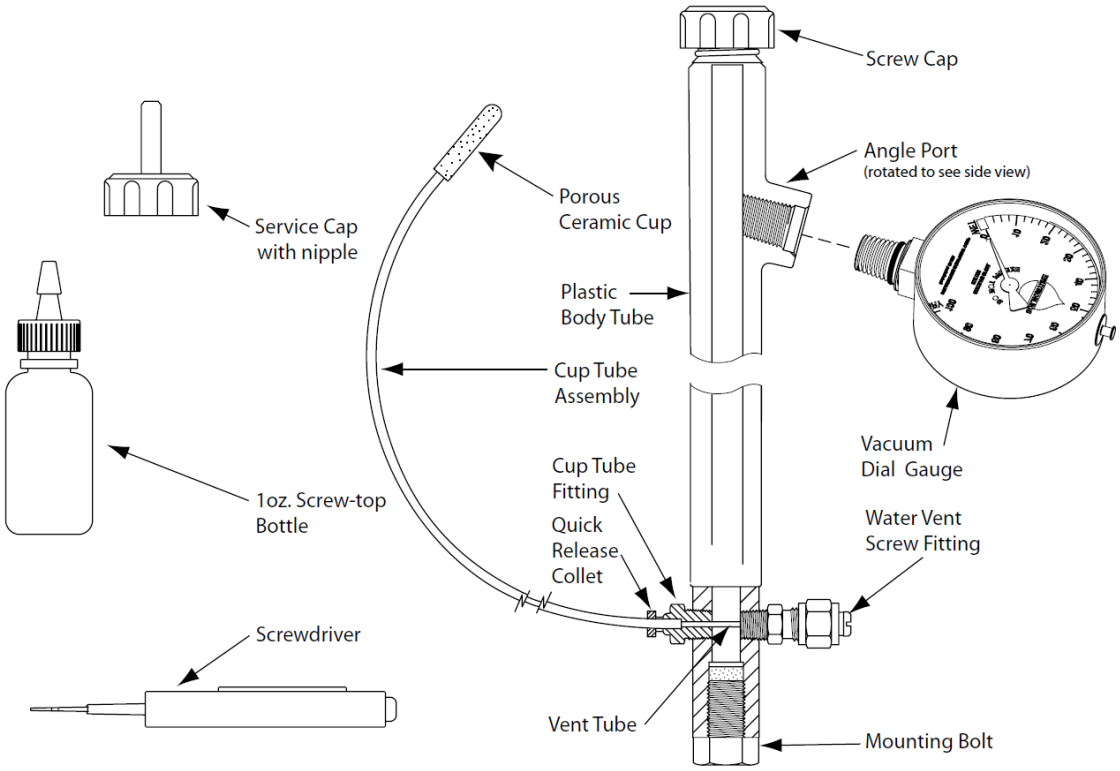

B-2 Kit of a tensiometer. A pore pressure transducer was used in place of the vacuum gage. (SoilMoisture® 2009)

Assembly of a tensiometer

It is a challenge to prepare each one of these devices; since they are composed of six different materials including acrylic, copper, plastic, ceramic, rubber, and steel; creating more than ten joints. The intent is to measure negative pore water pressure or soil suction; therefore, the proper assembly of each one of the parts of the tensiometer devices is crucial to avoid leaks. This assembly is divided in three important steps:

***Preparing the ceramic tip**:* The ceramic tip is a porous hollow ceramic probe that enters in contact with the soil, and transmits the flow of water through the tubing to the acrylic cup and finally to the pressure transducer. It measures externally 1.2" long by 0.250" diameter and has 1-Bar air entry pressure. Figure B-3 shows the ceramic tip and Figure B-4 shows a sketch of the tubing into it. The first step is to submerge the tip in deionized and-deaired water to saturate the pores of the ceramic tip with water. It is important that, at all times, this piece is manipulated with clean hands, free from grease, oils or any substances that might obstruct the pores of the ceramic. If possible it is recommended to use rubber gloves. This ceramic tip is designed to completely contain the vent or inner tube and the Nylon or outer tube inserted ¼" into the tip. These two tubes must have special preparation at their tips. The vent tube must be cut at a 45 degree angle at the tip, and the tip must be sandpapered in order to prevent pinching the Nylon tube. After the two tubes are prepared and inserted into the ceramic tip, both of them have to be generously bonded and sealed with the special bond included in the kit as shown in Figure B-4

B-3 Porous ceramic tip of tensiometer.

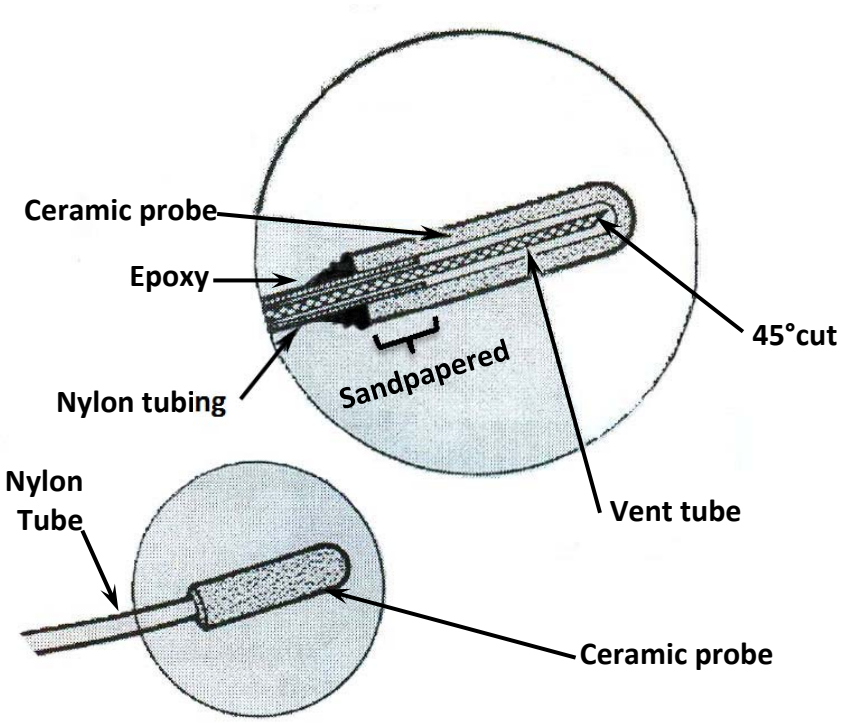

B-4 Cross section of porous ceramic tip of the tensiometer. (SoilMoisture®, 2009)

Preparing the tubing. The tubing for this device consists of two types of tubing; the vent tubing and the nylon tubing. The Nylon tubing cases the vent tubing and it goes from, ¼" inside the ceramic tip (as shown in Figure B-4), until the cup tube's fitting as shown in Figure B-5. The vent tubing extends from deep inside the ceramic tip (as shown in Figure B-4), crosses the acrylic cup and extends ¼" into the water vent nut. (Figure B-5). It is recommended to use at least a 2.0 meter (7 feet) length of tubing

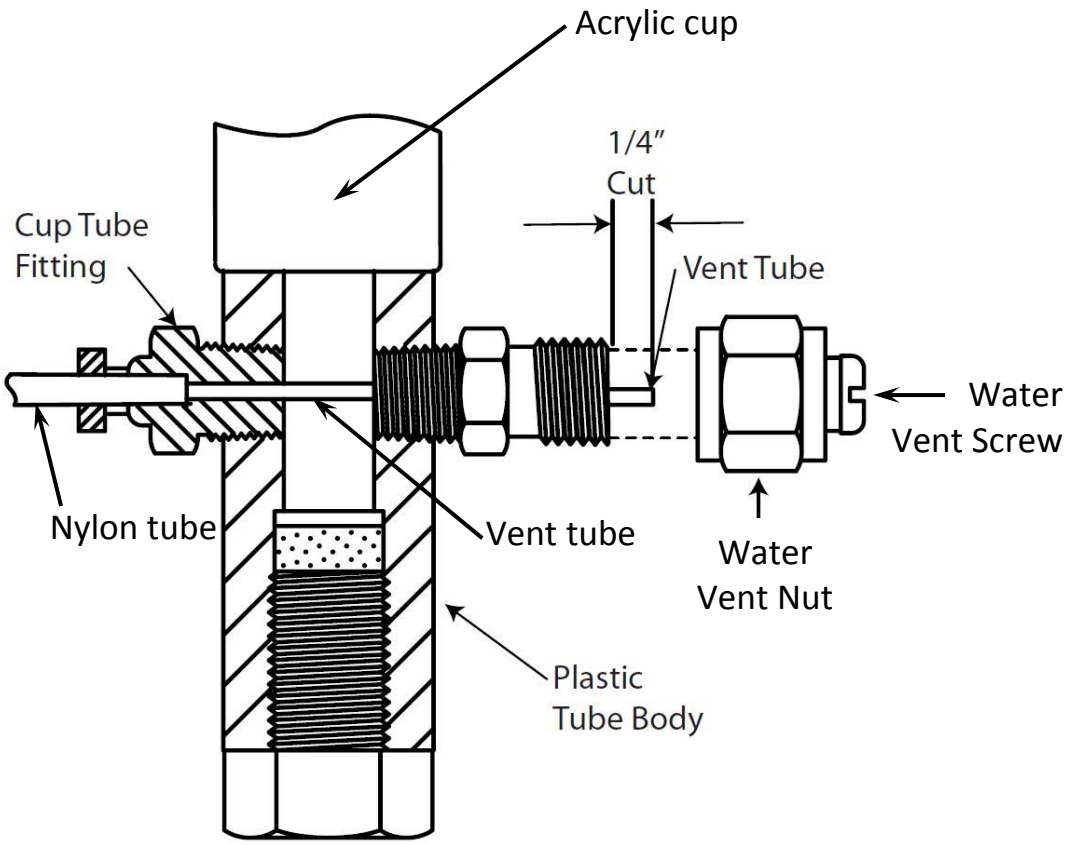

B-5 Location of tubes in the acrylic cup of tensiometer (Soilmoisture®, 2009)

Filling the cup. Once the ceramic tip is bonded to the tubing and the tubing connected to the acrylic cup, we can continue to fill the entire system with deionized, de-aired water. It is important to emphasize that, for these devices, only deionized, de-aired water should be used, in order to protect from organic content and to prevent cavitation in the tubing from the air of the water.

Figure B-6 shows the process of filling the tensiometer system. The first step is to fill the acrylic cup with water completely; with the Water Vent Screw Retaining Nut tightened (see Figure B-5), the Water Vent Screw is removed; in order to use it to expel

the air from the two tubes; then a water pump (or syringe) is used to force the water from the acrylic cup through the Nylon tubing, to the ceramic tip to the vent tube, until a steady flow of water squirts out from the vent tube in the Water Vent Nut. This process should be repeated, at least three times, depending on the length of the tubing. Once this system is saturated with water, the ceramic tips must be kept under water at all times until placed in the soil.

Failing to follow, any one of these procedures might result in a slow response in the functioning of the tensiometer which translates into poor quality readings of negative pore pressure.

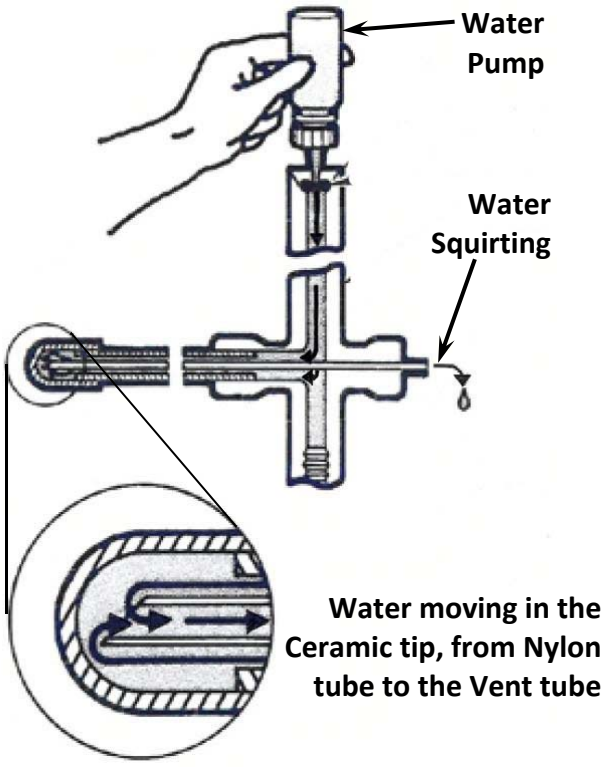

B-6 Process of filling the tensiometer system. (Soilmoisture, 2009)

Calibration of tensiometers

Although, the calibration of the tensiometers is similar to that of the potentiometers, the procedure is different. Instead of the vacuum vial gage shown in Figure B-2, a pore pressure transducer was used (Figure B-1). The pressure transducer was connected to the same computer as the potentiometer, and transforms the negative pore pressure from the soil into voltage units. Hence the challenge is to transform the voltage units into units of pressure.

The earth slopes fail at an unknown time; therefore it is crucial to take the correct readings of the pore pressure at the moment of failure. Accuracy and good time-response at failure from each pressure transducer is required for good quality data.

A wooden frame was built to evaluate the response and accuracy and, at the same time, to calibrate the pore pressure transducers. The frame consists of two 2-inch by 4-inch wooden poles connected beside the slope model container. The poles are marked in intervals of known distances; i.e., every twenty centimeters. The idea was to work with all fifteen pore pressure transducers at the same time, in order to compare the results among them. Figures B-7, B-8 and B-9 show the wooden frame.

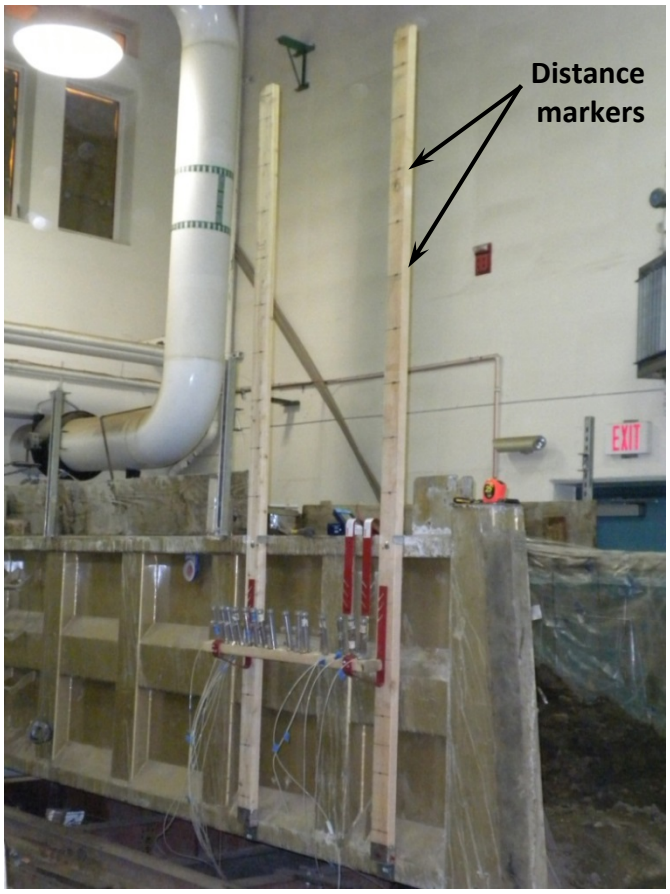

B-7 Wooden frame made to evaluate and calibrate the porewater pressure transducers.

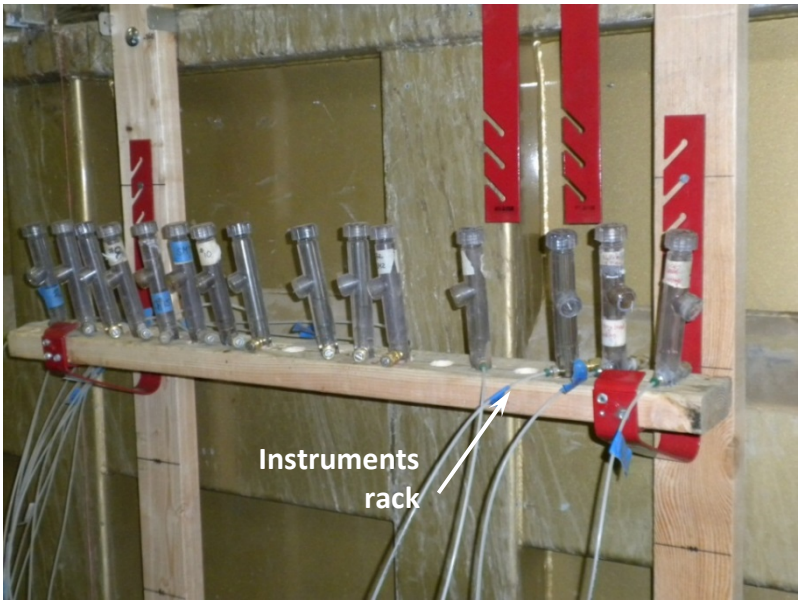

B-8 Rack to mount the tensiometers and pressure transducers.

B-9 Water reservoirs to maintain the porous ceramic tips under water.

The procedure is straightforward. Once the devices are assembled, they are put in the instrument rack as shown in Figure B-8. The reservoirs shown in Figure B-9 are filled with deionized, de-aired water to a known depth. Provisions should be taken so that the ceramic tips remain submerged under water in the reservoirs, at all times, as the racks move.

Now the evaluation can be started. It is important to mention that the position of the tip, relative to the transducer, indicates whether the transducer is in compression or tension. When the ceramic tip is below the transducer, tension or negative pressure is evaluated, and when the ceramic tip is above the transducer, compression or positive pressure is evaluated. It is indifferent how the evaluation is started; from compression to tension or from tension to compression.

In this example, we will start in tension. The rack in Figure B-8, with the tensiometers and transducers, is lifted; above the rack with the water reservoirs, until full extension of the tubes, in order to create and, to test at the same time, the maximum possible tension or negative pore pressure. The rack with the water reservoirs remains stationary in the meantime. Later on, the rack with the tensiometers and pressure transducers (Figure B-8) is moved, from its initial position downwards, and held at every known distance previously marked in the wooden poles (Figure B-7), in time intervals of one hour. This step is done until the rack with the tensiometers reaches the position of the rack with the water reservoirs and it can no longer move (Figure B-9).

Now we move to continue evaluating the compression or positive pressure of the transducers and tensiometers. Now the rack with the reservoirs of water is moved, vertically along the same marked path, and the rack with the tensiometers and transducers remains stationary. Figure B-10 shows a graph of an example of a good evaluation of the tensiometer and transducer response.

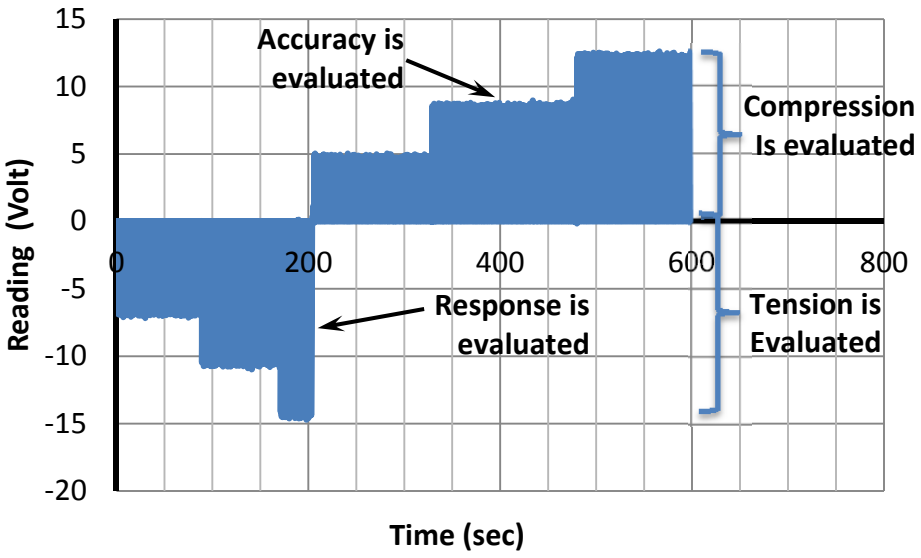

B-10 Graph of typical evaluation of tensiometer and transducer response.

Figure B-11 shows an example of the instruments being evaluated in compression. Note that the water reservoirs are above the transducers. To evaluate the tension, the rack with the instruments (pressure transducers) is above the rack with the water reservoirs.

The accuracy is evaluated over a one hour duration, when the transducer remains observing the same reading, even after, there has been a change in the potential. A low accuracy would be observed if the lines were not flat or horizontal as seen in Figures B-12 and B-13.

The response is evaluated when the transducer is capable of registering the sudden change in the potential, created when the racks are suddenly moved vertically. A low response would be observed if the lines were not straight, vertical or inclined. Figures B-12 shows pore pressure transducer PT8 and PT12 responding slowly

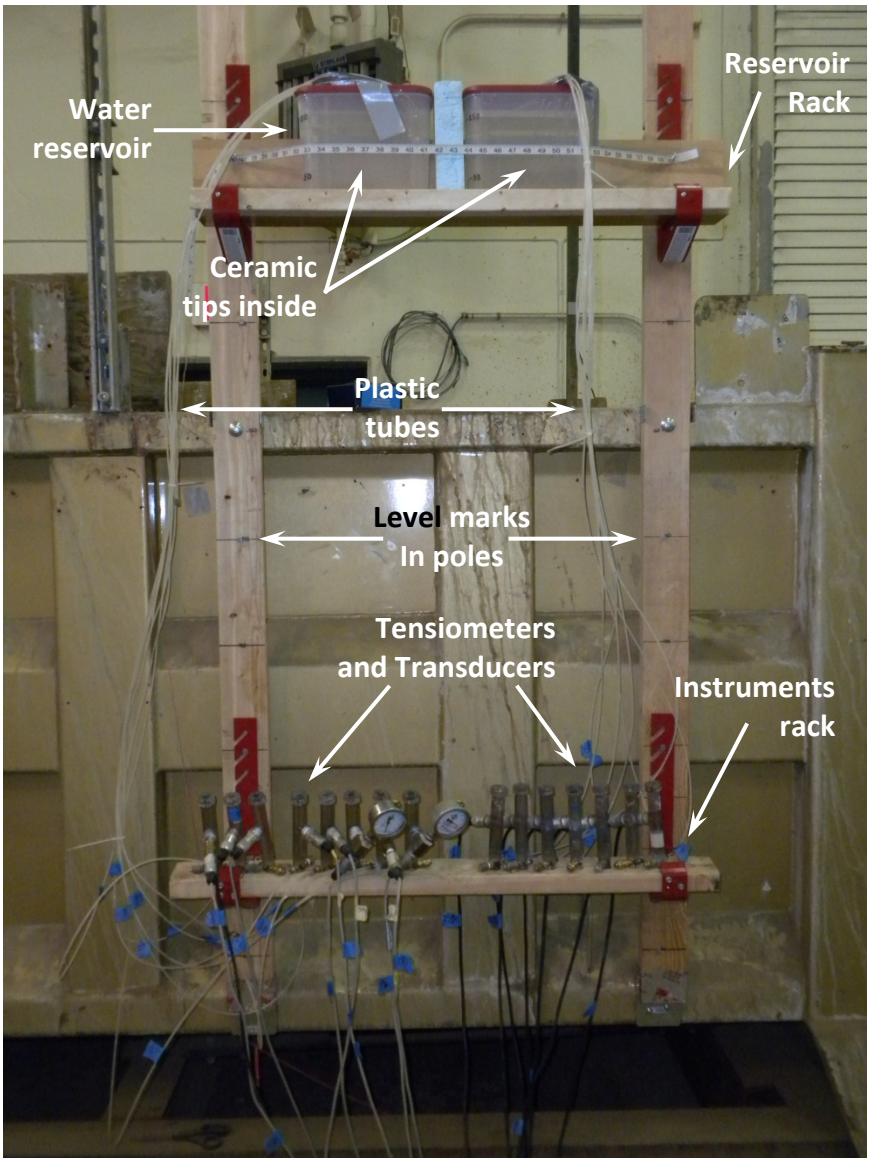

B-11 Graph of Calibration in Compression of Tensiometer and Transducers.

A leak in any of the joints of these tensiometers can cause inaccuracy and slow response in the devices which result in poor quality data. Note that by knowing the distance marked on the wooden poles we can convert the voltages to a height of an equivalent column of water and later to pressure units.

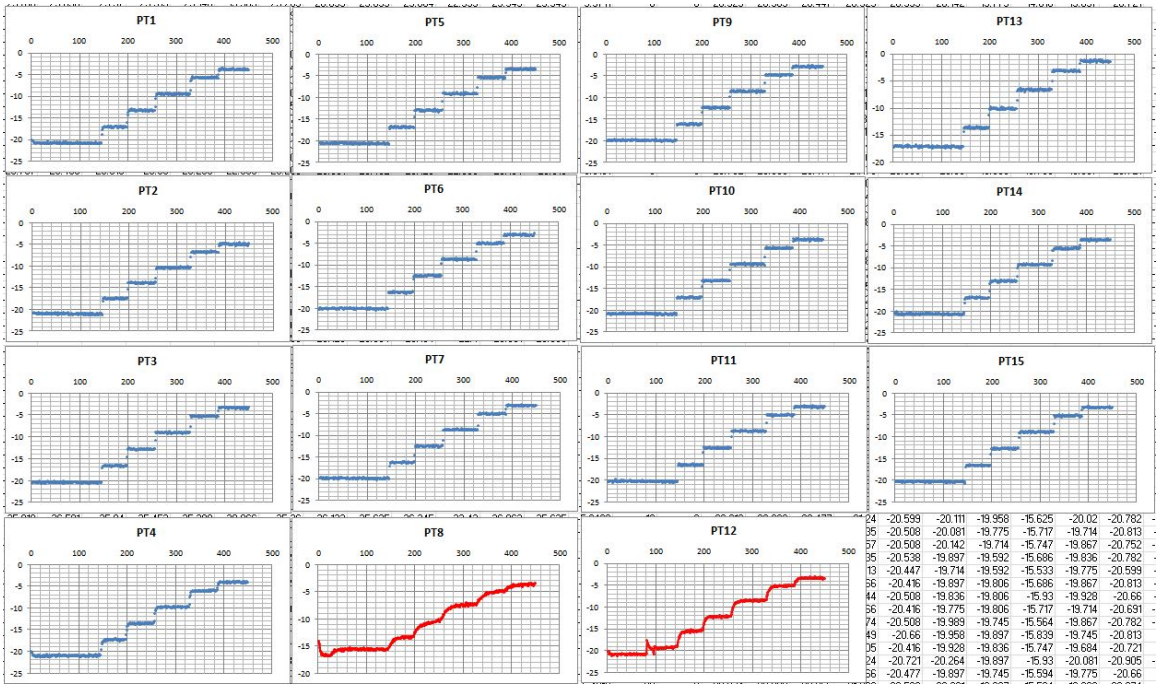

B-12 Graph of the results of simultaneous calibration of fifteen pore pressure transducers.

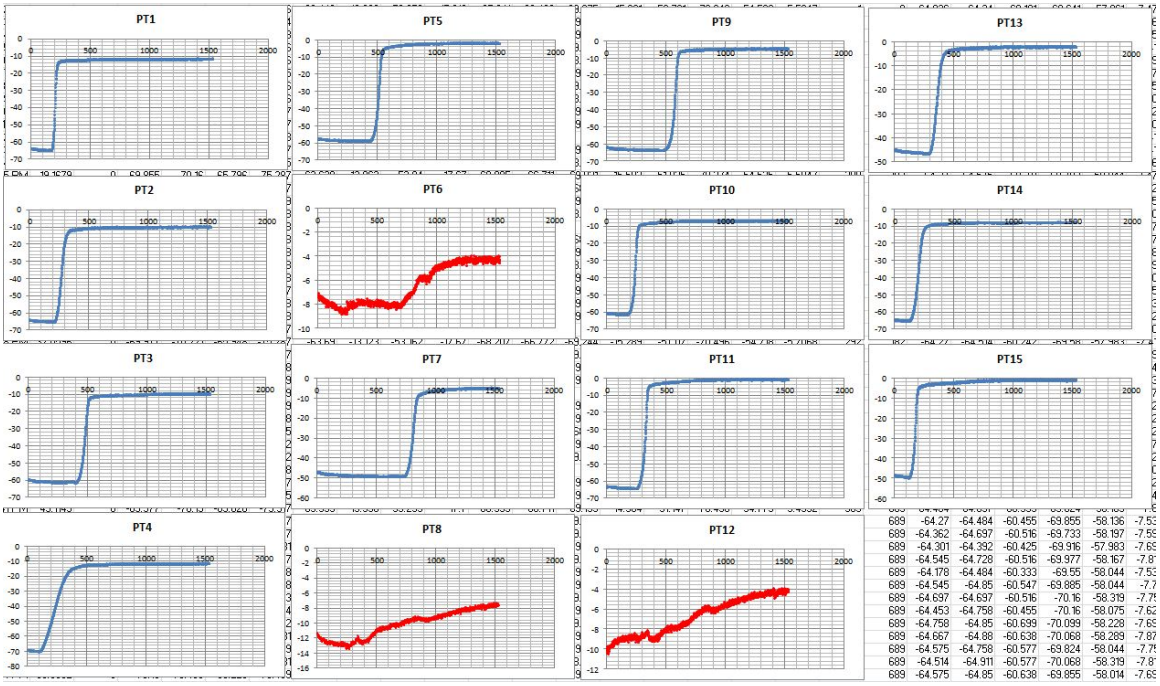

B-13 Graph of pore pressures readings for slope SL3.

Figure B-12 and B-13 show the importance of the proper evaluation of accuracy and response, by following the previously described procedure. Figure B-12 shows the graphs of the results of the simultaneous calibration of the fifteen instruments before performing test SL3. Figure B-13 shows the graphs of the results of the pore pressure from the same fifteen instruments, as the precipitation infiltrates into the soil slope after performing test SL3. In Figure B-12, it can be observed (in red), that it was known before performing the test that transducers PT8 and PT12 presented slow response times. This was confirmed after performing the test SL3 and it can be seen (in red) in Figure B-13. It is unknown why PT6 resulted in flawed results.

APPENDIX C

Derivation of the relationship between θ and ω in the SWCC

Fredlund and Rajardo 1993 presented the relationship between the gravimetric (ω) and volumetric moisture content (θ) as:

$$\boldsymbol{\theta = \frac{\omega G S}{S + \omega G}} \qquad \textbf{Equation 33}$$

Where G_s is the specific gravity of solids, *S* is the degree of saturation, ω is the gravimetric moisture content (mass of water divided by the mass of dry soil), θ is the volumetric water content (volume of water divided by total volume of specimen), which can also be expressed as a function of saturation and porosity as follows:

$$\boldsymbol{\theta = Sn \ \ or \ S = \theta / n} \qquad \textbf{Equation 34}$$

Substituting equation 34 in Equation 33 we obtain:

$$\boldsymbol{\theta = \frac{\frac{\omega G \theta}{n}}{\frac{\theta}{n} + \omega G}}$$

Canceling the term θ and rearranging Equation 33 we obtain the next expression:

$$\boldsymbol{\frac{\theta}{n} + \omega G = \frac{\omega G}{n}}$$

$$\boldsymbol{\theta = \omega G - \omega G n}$$

$$\boldsymbol{\theta = \omega G(1 - n)} \qquad \textbf{Equation 35}$$

Equation 35 relates the gravimetric moisture content (ω) to the volumetric moisture content (θ). The gravimetric water content ω is desired. The challenge is to obtain the porosity *n* or void ratio *e*. However since gravimetric moisture contents have been measured; and by using other parameters of the soil, we can obtain this value as follows:

$$n = \frac{V_v}{V_t}$$ **Equation 36**

$$V_t = V_s + V_v \quad or \quad V_v = V_t - V_s$$ **Equation 37**

$$V_s = \frac{W_s}{G_s \gamma_w}$$ **Equation 38**

$$V_t = \frac{W_s}{\gamma_d}.$$ **Equation 39**

W_s is the weight of dry soil; G_s is the specific gravity of the solids, 2.64 for this soil; γ_d is the dry unit weight, 120pcf (Boeckman, 2005); Υ_w is the unit weight of the water, 1 g/cm^3.

APPENDIX D

Calculations of factor of safety

Figure D-1 contains an Excel® format example table of the results of calculations developed to compute the factor of safety, in this case for pore pressure transducer PT1. The values in Columns A, B, C, D, E, F and U represent the original values obtained from importing the table from Lab View® to Excel®. Lab View® is the software used to record the data directly from the instrumentation. Column A is the date, columns B, C, and D, are the time at which the reading was recorded, Column E is the slope angle, Column F is the raw matric suction and column U is the values of base correction of the matric suction. The values in Column X are the matric suction in units of volts and are obtained from subtracting column F minus column U. The values of column Y are the matric suction in units of height of a column of water and are obtained by converting the units of volts to units of height, as explained in Appendix A. The values of columns Z, AA, AB, AC, and AD are the values of height correction as described in Section 3.4. Column AE is the corrected values of the matric suction obtained by subtracting the values of column Y minus the values in column AD as described in Section 3.4 and column AF is the absolute value of these calculations. Column AG is the conversion of the values from voltage units to kilopascal, kPa. Column AH is the values of the volumetric water content during the test, and obtained by using the fitted SWCC in Equation 2. The values of Column AI are obtained using Equation 35 and they are the

conversion from volumetric water content to gravimetric water content. Columns AJ, AK, AL and AM are the calculations for the unsaturated hydraulic conductivity as explained in Section 2.7. The values in columns AN, AO, AP, AQ, AR are results of the computations from the previous columns used to calculate the vertical infiltration rate in column AS using Equation 15 as explained in Section 2.8. The values in column AT correspond to the water pressure and they are obtained by multiplying the water density by the vertical height to the location of the ceramic tip. The values in the column AU correspond to the air pressure. Since we know the values of the water pressure and the matric suction is obtained from the readings of the tensiometers, we can obtain the values of the air pore pressure. These values are obtained from the matric suction equation. The values in column AV are the total stress and they are obtained from Equation 17 in Section 2.9. After we have done all of the calculations, we are ready to compute the factor of safety of the slope at this transducer. The factor of safety is calculated using Equation 1, which is transformed, using Equation 8 and Equation 17, from Sections 2.5. and 2.9 respectively, as follows:

$$\boldsymbol{F = \frac{S}{\tau} = \frac{c' + [(\sigma - U_a)_f + \chi_f (U_a - U_w)_f] \tan \phi'}{\gamma_d (1 + \omega) Z \cos \beta \sin \beta}} \qquad \textbf{Equation 40}$$

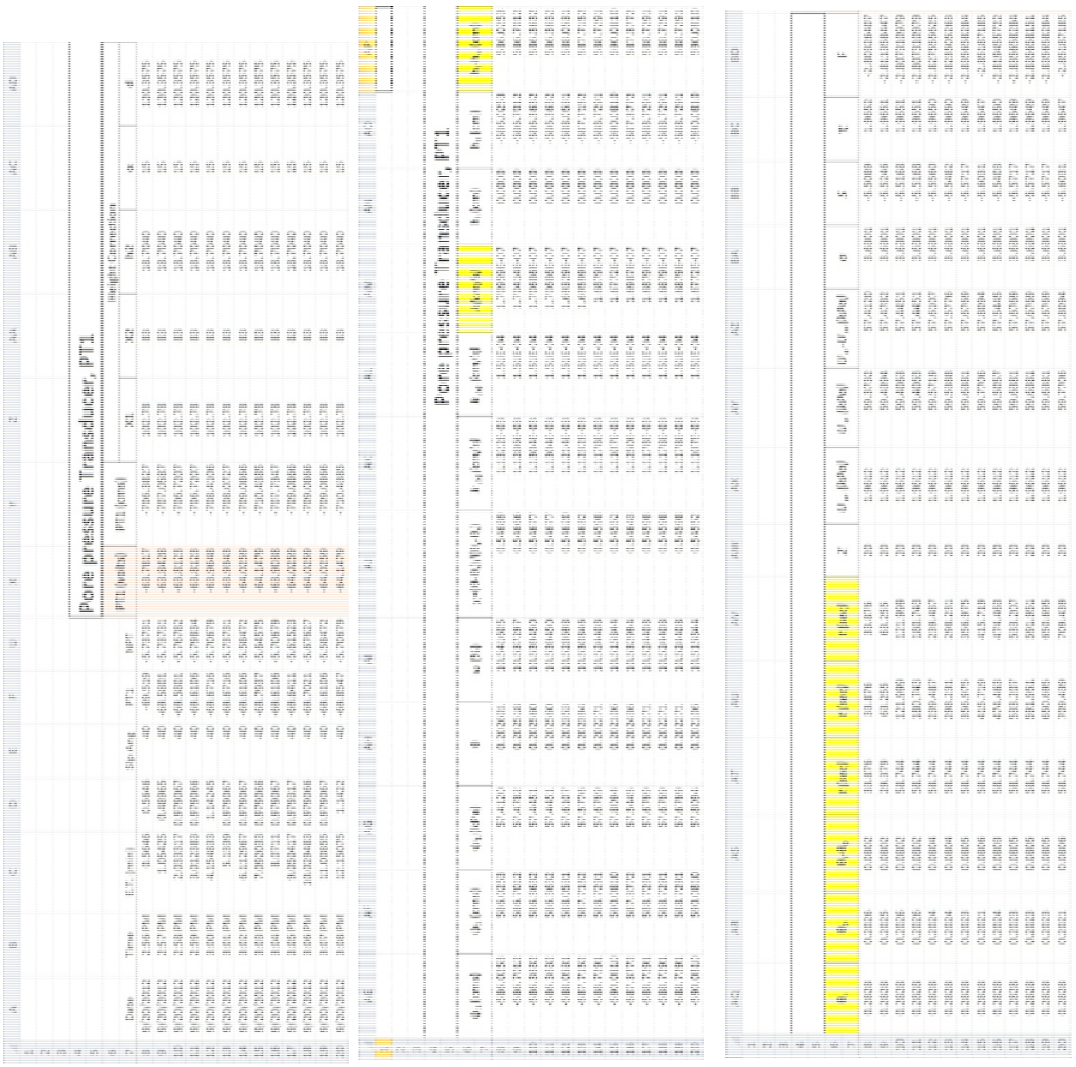

Figure D-1 Sample table of calculations of factor of safety.